APPLICATIONS OF NOVEL NANOMATERIALS TO IMPROVE FOOD SAFETY

A Doctoral Dissertation
Presented to
The Faculty of the Graduate School
At the University of Missouri

In Partial Fulfillment
Of the Requirements for the Degree
Doctor of Philosophy

by
ZHONG ZHANG
Dr. Mengshi Lin, Dissertation Supervisor

DECEMBER 2014

The undersigned, appointed by the dean of the Graduate School, have examined the dissertation entitled

APPLICATIONS OF NOVEL NANOMATERIALS TO IMPROVE
FOOD SAFETY

Presented by Zhong Zhang

a candidate for the degree of Doctor of Philosophy,

and hereby certify that, in their opinion, it is worthy of acceptance.

_____

Dr. Mengshi Lin, Food Science

_____

Dr. Azlin Mustapha, Food Science

_____

Dr. Bongkosh Vardhanabhuti, Food Science

_____

Dr. Qingsong Yu, Mechanical and Aerospace Engineering

ACKNOWLEDGEMENTS

Table of Contents

LIST OF FIGURES

LIST OF TABLES

Table **Page**

APPLICATIONS OF NOVEL NANOMATERIALS TO IMPROVE FOOD SAFETY

Zhong Zhang

Dr. Mengshi Lin, Dissertation Supervisor

ABSTRACT

Food safety is receiving much attention due to the increasing occurrence of food safety incidents in recent years. The emerging nanoscience and nanotechnology may provide novel solutions for the prevention of food safety incidents. This dissertation aims to apply novel nanomaterials and new techniques, such as dynamic light scattering and surface enhanced Raman spectroscopy (SERS) to build rapid analytical methods to improve food safety. Objectives of this study are to: (i) investigate a systematic approach to characterize, detect, and quantify the contamination of engineered nanoparticles in foods; (ii) incorporate gold nanoparticles into dynamic light scattering technique and use them for rapid analysis of aflatoxin in milk. The sensitive method can be easily adapted to determine other food contaminants if corresponding antibodies are used; (iii) develop two simple and reproducible methods to fabricate standing gold nanorod arrays. The standing arrays on gold-coated silicon can generate strong and reproducible signals for SERS. They were successfully applied in the detection of pesticides in apple juice and vegetables. Results of this study demonstrate that there is a great potential to use novel nanomaterials to help solve food safety issues.

CHAPTER 1

INTRODUCTION

1.1 Background

There has been a growing concern about food safety due to the increasing number of food safety incidents in recent years. For example, in 2006, Greenpeace tested some vegetables sold in two grocery stores in Hong Kong and discovered that 70% of tested samples contained pesticide residues (Zhang and Carmody 2009). Thirty percent of tested vegetable samples exceeded the safety levels and several samples were tested positive for illegal pesticides. In food safety scandals occurred in 2008 in China, melamine was deliberately added into raw milk to artificially boost the protein content. Melamine is a synthetic chemical that can lead to kidney stone and renal failure among infants and young children. The melamine adulterated infant formula affected around 300,000 Chinese infants and children, with six reported deaths (Gossner and others 2009). Melamine was also found in a variety of dairy products, such as frozen dessert, yogurt, protein powders, and candies. During this food safety incident, the melamine contaminated products were found in 47 countries (López and Quereda 2011).

In 2011, poor-quality alcohol, contaminated by ammonium nitrate and methanol, has resulted in an estimated 126 deaths in West Bengal, India. In the same year, meat and egg products were contaminated by the animal feed containing dioxins, which affected 4700 German farms (Wall 2014). In 2013, several European countries, including Romania, Serbia, and Croatia, reported

nation-wide contamination of milk for human consumption with aflatoxins (Tran 2014). The consumption of aflatoxin contaminated milk posed great health risks to consumers due to the strong carcinogenic effect of aflatoxins.

To improve food safety and reduce occurrence of food safety incidents, it is of critical importance to develop reliable, fast, and simple analytical methods to detect food contaminants. The fast and simple detection methods can help detect and identify food contaminants in a shorter amount of time, enable faster responses and actions to the contaminated food products, and prevent unsafe foods flowing into the market.

Traditional analytical methods for chemical contaminants include high performance liquid chromatography (HPLC), gas chromatography (GC), mass spectroscopy (MS), and others. HPLC and GC are reproducible and accurate methods for the analysis of various food contaminations, such as aflatoxin M1 in cow's milk, pesticides in fruits, and chemical contaminants in water (Kim and others 2000; de KOk and Hiemstra 1992; Watabe and others 2004). HPLC and GC have been recommended by the FDA and AOAC as standard detection methods for many food contaminants (Turnipseed and others 2008; Lehotay and others 2005). However, these methods have some limitations, such as high cost, complex sample pretreatments, and low analyzing capacity (Zheng and He 2014).

Because of the fast development of nanotechnology and nanomaterials, a new door was opened for analytical science. The specific size and unique optical property of nanomaterials make them very useful in amplifying the signals acquired by dynamic light scattering (DLS) and surface enhanced Raman spectroscopy (SERS). By choosing appropriate nanomaterials and using specific strategy to modify the nanomaterial, it is possible to use novel nanomaterial to

develop fast, simple, and cost-effective methods to measure food contaminants and improve food safety.

However, the applications of engineered nanomaterials will inevitably lead to contamination of nanomaterial in our environment and food supply chain (Martirosyan and Schneider 2014). The toxicity of the engineered nanomaterials is still not clearly understood and needs further investigation (Reidy and others 2013). It is very important and urgent to develop accurate and reliable detection methods for novel nanomaterials as food contaminants. The current challenge is that the contamination of engineered nanomaterials in foods is hard to detect compared to other chemical contaminants and biological contaminants due to their unique properties. Therefore, a combination of technologies needs to be developed to solve this problem.

1.2 Objectives

The objectives of this study were to: (i) characterize and quantify engineered nanoparticles (NPs) in food matrix; (ii) use Au NPs and DLS in the analysis of food contaminants; and (iii) detect of food contaminants by SERS using Au nanorods (NRs). Specific objectives were:

(i) Characterize and quantify engineered NPs in food matrix

- To detect and characterize pure Ag NPs using UV-vis spectrophotometer, Zeta-sizer, SEM and TEM;
- To detect and quantify Ag NPs in pear samples using SEM-EDS, ICP-OES;
- Investigate the potential penetration of Ag NPs on pear samples by ICP-OES and TEM.

(ii) Use Au NPs and DLS in the analysis of food contaminants

- To develop rapid detection methods for aflatoxin M1 using immuno-magnetic beads and Au nanoprobes coupled with dynamic light scattering in real food matrix.

(iii) Detect of food contaminants by SERS using Au NRs

- Develop a simple, cost-effective, high-yield, and reproducible methods to fabricate vertically aligned Au NR arrays on silicon;

- Choose appropriate Au NRs to fabricate standing arrays on gold-coated silicon slides; develop a simple method to remove surfactant on the surface of Au NRs arrays without destroying their morphology.

- Use standing Au NR arrays as reproducible SERS substrates to detect pesticides in apple juice and vegetables.

CHAPTER 2

LITERATURE REVIEW

2.1 Gold and Silver Nanomaterials

Nanomaterials are usually defined as any material with size between 1-100 nm in at least one of the three dimensions (Kreyling and others 2010). Due to their small size, nanomaterials show different physical, chemical, and biological properties compared to their corresponding bulk materials (Daniel and Astruc 2004). There are a variety of nanomaterials, such as metal nanomaterials, carbon nanomaterials, silicon nanomaterials, polymer nanomaterials, and organic nanomaterials (Rao and others 2006). Nanomaterials can have various shapes, such as sphere, cube, triangle, rod, tube, and wire. Among those nanomaterials, metal nanomaterials, especially gold and silver nanoparticles, have been widely studied in recent years (Huang and others 2006; Luo and others 2006).

Gold and silver NPs are used in many areas due to the easy preparation step, versatility in surface modifications, and tunable optical properties (Lee and El-Sayed 2006; Sun and Xia 2003). Gold and silver NPs are usually synthesized by reducing $AuCl_4^-$ and Ag^+ using sodium citrate solution at boiling temperature for 10 - 20 min (Kimling and others 2006). The size of Au NPs could be easily controlled by adjusting the ratio of $AuCl_4^-$ and citrate. The citrate reduction method could reproducibly produce Au NPs with size from 10 to 40 nm. The Ag NPs synthesized by the citrate reduction method are usually in the range of 20 - 80 nm (Pillai and Kamat 2004). The citrate ions form a monolayer on the surface

of Au and Ag NPs and perform as a protection layer for the Au and Ag NPs because the negative charges of citrate ions prevent the aggregation of NPs. Therefore, Au and Ag NPs can be homogeneously dispersed in the citrate solution and used for various applications (Figure 1).
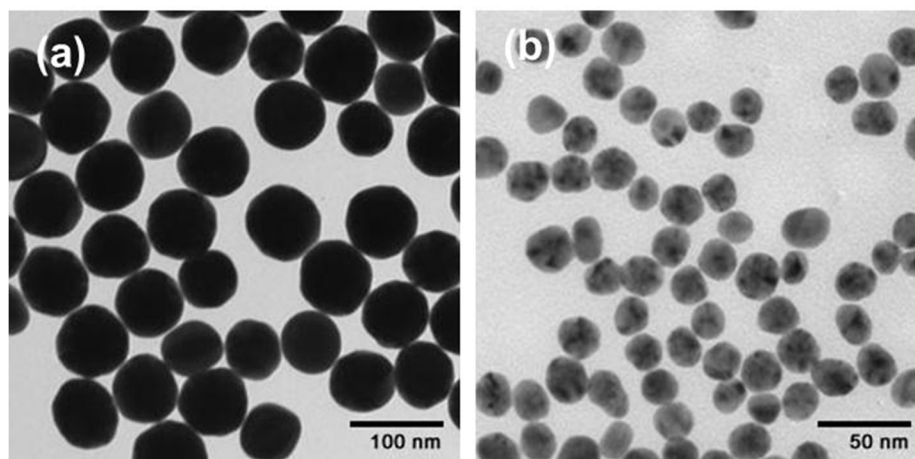
Figure 1 TEM image of (a) gold and (b) silver NPs (nanoComposix).

It is easy to modify the surface of Au NPs because of the presence of a single layer of citrate ions, which facilitates the attachment of biomolecules, such as DNA, antibody, and enzymes on the nanoparticle surface with or without the help of thiol linker (Drummond and others 2003; El-Sayed and others 2005). For example, single-stranded DNA has been loaded on the surface of Au NPs using the thiolated end of DNA. Gold NPs have also been linked to antibody using thiolated polyethylene glycol (Qian and others 2008). The successful modification of Au NPs with those biomolecules makes it possible to use Au NPs for various delivery and detection purpose. In addition, the localized surface plasmon resonance (LSPR) on Au or Ag NPs can be tuned by changing their size and shape (Liu and others 2011). The LSPR response of Au and Ag NPs could be used to design many different types of biosensors. For example, Au NPs have been used to detect and kill pathogens using the LSPR response (Ray and others 2012). The unique

properties of Au and Ag NPs make them very useful in different areas. In this dissertation, the main objective was to apply novel gold and silver nanomaterials to improve food safety.

2.2 Contamination of Nanomaterials in Foods

Studies have demonstrated that due to their small size, Ag NPs can penetrate bacterial cell membrane and cause strong inhibitory effect to their growth (Panáček and others 2006). Ag NPs have been incorporated into food packaging materials to extend the shelf-life of foods because of the strong antimicrobial property of Ag NPs (Azeredo 2009). For example, it has been shown that the antibacterial properties of hydroxypropyl methylcellulose/Ag NPs thin films have strong inhibitory effect against *Escherichia coli* and *Staphylococcus aureus* (De Moura and others 2012). The nanocomposite films containing 41 nm Ag NPs showed a great bactericidal effect in the disk diffusion studies. It has also been demonstrated that the chitosan-based nanocomposites containing Ag NPs were effective against *E. coli*, *S. aureus*, and *L. monocytogenes* (Llorens and others 2012). In addition, it has been reported that silver-containing polyethylene layer showed high bactericidal capacity against *Alicyclobacillus acidoterrestris*, and the material prolonged the shelf-life of apple juice (Fernández and others 2009). However, Ag NPs or ions can be unintentionally released from the food packaging materials and migrate to foods, thus posing health risks to consumers.

In addition, new formulations of chemicals containing silver nanomaterials could appear in the food products (Benn and others 2010). For example, Ag NPs could be released from different materials including textiles and

paints. Silver NPs were also found to be used in disinfecting sprays, deodorants and other cosmetics as antimicrobial agents (Reidy and others 2013). Due to the carcinogenic properties of organic pesticides, new types of pesticides containing inorganic nanomaterials have been developed and used to control the pests in agriculture produce (Bergeson 2010). Due to the potential applications of inorganic nanomaterial in the food and agriculture products, the knowledge of the residue and translocation of nanomaterials became extremely important to the food industry. Therefore, it is of paramount importance to establish novel methods for the detection and quantification of nanomaterials in the food matrix.

2.3 Nanomaterial and Dynamic Light Scattering

Dynamic light scattering (DLS), also called photon correlation spectroscopy and quasi-elastic light scattering, is a technique which can be used to determine the size distribution of small particles in the solution (Goldburg 1999). As shown in Figure 2, a monochromatic beam of laser light is directed to small particles in the solution. The laser lights are scattered and acquired by a detector at a specific angle with respect to the transmitted light. Meanwhile, small particles are perpetually moving and rotating in the solution because of the Brownian motion. Due to the motion of these particles, their positions are constantly changing, resulting in the fluctuation of total scattered light. According to the Brownian motion, bigger particles move slower than smaller particles. Particles with different sizes have different fluctuation patterns. Therefore, the particle size can be calculated through analyzing the fluctuation patterns using the Stokes-Einstein equation (Pecora 1985).

If different samples have the same size of particles, then the sample containing more particles can reflect more scattering light due to the larger scattering surface. In other words, the total DLS intensity is positively related to the number of particles in the sample solution (Xie and others 2007; Liu and others 2007). Therefore, the concentration of particle could be determined by measuring the DLS intensity.
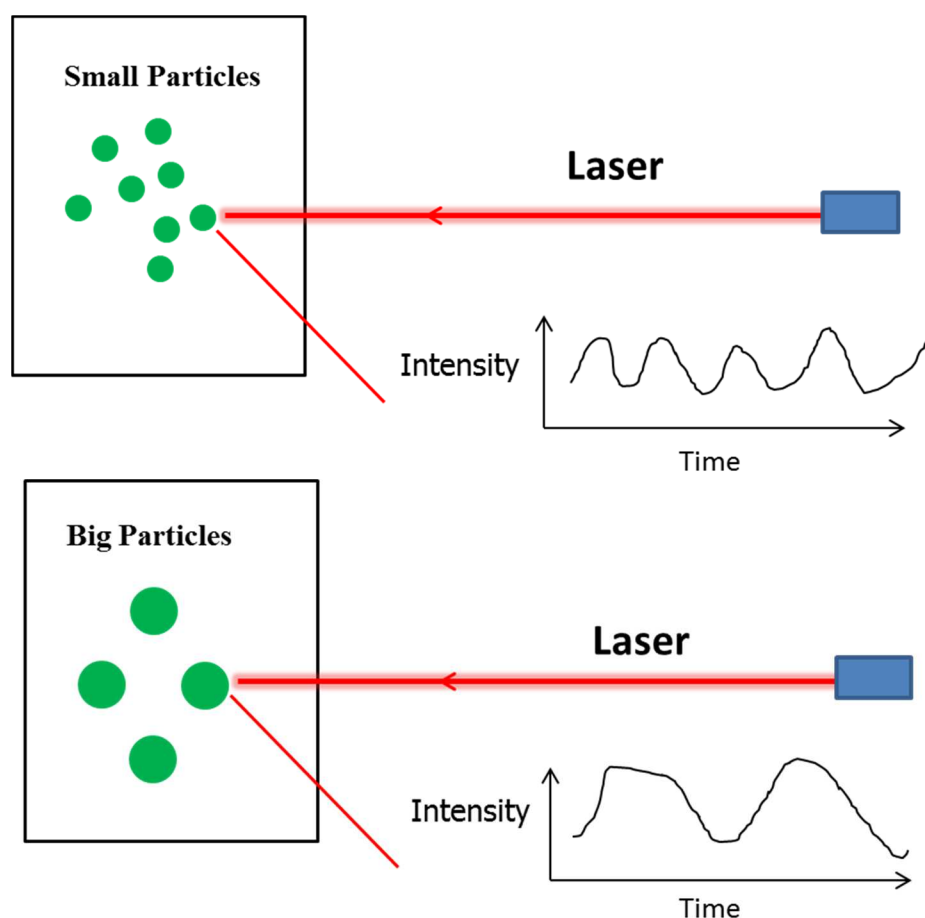
Figure 2 Scheme of dynamic light scattering technique.

If there are a same number of particles in two different solutions, the solution with bigger particles will scatter more light than the solution with smaller particles. The DLS intensity is positively related to the third power of the particle radius. For example, the DLS intensity of a 100-nm Au NP is 1000 times

of the intensity of a 10-nm Au NP (Instruments 2004). Therefore, bigger NPs could be used to amplify the DLS intensity. The size of most biomolecules, such as proteins, is in the range of 1-5 nm. If a particle with size of 35 nm was used to amplify the signal of a protein with size of 1.0 nm, the DLS intensity of protein would be amplified by 42,875 times. Therefore, the DLS could be used to detect very low concentration of proteins in the sample solution if a proper scheme is used. However, a critical problem is which type of particle is the best selection for the signal amplification.

Fortunately, Au NPs with size of 10 - 40 nm can be easily synthesized by the citrate reduction method and maintain a good stability in the citrate solution. More importantly, Au NPs can be easily modified by antibody or other proteins through the hydrophobic interaction and Au-S bonding. For example, Au NPs were directly modified by antibody and used in lateral flow immunodipstick for the detection of aflatoxin (Liao and Li 2010). After the surface modification by antibodies or antigens, Au NPs are given the corresponding functionality and can be used in the antibody-antigen reaction. Due to the bigger size of Au NPs, Au NPs can generate high scattering and be easily detected by DLS (Jans and others 2009). The specificity of antibody-antigen reaction would make DLS very selective and sensitive in the detection of food contaminants when coupled with modified Au NPs.

2.4 Nanomaterial and Surface enhanced Raman spectroscopy

2.4.1 Raman spectroscopy

The photons, which make up the light, may interact with the molecule when the incident light is directed on the molecule. The photons could be adsorbed by the molecule if the photon energy matches the energy gap between ground state and excited state of the molecule. The molecule is promoted to a higher energy excited state after the adsorption of photon energy (Smith and Dent 2005).

On the other hand, if the photon energy does not match the differences between two energy levels of a molecule, the photon can also interact with the molecule and scattered from it (Colthup and others 1990). For example, when a single frequency of light is used to irradiate samples, the photons interact with the molecules and polarize the electron clouds near the nuclei to form a virtual state for this molecule. The lifetime of this virtual state is very short, leading to the re-radiation of the photons. When the energy of re-radiated photon is equal to the energy of incident photon, the scattering is called "Rayleigh scattering", which is the dominant scattering and does not involve any energy transfer. When the molecule in the ground state is promoted to virtual state and then returns to excited state, the scattering is called "stokes scattering". This process involves the energy transfer from photons to the molecule. Likewise, when the molecule in excited state is promoted to virtual state and then returns to the ground state, the scattering is called "anti-stokes scattering". This scattering process transfers the energy from the molecule to photons. Raman scattering is the inelastic scattering of a photon, including both Stokes and anti-Stokes scattering. However, Raman

spectroscopy usually records the Stokes scattering because the anti-Stokes scattering is very weak compared to the Stokes scattering.

By recording the Raman scattering and calculating the energy loss of incident photons, Raman spectroscopy provides the detailed vibrational information for the molecules in the sample (Ferraro 2003). The Raman spectra are like "fingerprints" to the molecules, which would be very useful for the identification of the molecules. However, as stated above, the dominant scattering of the photon-molecule interaction is Rayleigh scattering. Raman scattering is a very weak effect.

2.4.2 Mechanism of surface enhanced Raman spectroscopy

SERS is a technique that can greatly enhance Raman scattering by placing the target molecules on the surface of roughened metal or the junctions of metal NPs, such as Ag and Au NPs (Smith and Dent 2005). SERS phenomenon was first observed in 1974 by a group of scientists at the University of Southampton (Fleischmann and others 1974). They reported strong Raman scattering from pyridine adsorbed on a roughened silver electrode. The enhancement was calculated to be around 10^6. It is believed that there are two possible reasons for the enhanced Raman scattering. Herein, we use Ag NPs as a model nanostructure to illustrate the SERS mechanism.

(1) Electromagnetic mechanism (Etchegoin and Le Ru 2011): The surface of Ag NPs is covered with negatively charged electrons. Those electrons can move to an extendable distance from the silver surface. When a light beam is incident on Ag NPs, the freely moving electrons can interact with the light. They start to oscillate as a collective group across the surface of Ag NPs. The collective

oscillation of the electrons is called localized surface plasmon. The electromagnetic field (E_r) at the surface of Ag NPs could be calculated using the following equation:

$$E_r = E_0 \cos\theta + g\left(\frac{a^3}{r^3}\right)E_0 \cos\theta \qquad (1\text{-}1)$$

In this equation, E_r is the electromagnetic field at a distance r from the NP surface, a is the radius of the NP, θ is the angle relative to the direction of the electromagnetic field, and g is a constant related to the metal. As is shown, the electromagnetic field decreases rapidly as the distance (r) increases (Figure 3). When a molecule is close to the surface of Ag NPs, the molecule will experience strong electromagnetic field. In another word, the molecule is located in a high density cloud of freely moving electrons and interacts with those electrons, resulting in great polarization of the molecule and strong Raman scattering. Therefore, the Raman scattering is greatly enhanced in this situation. It was calculated that the Raman enhancement are proportional to $(E_r)^4$. In this mechanism, the molecule has to be close enough to experience the electromagnetic field and interact with the electrons. The maximum electromagnetic field will be obtained if the frequency of incident light beam (laser) matches the resonance frequency of Ag NPs. In this circumstance, the molecule will experience the maximum Raman enhancement. The electromagnetic enhancement is generally applied to all the molecules close to the nanoparticle surface.

(2) Charge transfer mechanism: this mechanism explains the Raman enhancement of molecules that are bound to the surface of Ag NPs. For example, a molecule with a free thiol group could easily bind to the silver surface through

the Ag-S bond. Therefore, the electrons could be transferred from the silver surface to the molecule. Due to the interaction with the electrons, the molecule will be polarized significantly. It is believed that the Fermi level of metal locates between the ground state and one of the excited states of the adsorbed molecule (Lombardi and others 1986). There are transitions between the molecule ground sate and the Fermi level or from the Fermi level to excited states. Due to the presence of the transitions, the charge transfer excitations can occur at about half energy of the intrinsic intra-molecule excitations of the adsorbed molecule, resulting in enhanced Raman scattering. This type of molecules could also experience strong electromagnetic enhancement due to the close distance to the nanoparticle surface. Therefore, the combination of electromagnetic enhancement and charge transfer enhancement usually give this molecule larger Raman enhancement than other molecules.
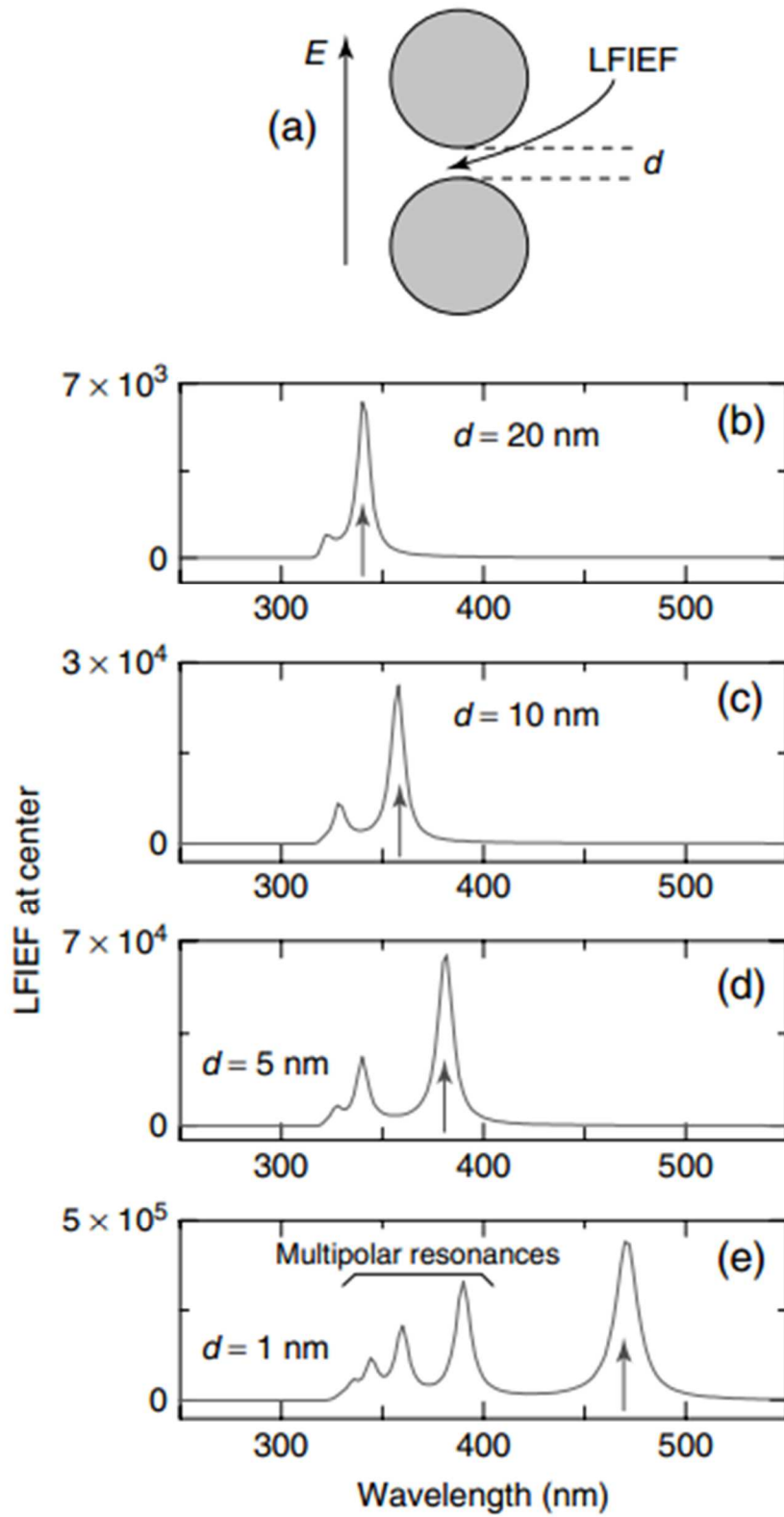
Figure 3 Local field intensity enhancement factor at the center of a dimer with different gap distance: (a) dimer of Ag NPs, (b) 20 nm, (c) 10 nm, (d) 5 nm, and (e) 1 nm (Prodan and others 2003).

2.4.3 Detection of Food Contaminants by SERS

SERS has been applied in chemical analysis, detection of food contaminants, biological sensing, and environmental monitoring (Fleischmann and others 1974; Cooney and others 1977; Liu and others 2012a; Qian and others 2008; Ren and others 2012). Nowadays, pesticide residues in agricultural products are posing great risks to the public health (Dunlap and Beus 1992). The monitoring of pesticide residues on agricultural products is becoming increasingly important. However, conventional methods to detect the pesticides are time-consuming, complex, and are difficult for on-site detection. In addition, it is difficult to use conventional methods to detect multiple pesticides simultaneously. The SERS technique enables rapid detection of pesticides and can potentially differentiate multiple pesticides at the same time. SERS has been applied in measuring three types of pesticides, carbaryl, phosmet, and azinphos-methy using the Q-SERS as the substrates (Liu and others 2012b). By building principal component analysis (PCA) models, the SERS spectra of three pesticides were easily differentiated.

SERS has also been used to detect melamine in dairy products (Liu and others 2010). Melamine, a chemical for industrial uses, was intentionally added in foods to artificially boost the protein index of products. HPLC is a traditional method commonly used to measure melamine. But HPLC and other chromatography-based methods need time-consuming steps such as extraction, purification, and separation by HPLC column. In contrast, the SERS technique can effectively solve these problems and has been used to analyze melamine in dairy products. SERS methods have several advantages compared to the traditional

analytical methods such as HPLC and GC. First, SERS does not require complex sample pretreatments and highly skilled staff for operation. Second, SERS is a fast method and only needs a few minutes for a single measurement, which is much faster than HPLC and GC. However, a main problem of SERS is the lack of reproducible, efficient, and low-cost substrates. Therefore, it is of paramount importance to develop sensitive and cost-effective substrates for SERS.

A variety of substrates have been developed in recent years for SERS applications. The substrates fabricated by nanolithography show promising SERS enhancement and great reproducibility (Alvarez-Puebla and others 2007; Abu Hatab and others 2008; Theiss and others 2010). Sub-10-nm metallic nanogap arrays with precise control of the gap morphology have been produced by nanolithography technique (Im and others 2010). However, it is still a big challenge to fabricate smaller nanogaps (1-2 nm) by nanolithography. The nanolithography also requires specific equipment for the development of nano-patterns and the deposition of gold or silver layer. Another lithographic method, called nanosphere lithography, has been adopted by many scientists because it is inexpensive and able to create large area of ordered nanostructures (Chan and others 2007; Im and others 2013; Zhang and others 2006). However, the nanosphere lithography still needs to pattern the substrate surface by a layer of nanospheres in advance, which is difficult to be tailored for different SERS detection strategies. In addition, SERS substrates can also be fabricated by assembling Au or Ag NPs on glass, silicon surface, or liquid/liquid interface (Su and others 2011; Cecchini and others 2012; Alvarez-Puebla and others 2011; Peng and others 2013; Tong and others 2011; Chen and others 2011).

Among all these fabrication methods, the self-assembling approach is the most convenient and cost-effective method because it can be performed without using expensive equipment. Between the junctions of the self-assembled NPs, numerous hot-spots for SERS can be created where intense electromagnetic field is generated at this area.

2.4.4 Standing Au Nanorod Arrays as SERS Substrates

Gold nanorod (NR), an anisotropic nanostructure, has gained much attention due to its unique ability to interact with light of varying wavelengths (Murphy and others 2005; Grzelczak and others 2010; Rycenga and others 2011). Gold NR displays two separate surface plasmon resonance (SPR) bands known as transverse and longitudinal plasmon bands. The longitudinal plasmon band can be tuned from visible region to near infrared (NIR) region by carefully controlling the aspect ratio and the size of Au NR (Murphy and others 2011; Sivapalan and others 2013). Due to the strong interaction of NR with the light in this region, Au NRs have been employed in biomedical detection using dark-field imaging, two-photon luminescence, optoacoustic imaging, and confocal reflectance microcopy (Sokolov and others 2003; Wang and others 2005; Durr and others 2007; Franchini and others 2010). Gold NRs have also been applied in the detection of food pathogens and environmental toxins by functionalizing the Au NRs with specific antibodies and monitoring the change of longitudinal surface plasmon band (LSPR) (Singh and others 2009; Wang and Irudayaraj 2010; Wang and Irudayaraj 2008; Wang and others 2010). In addition, Au NRs could also be applied in cancer therapy using the heat generated by the NRs

during the laser irradiation (Huang and others 2006; von Maltzahn and others 2009; Hu and others 2006; Tong and others 2009; Huang and others 2008).
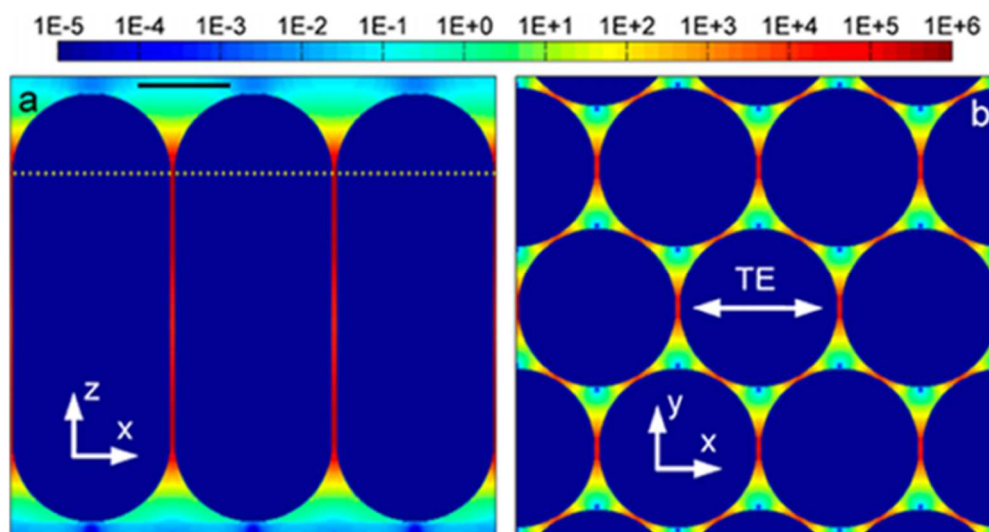
Figure 4 Electromagnetic field of standing Au NR arrays: (a) side view; (b) top view. (Peng and others 2013).

Rapid developments of SERS make it a powerful tool in analytical chemistry, but the lack of highly uniform and robust nano-substrate, to some extent, limits the application of SERS as a quantification tool. In order to solve this problem, standing Au NR arrays have been selected to improve the surface enhancement and the reproducibility of SERS. Standing Au NR arrays, as a new nanostructure, can generate strong and reproducible electromagnetic field (Figure 4). Compared to randomly distributed Au NRs, standing Au NR arrays can provide high enhancement and narrowly distributed enhancement factors for SERS. However, current methods of fabricating standing Au NR arrays have several disadvantages, such as low-yield, high-cost, and low-reproducibility. This dissertation aims to develop a high-yield, simple, and economic process to fabricate standing Au NR arrays using self-assembling approach. The standing Au

NR arrays were then used as high-performance and reproducible SERS substrates for the analysis of contaminants in foods.

CHAPTER 3

Detection of Engineered Nanoparticle Contamination in Foods

3.1 Introduction

It is estimated that global crop yields are reduced by 20 to 40% per year due to pest infection and plant diseases (FAO. 2012; Strange and Scott 2005). The use of pesticides could effectively control this problem and improve the quality of crops (Carvalho 2006). In recent years, inorganic pesticides, such as nanosized silver, silica, and copper, have captured the attention of agrichemical companies. In particular, Ag NPs, known for their antimicrobial and insecticidal properties, have been used as pesticides in agriculture or intentionally incorporated in food packaging materials (Bergeson 2010; Duncan 2011; Martirosyan and Schneider 2014; Mura and others 2013). By doing so, the manufacturers expect that new products can help farmers spray the fields more efficiently and release less pesticide to environmental drift and storm water runoff. However, the toxicity of nanoscale pesticides to humans and the environment has not been fully investigated and understood (Bouwmeester and others 2009; Magnuson and others 2011). There is little information about the fate of these nanosilver pesticides in the environment or in agriculture products. Therefore, there is a growing concern about the safety of nanosilver pesticides used in food crops and produce.

To understand the fate and measure the residue of nanosilver in food crops, it is critical to have a suitable and accurate analytical method for detection and characterization of Ag NPs. However, little information could be found on

detection and characterization of Ag NPs in agricultural products. Because no single technique is able to provide all the information that is necessary to identify and quantify Ag NPs in food crops, we aimed to develop a combination of methods that are sensitive enough for the measurement of low concentrations of Ag NPs and that can directly observe the size, shape, and translocation of Ag NPs in fruit samples.

Conventional techniques such as optical microscope are unsuitable for measuring extremely small size of NPs. Several studies have been reported on the detection of NPs using field flow fractionation (FFF), hydrodynamic chromatography (HDC), and dynamic light scattering (DLS) (Kammer and others 2011; Tiede and others 2010; Murdock and others 2008). Although FFF, HDC, and DLS are good methods to detect the size distribution of NPs, they require suspending NPs in solution prior to testing, and it is difficult to apply these methods in detection of NPs in foods due to the difficulty in extracting the NPs from food matrices, especially when the concentration of NPs is at a very low level. In addition, these methods cannot be used to measure important physical properties (shape, etc.) of NPs and the interaction between NPs and plant tissues. In this study, TEM and SEM were selected to detect the Ag NPs in fruits because they have been widely used to characterize the size, shape, and structure of nanomaterials and can directly detect and visualize the penetration and interaction of NPs with plant tissues (Tiede and others 2008; Feng and others 2006; Zhao and others 2011; Chen and others 2009). In addition, inductively coupled plasma optical emission spectrometry (ICP-OES) has been employed to determine the metal content in the soil and plant samples with high accuracy (Tighe and others 2004). Different metal elements could be rapidly detected by

22

ICP-OES at one time (De la Rosa and others 2003; Ikem and others 2002). ICP-OES were thus selected in this study to determine the concentration of Ag NPs in fruit samples.

The objective of this study was to detect, characterize, and quantify Ag NPs in fruit samples (i.e., pears) by a combination of techniques including TEM, SEM, EDS, Zetasizer, and ICP-OES. The residue and penetration of Ag NPs on the pear skin were studied by TEM, SEM, and ICP-OES.

3.2 Materials & Methods

3.2.1 Pear samples and Ag NPs

Pears were purchased from a local grocery store. Ag NPs were purchased from NanoComposix (San Diego, CA, USA) with a silver concentration of 0.02 mg/mL in citrate solution and an average diameter of 20 and 70 nm, respectively. Ag NPs with different diameters were used in this study due to the fact that most nanoscale silver was present as mixed nanoparticles in the pesticide solutions. The size distribution of NPs was measured by a Zeta-sizer (Malvern Nano S, Worcestershire, U.K.). TEM (JEOL 1400, Tokyo, Japan) and SEM equipped with EDS (Quanta FEG 600 ESEM) were used to characterize the Ag NPs in the pear tissues. The size of Ag NPs was calculated using ImageJ 1.45 (available at http://rsb.info.nih.gov/ij/).

3.2.2 TEM characterization of Ag NPs in pear

A pear skin (4.7 mm^2) and a pulp cube (2 mm × 2 mm × 1 mm) were cut from the pear and immersed in the Ag NP (20 nm) solution for 5 days. The

specimens were then washed with distilled water and suspended in a primary fixative solution (2% glutaraldehyde, 2% paraformaldehyde in 0.1 M cacodylate) for 2 h on a rocker at room temperature. The specimens were washed three times with buffer and placed into a secondary fixative solution (2% osmium tetroxide in 0.1 M cacodylate) for 2 h. After the secondary fixation, the specimens were washed three times with distilled water. Dehydration of samples was performed in graded acetone series by the following sequence: 25%, 50%, 70%, and 95% (each for 30 min) and 100% (three times of 30, 30, and 60 min). The infiltration was started using 1 part resin and 2 parts acetone for 2 h, continued with 1 part resin and 1 part acetone for 2 h, 2 parts resin and 1 part acetone for 2 h, and, finally, pure resin for 8 h. The resin was then placed in embedding capsules and polymerized at 60°C for 2 days. The ultrathin sections were cut and placed on the grid for staining. The grid was stained by uranyl acetate followed by washing with distilled water and lead citrate staining. Finally, the grid was washed by distilled water and observed by TEM (120 Kv).

3.2.3 SEM characterization and EDS analysis of Ag NPs in pears

Pear skin and pulp were treated as described in the TEM section. The samples were transferred into the primary fixative solution and then subjected to dehydration, followed by the critical point drying using liquid carbon dioxide. The samples were first flushed by liquid carbon dioxide for 20 min in a critical point dyer (AutoSamdri 815, Tousimis, USA). Liquid carbon dioxide is heated above 31°C and stabilized for 4 min. Then the pressure was gradually released for the drying of pear samples. The skin and pulp samples were then coated with

a 150 nm carbon layer for SEM characterization. The elemental composition of embedded NPs in pear tissues was determined by the EDS.

3.2.4 Quantification of Ag NPs in pear samples

Pear cubes including the pear skin (50 g) were cut from intact pears. Ag NP solutions with a series of volumes (0 to 1000 μL) were applied on the surface of pear cubes. The pear cubes were then blow-dried at room temperature and stored at 4°C for 7 days. After storage, the pear cubes were dried at 105°C for 3 days to completely remove the moisture of the pears. Dried samples were transferred to crucibles and burned at 500°C for 5 h. After cooling, 10 mL HCl (6 M) were added in the crucibles to dissolve the ashes. The mixtures were thoroughly transferred to a Kimax glass tubes and finally diluted to 50 mL with distilled water. The solution was filtered through Whatman #42 filter papers and subjected to the ICP-OES analysis. The concentration of Ag NPs was expressed as the concentration of Ag element in the pear samples. The recovery rate of Ag NPs was calculated according to the following equation:

$$\text{Recovery} = (C_{\text{sample}} - C_{\text{control}})/C_{\text{spiked}} \times 100\% \qquad (2\text{-}1)$$

where C_{sample} is the Ag concentration in the spiked pear samples, C_{control} is the Ag concentration in the control pear samples, and the C_{spiked} is the spiked concentration of Ag calculated according to the spiked amount of Ag NPs solution and the weight of pear samples .

3.2.5 Penetration studies of Ag NPs on the pear skin

A circle (6.7 cm^2) was drawn by an ink pen on the skin of an intact pear. An aliquot (100 μL) of Ag NP solution was dropwise added on the circled skin by

a 10 μL pipette. The treated pears were blow-dried at room temperature, sealed in beakers and then stored in a 4°C refrigerator. Before sampling, the pear was completely rinsed with deionized water to remove the weakly attached Ag NPs. Both skin and pulp (4.60 ± 0.02 g) under the circled area were carefully peeled and collected from intact pears with time intervals of 0, 2, 4, 6, and 8 days. The concentration of Ag NPs in pear samples was determined by ICP-OES and expressed as the concentration of Ag element. The pretreatments and ICP-OES analysis were similar to the procedure described above.

3.2.6 Data analysis

Partial least squares (PLS) linear regression analysis and significance test ($P < 0.05$) were performed using the SPSS software (Version 16.0 for windows, IBM, New York, U.S.A.). The detection limit (DL) for Ag NPs was determined and expressed as the concentration of Ag element, which was calculated by the following equation according to the definition from the International Union of Pure and Applied Chemistry (IUPAC):

$$DL = 3\delta/m \qquad (2\text{-}2)$$

where δ is the standard error in the y-intercept, m is the slope obtained from a standard linear regression analysis, and the number 3 represents a 99.86% confidence interval.

3.3 Results & Discussions

3.3.1 Characterization of Ag NPs in citrate solution

The size, shape, and other physical properties of Ag NPs (20 and 70 nm) in 2 mM citrate solution were investigated by TEM (Figure 5). It is obvious that Ag NPs were uniformly dispersed in the citrate solution without any agglomerations. The shape of most 20 nm Ag NPs was spherical while the 70 nm Ag NPs were mostly oval in shape. The TEM image indicates an average particle size of ~21.3 and ~69.1 nm for these two types of Ag NPs, respectively, which is in close accordance with the product specifications (20 and 70 nm) provided by the manufacturer. However, TEM is not an ideal technique for routine analysis of size distribution of engineered nanoparticles because it is complicated and expensive. In this study, the size distribution of Ag NPs was also measured by the Zetasizer due to the simplicity and rapidness of this method. Figure 6 shows the size distribution of Ag NPs analyzed by the Zetasizer, which demonstrates that the average size for two types of Ag NPs is 25 and 73 nm, respectively. These results were also close to the labeled diameter provided by the manufacturer. However, the relative standard deviation of 20 nm Ag NPs (20%) is larger than that of 70 nm Ag NPs (4.2%). This is mainly because the hydrated layer was regarded as part of the Ag NPs. Therefore, the results acquired by the Zetasizer exhibit greater relative standard deviation. The advantage of using the Zetasizer is that the size distribution and average diameter of NPs could be directly read from the machine.
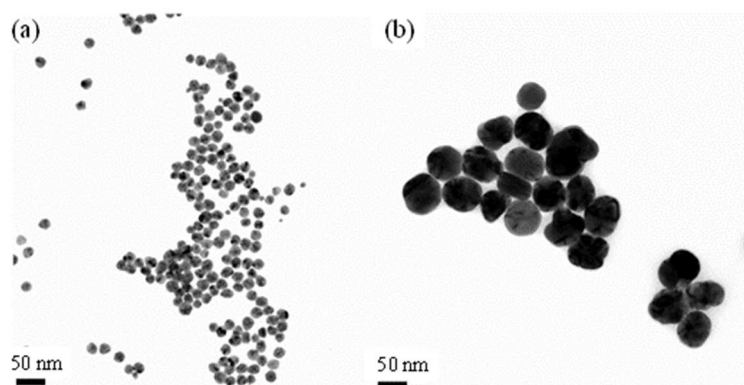
Figure 5 TEM images of Ag NPs in citrate solution (a) 20 nm, (b) 70 nm.
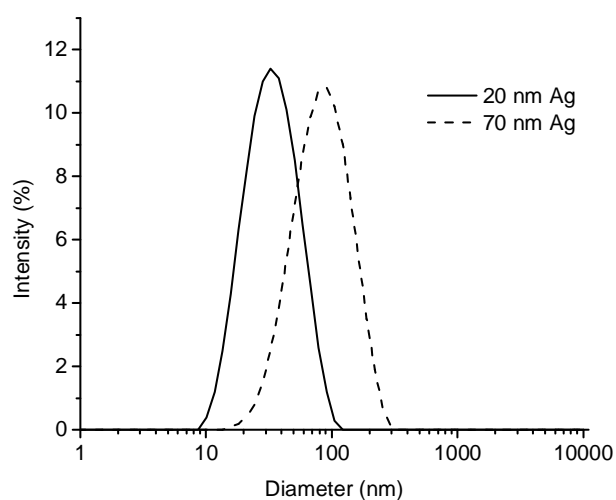
Figure 6 Size distributions of Ag NPs (20 nm and 70 nm) determined by Zetasizer.

3.3.2 Characterization of Ag NPs in pear tissues by TEM

Figure 7 shows TEM images in a vertical section of pear tissue samples treated by Ag NPs (20 nm). Ag NPs could be clearly observed in these TEM images. It was found that Ag NPs penetrated into the pear skin from the inner side or outer side of skin via the gaps of skin tissues. Ag NPs were firmly attached in tissues due to the high surface area of Ag NPs. During the penetration process from the surface to the central parts, Ag NPs might lose the protection from

surfactant citrate and tended to aggregate due to the interactions with the components in the pear skin. The aggregation status of Ag NPs was clearly observed in Figure 7b. Most Ag NPs were still round in shape but they aggregated with each other to form a cluster attaching on the pear tissues. Similarly, the penetration of Ag NPs inside the pear pulp was also observed by the TEM (Figure 7c). The size of Ag NPs was around 20 nm, which agrees with the value determined by Zetasizer. The TEM images also show that there was a thick layer coating on Ag NPs inside the pulp tissues (Figure 7d). This may be caused by the interaction of Ag NPs with macromolecular substances such as polysaccharides or pectin in the pear pulp. To detect the contamination of Ag NPs in fruits, it is of great importance to investigate the penetration of Ag NPs inside fruit tissues rather than the surface contamination because those penetrated Ag NPs could not be simply removed by washing with water. TEM could provide visual images for such contamination and penetration in fruit samples. The 20 nm Ag NPs are much smaller than 70 nm Ag NPs and, thus, are more difficult to be detected and visualized in TEM and SEM analysis. If 20 nm Ag NPs could be detected by SEM and TEM, then the same type but with much bigger size of NPs would be easily detected.
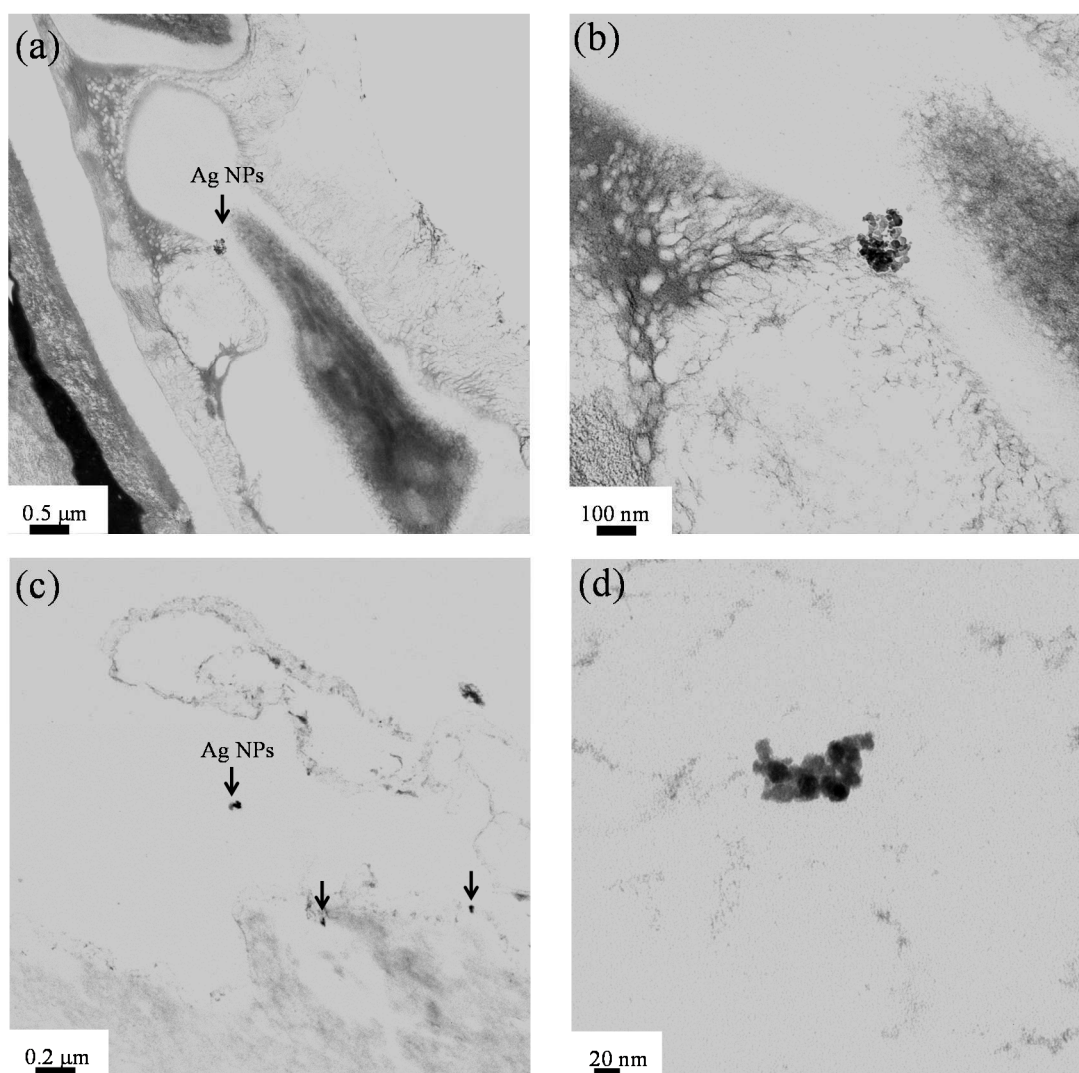
Figure 7 TEM characterizations of Ag NPs on pear tissues: (a) and (b) pear skin at different magnifications; (c) and (d) pear pulp at different magnifications.

3.3.3 Characterization of Ag NPs in pear tissues by SEM and EDS

Ag NPs on the surface of pear tissues could be clearly observed by SEM (Figure 8). Due to the high molecular weight of silver element, Ag NPs could be clearly differentiated from pear tissues because backscattered electrons made Ag NPs brighter than pear tissues. As shown in Figure 8a, some Ag NPs were coagulated and attached on the surface of pear skin, while other Ag NPs were embedded in the skin tissues. Figure 8b shows the Ag NPs in pear pulp. Some of them were entrapped inside the pulp tissues, thus part of the backscattered

electrons were blocked by the pulp tissues, which made them appear darker than other Ag NPs. In addition, the EDS were used to determine the elemental composition of those NPs. It was found that bright dots consisted of different amounts of Ag element ranging from 30% to 72%. The profile of EDS shows that a significant amount of Ag, S, P, and Na was present around the bright dot (Figure 8c). The P and Na are naturally existing elements in pear samples. Therefore, it was concluded that those NPs were Ag NPs. These results demonstrate that SEM coupled with EDS could be used not only to characterize the shape and aggregation status of NPs but also to determine detailed elemental composition of the NPs in fruit samples.
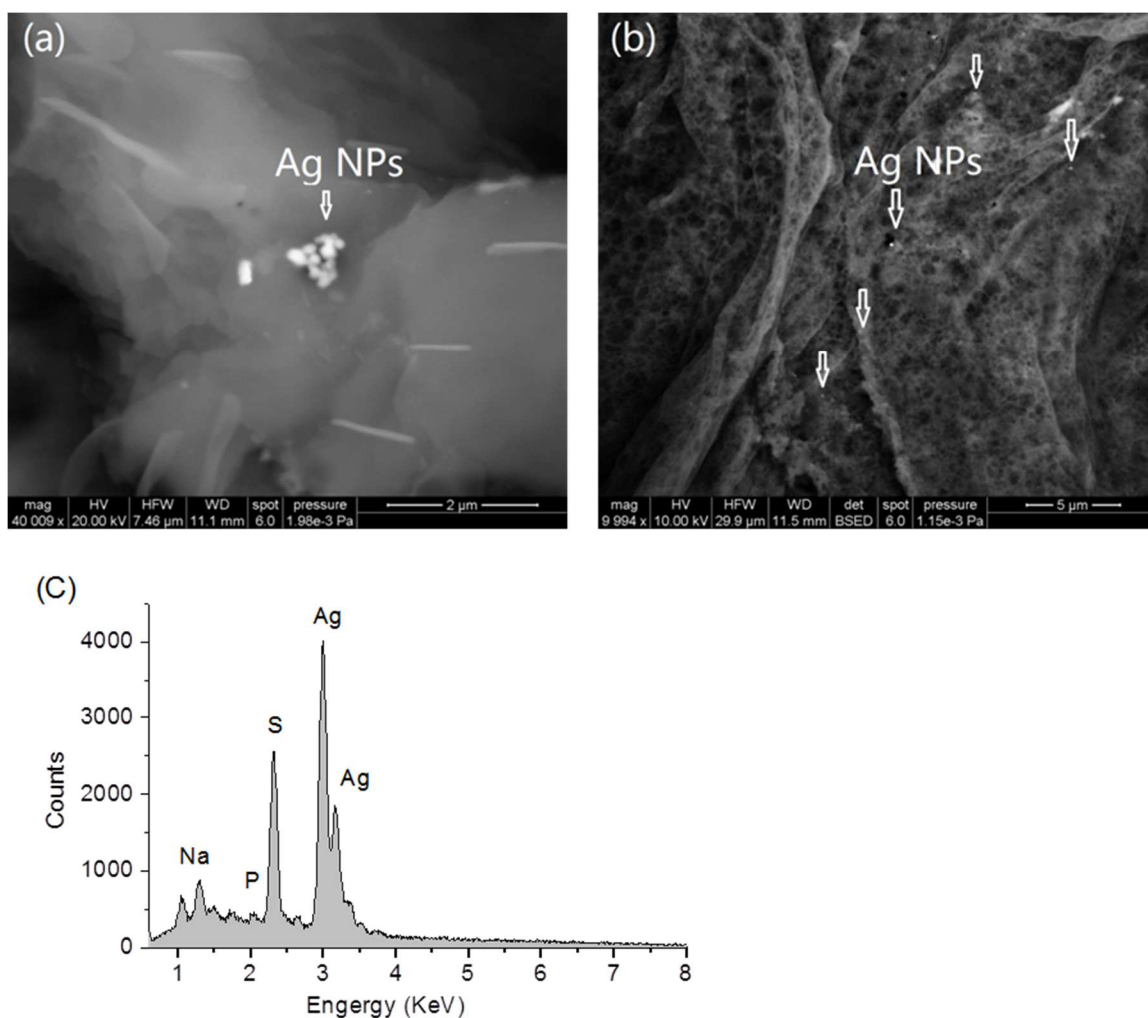
Figure 8 SEM characterizations of Ag NPs on pear tissues: (a) pear skin (b) pear pulp (C) A typical EDS profile for the nanoparticles attached on pear skin.

3.3.4 Quantification of Ag NPs in pears by ICP-OES

The concentrations of silver element in pear samples, contributed by the added Ag NPs and naturally existing silver in the pear, were determined by ICP-OES. Trace amounts of silver might be naturally present in pears due to the adsorption of silver from water and soil. As expected, 45.0 µg·kg^{-1} of silver was detected in the control samples. As shown in Figure 9, there is a linear relationship between the added values and the predicted values by ICP-OES, and it is evident that the recovered values of Ag NPs were all very close to the spiked

values. The slope is 1.03 and R^2 value is 0.983, indicating a good linearity and reliable prediction of this method. The detection limit of this method is 22.7 $\mu g \cdot kg^{-1}$ for Ag NPs in pear samples. In the recovery study, the concentration of Ag element in control samples was deducted accordingly because the naturally occurring Ag element in pear samples could contribute to the recovery rate. The recovery of Ag NPs was between 92.3% and 108.2% for the spiked samples (**Table 1**). The satisfactory recovery rate demonstrates that ICP-OES is a reliable method to quantify Ag NPs in pear samples.
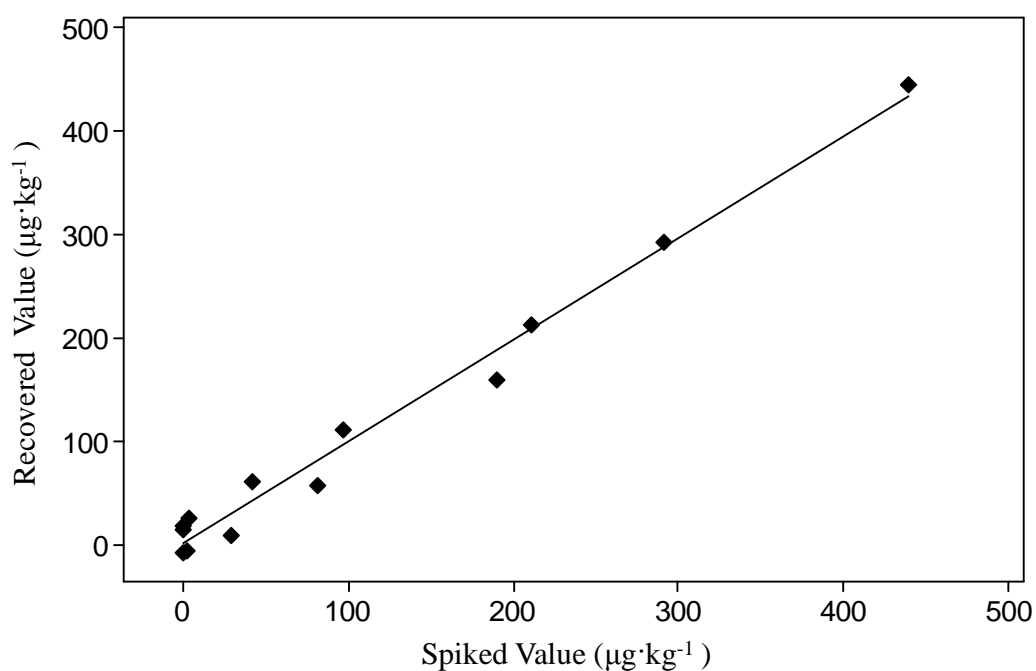
Figure 9 PLS regression fitting between the concentration predicted by ICP-OES and the spiked amount of Ag NPs in the pear samples (Y=1.03X-44.7, R^2=0.983, RMSEP=7.8).

Table 1 Recovery of Ag NPs in pear samples determined by ICP-OES

Spiked (µg·kg^{-1})	Quantified (µg·kg^{-1})	Recovery (%)
35.6	38.2±4.3	108.2%
92.9	91.7±10.5	98.7%
200.7	185.3±6.6	92.3%
297.3	310.7±8.1	104.5%
419.5	404.3±15.9	96.4%

3.3.5 Penetration studies of Ag NPs on the pear skin by ICP-OES

To simulate a real world situation of applied pesticides being washed off by rainwater, Ag NPs (20 and 70 nm) were applied on pears followed by thorough rinsing with deionized water. Figure 10 shows the relative content of Ag NPs in pear skin and the underneath pulp in different treatment times. The control samples were untreated pear skin and pulp, which were used to compare the accumulation and penetration of Ag NPs in treated samples. There is a significant difference in Ag content between the skin and pulp in the control group ($P < 0.05$). This is reasonable because the pear skin was directly exposed in the environment and was apt to adsorb the contaminants from the environment such as soil and air. The amounts of Ag in pear skin were enhanced by the treatment of Ag NPs after 4-day storage for both 20 and 70 nm Ag NPs. This indicates that some Ag NPs were firmly attached on pear skins after 4-day treatment and could not be removed by rinsing with water. But other weakly attached Ag NPs could be carried away by rainwater and migrate to the environment, thus contaminating the soil and water. For pear samples per se, the

residual Ag NPs on pear skin might not cause health problems to consumers because usually the pear skin is peeled off before consumption. Therefore, it would be interesting to investigate if Ag NPs could penetrate the pear skin and into the pulp.
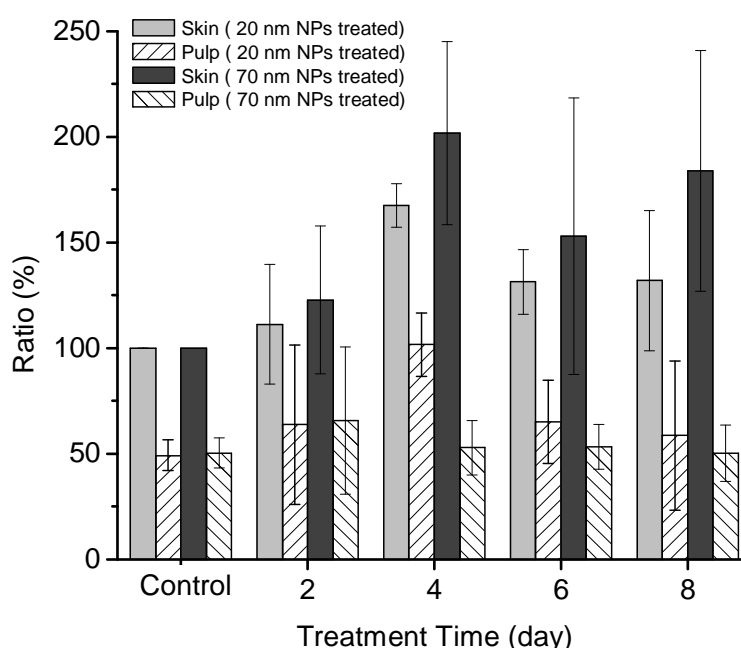
Figure 10 Relative content of Ag (20 nm and 70 nm) applied on the pear samples under different treatment time (Ratio=C_{sample}/$C_{control}$, where C_{sample} represents the concentration of Ag in samples and $C_{control}$ is the Ag concentration of pear skin in the control group).

The pear pulp right under the treated skin was sampled and subjected to ICP-OES measurement. The results show that the Ag content in the pulp increased by 50% four days after the treatment with 20 nm Ag NPs, indicating the potential penetration of Ag NPs into the pear pulp. This characteristic of Ag NPs is dangerous to consumers because NPs could translocate in the human body via direct digestion of pear pulps in the gastrointestinal tract (Delie 1998). The Ag content in the pulp was slightly reduced after 6-day and 8-day treatments,

which may be caused by further penetration of Ag NPs into the pear pulp or the translocation of Ag NPs to the surrounding pulp tissue. However, no increase was observed in the pear pulp samples treated with 70 nm Ag NPs. The concentration of 70 nm Ag NPs in the pear pulp maintained at the same level as that of the control even 8 days after the treatment. This may be due to the fact that 20 nm Ag NPs have a much smaller particle size than 70 nm NPs, which facilitated the penetration of Ag NPs into pear skin and translocation to the pulp. This phenomenon agrees with other studies about the penetration of Ag NPs into the cell wall of bacteria (Sondi and Salopek-Sondi 2004; Pal and others 2007). Previous studies have shown that the antibacterial ability of smaller NPs is much stronger than that of larger NPs due to the easier penetration of smaller NPs. Therefore, smaller NPs may be more harmful to consumers than larger counterparts. From this standpoint, the use of nanosilver pesticides in food crops should be carefully regulated.

3.4 Summary

The contamination of Ag NPs in pears was investigated in this study. The size, shape, and other properties of Ag NPs in solution or in pear tissues were characterized by Zetasizer, TEM, SEM, and EDS. The quantification of Ag NPs in pear samples was performed by ICP-OES. There was a good linear relationship between the recovered and spiked values of Ag NPs ($R^2 = 0.983$) with a detection limit of 22.7 $\mu g \cdot kg^{-1}$, demonstrating that ICP-OES is an accurate method for quantification of Ag NPs in pear samples. Moreover, the attachment and penetration of Ag NPs in pears were also investigated in this study. It was found that both 20 and 70 nm Ag NPs were still attached on the pear skin after 4 days

of treatment followed by rinsing with deionized water. The results reveal that 20 nm Ag NPs could penetrate the pear skin and pulp, while 70 nm Ag NPs did not. This study provides a promising approach for detection, characterization, and quantification of Ag NPs in food crops or other agricultural products. Compared with other methods such as FFF, HDC, and DLS, the advantage of the proposed method using a combination of techniques is that it cannot only detect, characterize, and quantify Ag NPs but also directly visualize the penetration of NPs in food tissues. Future research is needed to study the contamination and penetration of different type of nanoparticles on other fruits, crops, and agricultural products.

CHAPTER 4

Application of Au NPs and DLS to Detect Aflatoxin

4.1 Introduction

Aflatoxin M1 (AFM), a hydroxylated metabolite of aflatoxin B1, is often found in milk from animals fed with aflatoxin B1-contaminated feeds (Galvano and others 1996; Prandini and others 2009). AFM can also be found in a variety of dairy products such as cheese, yogurt, and infant formula due to its resistance to heat treatment (Stoloff and others 1975). AFM is a carcinogenic, genotoxic, and immunosuppressive compound. Therefore, the contamination of foods by AFM could pose a serious risk to public health, especially to the milk consumers (Reddy and others 2010; Chu 1991; Eaton and Gallagher 1994). In 1977, the U.S. Food and Drug Administration (FDA) established a strict action level of 500 ng·L^{-1} for AFM in fluid milk (Wood and Trucksess 1998).

Currently, several qualitative and quantitative methods have been developed to detect AFM in milk and other dairy products (Iha and others 2011; Rodriguez Velasco and others 2003; Wang and others 2011). Among them, thin layer chromatography and immunochromatographic assay are the most commonly used methods for rapid qualitative detection and semi-quantification of aflatoxins (Iha and others 2011; Wang and others 2011; Xiulan and others 2006). In addition, some biosensors have also been developed to analyze the AFM, including electrochemical immunochip sensor and DNA-based electrochemical membrane (Banitaba and others 2011; Siontorou and others 1998; Tombelli and others 2009). The quantification of AFM is usually conducted

by high performance liquid chromatography (HPLC) and enzyme-linked immunosorbent assay (ELISA) (Rodriguez Velasco and others 2003; Bognanno and others 2006; Santini and others 2010). The HPLC fluorimetric detection method can quantify AFM with high accuracy and a very low detection limit, but it requires complex and laborious pretreatments of samples, such as defatting of milk and subsequent extraction of AFM by methanol or immunoaffinity columns (Hussain and others 2010). The ELISA methods employ a direct competition of AFM and AFM-HRP (horseradish peroxidase) for binding sites of the antibody that are coated on microtiter wells. Compared to HPLC methods, ELISA requires less sample pretreatment procedures and has higher throughput (Zheng and others 2006). It is now commonly used in the AFM analysis. However, the ELISA still requires 30 – 60 min incubation time for the equilibrium of antibody-antigen reaction, 15 min for the development of color, and around 10 min for spectrophotometric assay (Pei and others 2009).

Dynamic light scattering (DLS) is a technique that can be used to measure the concentration and hydrodynamic diameter of micro- and nanoparticles dispersed in water solution. The detection limit could be as low as 5.95×10^{-13} M using 40 nm Au NPs (Jans and others 2009). Due to high sensitivity, simple operation, and rapid data acquisition, DLS technique coupled with Au nanoprobes is becoming one of the most widely used methods for detection of chemical and biological species (Dai and others 2008). For example, DLS has been used to diagnose prostate cancer by correlating the average size of nanoprobes with the concentration of prostate specific antigen (Liu and others 2008). But it is difficult to directly apply this method for qualification of AFM because AFM could not be sandwiched by antibody-modified nanoprobes.

However, the correlation of DLS intensity with the concentration of Au NPs opens a new route for us to detect AFM using Au nanoprobes modified with competing antigen.

Herein we aim to develop a rapid detection method for AFM by DLS coupled with Au nanoprobes and magnetic beads. Gold NPs were labeled with the conjugate of AFM and bovine serum albumin (AFM-BSA). The AFM-BSA can be anchored on the surface of Au NPs through abundant surface lysine groups of AFM-BSA (Shang and others 2007). In addition, the anti-AFM antibody could be easily linked on the surface of magnetic beads by oriented coupling effect of recombinant protein G (Radoi and others 2008). Unlike the immobilized antibody of conventional ELISA, these antibody-modified magnetic beads act as small "hunters" and can rapidly capture AFM when they are dispersed in the sample solution containing AFM, therefore reducing the incubation time. As illustrated in Figure 11, the AFM competes with Au nanoprobes for the binding sites of antibody on magnetic beads. After incubation, the bulk solution was separated from the magnetic beads by a magnet and directly transferred into a cuvette for DLS analysis. The DLS intensity of nanoprobe in bulk solution is positively proportional to the concentration of AFM in sample solution.
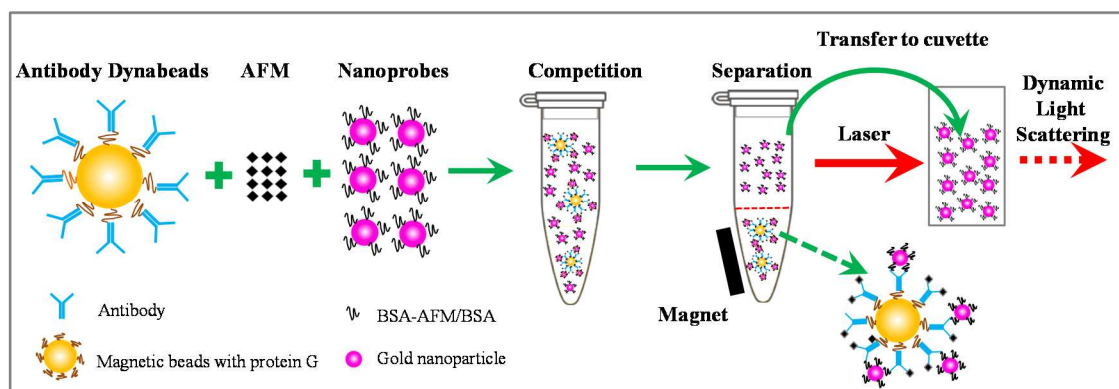
Figure 11 Scheme: detection of AFM by dynamic light scattering (DLS) using magnetic beads separation and Au nanoprobes.

4.2 Materials & Methods

4.2.1 Materials and chemicals

An immunoprecipitation kit and a magnet were obtained from Invitrogen (Carlsbad, CA, USA). This kit contained 2 mL of magnetic beads protein G, 16 mL of antibody binding and washing buffer, 28 mL washing buffer and 1 mL of elution buffer. A rabbit polyclonal antibody to AFM (100 μL) was purchased from Antibody-online (Atlanta, GA, USA). Bovine serum albumin (BSA), AFM, AFM-BSA conjugate (4-8 mol AFM per mol BSA), disodium hydrogen phosphate, sodium dihydrogen phosphate, sodium citrate, and gold chloride (30 *wt.*% in HCl) were purchased from Sigma-Aldrich (St. Louis, MO, USA) and used without further purification. Tween 20, 4-mercaptopyridine and cuvettes were obtained from Fisher Scientific (Rochester, NY, USA).

4.2.2 Fabrication of Au NPs and Au nanoprobes

Gold NPs with average diameter of 32 nm were fabricated by the citrate reduction method.(Frens 1973) Specifically, 250 mL ultrapure water was stirred and heated to boiling temperature on a magnet stirrer/hot plate. $HAuCl_4$ (40 μL) was then added to the boiling water. Subsequently, 2.7 mL sodium citrate solution (1 *wt.*%) was injected into the flask to reduce $HAuCl_4$ to Au NPs. The mixture was boiled for 5 min and then cooled to room temperature. The as-prepared Au NPs (0.5 mL) and AFM-BSA (5 nM, 0.5 mL) solution were thoroughly mixed in a 1.5 mL centrifuge tube. After 40 min, 100 μL of 1% BSA solution was added to prevent the aggregation of NPs and block the bare surface of NPs. Then, 200 μL of 4-mercaptopyridine (10 μM) were added to the mixture to further

block the surface of Au NPs. After 20 min incubation at room temperature, the excess 4-mercaptopyridine, BSA, and AFM-BSA conjugate were removed by centrifugation for 4 min at 8400 rpm (Eppendorf MiniSpin, Hamburg, Germany). Following the removal of the supernatant, the red oily precipitate was dispersed in 0.5 mL of phosphate buffer solution (PBS, pH 7.4, 10 mM) and subjected to a second centrifugation. The nanoprobes were finally dispersed in 0.5 mL PBS and stored at 4 °C.

4.2.3 Preparation of antibody-magnetic beads complex

A volume of 15.0 μL of magnetic beads was transferred to a 1.5 mL centrifuge tube. The magnetic beads were washed three times by the antibody binding and washing buffer. The magnetic beads were then suspended in 0.5 mL of antibody solution (Dilution 1:3000). The magnetic beads were incubated for 60 min with 300 rpm rotation at room temperature. After incubation, the magnetic beads were washed three times by washing buffer and finally suspended in 1.5 mL of washing buffer. The fragment crystallizable region (Fc region) of antibody was successfully attached on the magnetic beads by the coupling of recombinant protein G. The antibody-magnetic beads complex was prepared freshly to avoid the loss of activity during storage.

4.2.4 Analysis of AFM in PBS and milk

An aliquot of antibody magnetic beads (100 μL) was transferred to a 1.5 mL tube. The magnetic beads were separated from the bulk solution by a magnet. After removing the liquid, 100 μL of AFM standard solution (0 - 2000 ng·L^{-1}) and 60 μL of nanoprobe solution were added in the tube. The mixtures were

incubated at room temperature for 15 min with a rotation speed of 300 rpm to allow for full competition of AFM and AFM-BSA modified nanoprobes. The magnetic beads were then absorbed tightly at the bottom of tube caused by magnetic attraction force from the magnet. The bulk solution (100 µL) was directly transferred into a cuvette pre-filled with 1.2 mL high purity water for DLS analysis.

Skim milk was purchased from a local grocery store and spiked with AFM standard solution (v/v: 9:1). The analysis of skim milk was slightly different from that in PBS to avoid potential interaction between Au nanoprobes and milk proteins. First, 100 µL solution of antibody modified magnetic beads was added into spiked milk (100 µL) and incubated for 15 min at room temperature to capture AFM. The magnetic beads were then washed four times by antibody washing buffer (PBS, pH 7.4, 10 mM). Nanoprobe solution (60 µL) and PBS (100 µL) was subsequently added in the tube and incubated at room temperature for 25 min with rotation. After separation from magnetic beads, the bulk solution was subjected to DLS analysis as described above.

DLS measurements were performed at 25.0 ± 0.1 ^{o}C using a Malvern ZS ZEN 3600 system (Malvern, Worcestershire, UK) equipped with a red laser (633 nm). During the measurement, light from laser was directed and focused on the cuvette with 1.2 mL sample solution. The DLS signals were collected by a photodiode detector (Malvern, Worcestershire, UK) and processed by Malvern Zetasizer nanoapplication software. For each sample, two DLS measurements were conducted with at least 12 runs and each run lasted 10 s.

4.2.5 Transmission electron microscopy (TEM) analysis

TEM (JEOL 1400, Tokyo, Japan) was used to visualize the reaction between Au nanoprobes and antibody on magnetic beads. After being incubated as described in the section *2.4*, the magnetic beads were washed three times by PBS (pH = 7.4, 10 mM) and re-dispersed in 100 μL of PBS. A drop of magnetic beads solution (2 μL) was deposited on carbon side of copper/carbon grid and the grid was dried at room temperature for characterization by TEM.

4.2.6 Data analysis

The OriginPro software (version 8.0, OriginLab, MA, USA) was used to analyze the data. The inhibition value was calculated as the following equation:

$$\% \, Inhibition = \frac{I - I_0}{I_{Sat} - I_0} \times 100\% \qquad (3\text{-}1)$$

where I is the DLS intensity obtained from different concentration of AFM, I_{Sat} and I_0 are the DLS intensities corresponding to the saturating and non-competitor antigen, respectively. The limit of detection (LOD) was calculated as the concentration corresponding to 10% of inhibition value.[24]

4.3 Results & Discussions

4.3.1 Synthesis of Au nanoprobes

Figure 12 shows a TEM image of Au NPs and the hydrodynamic diameter distribution of pure Au NPs and AFM-BSA modified Au NPs. The as-prepared Au NPs were monodispersed with an average diameter of 32.0 ± 3.6 nm as tested by TEM (Figure 12a). The size of Au NPs plays an important role in developing a

detection method by DLS because larger NPs scatter light much stronger than smaller ones.[20] From Rayleigh approximation, the DLS intensity of 32 nm Au NPs is 1072 times higher than that of 10 nm NPs. Thus, it is important to use bigger NPs to enhance the sensitivity and lower the detection limit. Herein, 32 nm Au NPs were chosen to fabricate the nanoprobes because it could be easily synthesized by the citrate reduction method with high reproducibility. Seed-mediated growth method is usually needed to produce Au NPs with size of larger than 40 nm. The aspect ratio of Au NPs used in this study was from 1.04 to 1.22, showing a spherical shape of NPs. The AFM-BSA could bind uniformly on the surface of spherical Au NPs. It is also important to keep a narrow size distribution for the Au NPs to reduce the variation of DLS intensities.

The hydrodynamic diameter of Au NPs increased around 5 nm when AFM-BSA was added, indicating successful attachment of AFM-BSA on the surface of Au NPs (Figure 12b). There are abundant functional groups that enable the adsorption of AFM-BSA and BSA onto the surface of Au NPs, for example, amine groups from 60 surface lysines, imidazole group from histidine, and thiol group from cysteine. Therefore, BSA and AFM-BSA could spontaneously bind onto Au NPs by direct coupling of those functional groups with gold through electrostatic interactions and coordination effects (Brewer and others 2005). In addition, the hydrophobic interaction of BSA with gold also facilitated the immobilization of BSA on Au NPs. It is worth noting that two small peaks were also observed from 1.5 nm to 6 nm for both Au NPs and Au nanoprobes in DLS size distribution, which contributed around 10% for total DLS intensity. Similar peaks (<10 nm) were also reported for 60 nm Au NP which was tested by the same type of Zetasizer. A previous study proved that the small peak was caused by the rotation

motion of NPs because Au NPs were not perfectly spherical (Khlebtsov and Khlebtsov 2011). Likewise, a small peak observed in Figure 12b may be due to the rotation motion of the NPs that were not perfectly spherical.
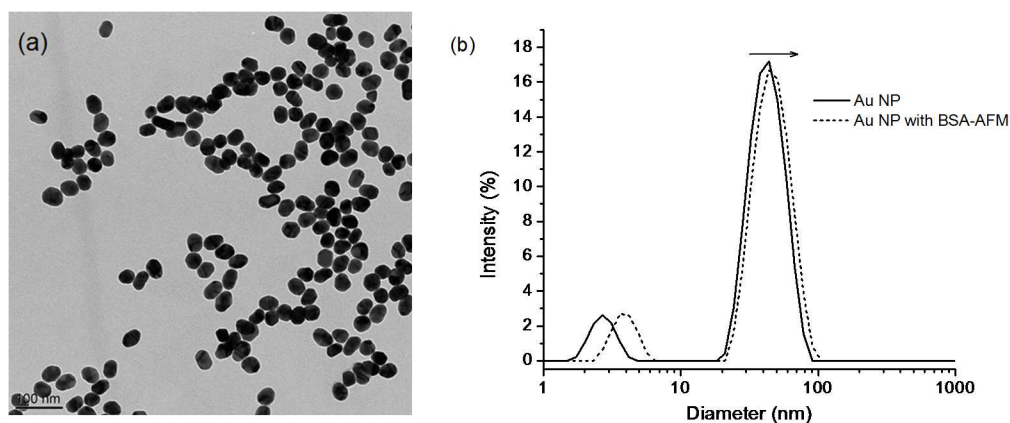
Figure 12 Characterization of Au NPs and Au nanoprobes: (a) TEM image of Au NPs (32.0 ± 3.6 nm); (b) size distribution of Au NPs without and with AFM-BSA as determined by DLS.

In this reaction, AFM-BSA acted as the competing antigen for AFM and BSA was used as a stabilizing agent for the nanoprobes. BSA could also block the interaction between Au NPs and antibodies on magnetic beads, thus reducing the non-specific adsorption of nanoprobes on magnetic beads. Due to the large size of BSA molecules, the surface of Au NPs may not be fully blocked by the addition of BSA. A small molecule with a thiol group, 4-mercaptopyridine, was added to fill the gaps between BSA molecules. During the double centrifugation, 4-mercaptopyridine also enhanced the stability of Au nanoprobes and prevented the aggregation of Au nanoprobes. Without using 4-mercaptopyridine, Au nanoprobes aggregated upon the first centrifugation even when 500 μL of BSA (5%) was present and could not be re-dispersed in solution. The possible explanation is that the AFM-BSA/BSA coated Au NP contacted closely with each other during the centrifugation. The BSA molecule penetrated the adjacent Au NP

surface, resulting in the coagulation of nanoprobes. On the contrary, this coagulation could be effectively prevented due to steric hindrance if 4-mercaptopyridine was covalently adsorbed on Au NPs.

4.3.2 Preparation of antibody-magnetic beads complex

Protein G, a surface protein expressed by *Streptococcus*, has been widely used for binding the Fc region of immunoglobulin G (IgG) (Bjorck and Kronvall 1984). The protein G has great affinity to polyclonal IgG of rabbit, goat, rat, and mouse. In the present study, a recombinant protein G was used to immobilize the anti-AFM antibody on the surface of magnetic beads. The nanoprobes would not bind with recombinant protein G due to repulsion between hydrophilic surface of protein G and hydrophobic surface of BSA. The optimum pH is 5.0 for the coupling reaction of antibody and protein G while the antibody-antigen reaction is favored at pH 7.0. Therefore, it is necessary to adjust the pH by washing the magnetic beads with PBS of pH 7.4.

4.3.3 Correlation of DLS intensity with concentration of nanoprobes

Figure 13 shows a linear relationship between DLS intensities and the concentrations of Au nanoprobes (R^2 value = 0.995). In this situation, the total intensities were used although there is a small peak from 1.5 – 6 nm (~10% of total intensity) that is also from nanoprobes as mentioned above. The standard deviations of DLS intensities were very small for the tested concentrations. These results indicate that DLS intensity could be used to precisely predict the concentration of nanoprobes. With the protection of AFM-BSA/BSA, the

nanoprobes were less liable to aggregate when dispersed in water solution, thus enabling the accurate detection of AFM by DLS.
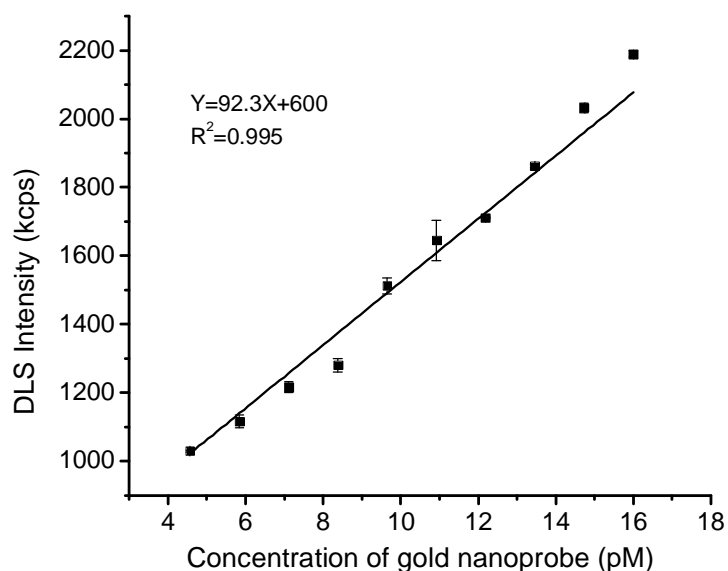
Figure 13 The linear relationship between DLS intensity and the concentration of Au nanoprobes.

4.3.4 Optimization of the incubation time

Figure 14 shows the changes of DLS intensity during different incubation times when the nanoprobes were incubated with antibody modified magnetic beads in PBS. It was observed that the DLS intensity decreased with increased incubation time. The results indicate that Au nanoprobes were gradually adsorbed on the magnetic beads, resulting in lower concentration of nanoprobes in bulk solution. The DLS intensity decreased rapidly in the first 15 min while changed slowly between 15 and 25 min. The final equilibrium of antibody-antigen reaction might not be reached within 15 min. But in this study, 15 min was selected as the optimum incubation time because a small difference was observed for the DLS intensity from 15 to 25 min. In conventional ELISA, the specific antibody is restrained on a small area of microtiter wells and stayed

static in the sample solution. The antibody waits for antigen to be captured in the reaction (Pei and others 2009). On the contrary, in this experimental design, the antibody on the magnetic beads could move along with the movement of the antibody-magnetic beads complex. There were tremendous amounts of micro-sized magnetic beads dispersed in the solution to hunt for AFM and nanoprobes. Meanwhile, the large surface area of magnetic beads also facilitated the interaction of antibody/antigen at room temperature. The incubation time was thus reduced for the aforementioned reasons. The optimized incubation time was 15 min based on the antibody concentration used in this study.
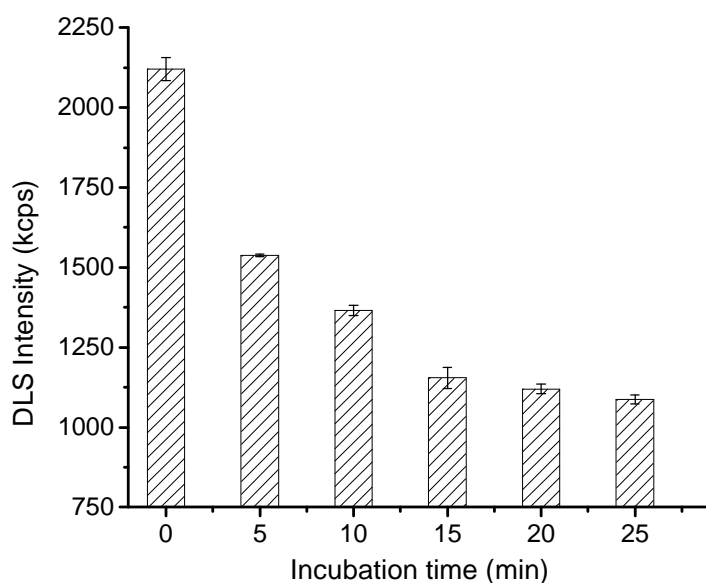
Figure 14 Optimization of incubation time for Au nanoprobes (60 μL) incubated with antibody modified magnetic beads in PBS (100 μL).

4.3.5 Measurement of AFM in PBS by DLS

MBISA is based on direct competition between the nanoprobes and AFM for the antibody binding sites on magnetic beads (Figure 11). The antibody has stronger affinity to AFM than AFM-BSA modified Au nanoprobes. The

concentration of nanoprobes attached on the surface of magnetic beads is negatively proportional to the concentration of AFM. Hence, the concentration of nanoprobes in bulk solution is positively proportional to the concentration of AFM in the sample solution. After competition with AFM, the nanoprobes in bulk solution could be separated from magnetic beads by a magnet and then measured by DLS. More importantly, the color development step and spectrophotometric analysis in conventional ELISA was substituted by direct DLS analysis of nanoprobes. The DLS measurement could be finished within a short time for each sample, thus significantly simplifying the analysis. Figure 15 shows the TEM images that were used to visualize and confirm the linkage of nanoprobes and antibody on magnetic beads. It was clearly shown that Au nanoprobes were adsorbed on the surface of magnetic beads due to antibody-antigen reaction, which proved that AFM-BSA modified Au NPs triggered antibody-antigen reaction and could be used as a probe for AFM.
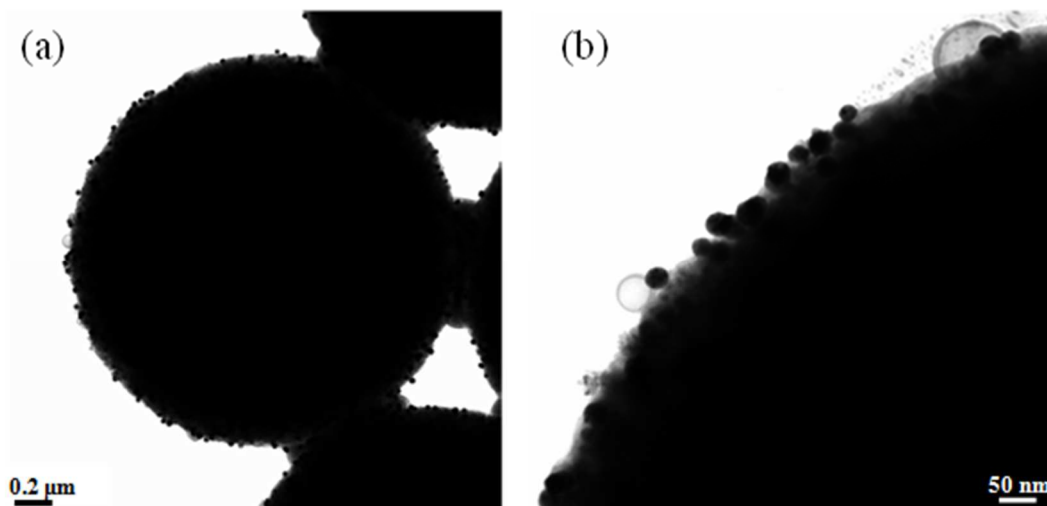
Figure 15 TEM images of nanoprobes attached on the magnetic beads with different magnifications: (a) scale bar: 0.2 μm; (b) scale bar: 50 nm.

Figure 16 shows a linear relationship between inhibition values and the concentrations of AFM in PBS (R^2 = 0.912). AFM has the preference to bind on the

antibody binding site due to higher affinity and lower steric hindrance compared to AFM-BSA immobilized on Au NPs. The antibody binding sites were first occupied by AFM. Thus, the number of remaining binding sites for nanoprobes was reduced when the concentration of AFM increased, resulting in a higher concentration of nanoprobes in the bulk solution. We also observed that there was no obvious change of DLS intensity when the concentration of AFM is higher than 1000 ng·L^{-1}. Thus, the saturation point of AFM is at 1000 ng·L^{-1} in PBS. Therefore, a linear relationship were only acquired for AFM between 0 and 1000 ng·L^{-1}. It is worth noting that the standard deviation of the inhibition values is relatively high, which may be due to the fact that the polyclonal antibody serum may contain a heterogeneous complex mixture of antibodies with different affinity to AFM. Additionally, it is difficult to fabricate Au NPs with uniform sizes. Although the standard deviation of Au NP size (32.0 nm) was only 3.6 nm, it still contributed to a relative standard deviation of 11.3%. The variation in size of Au NPs could impact the DLS intensity directly, which also contributed to high standard deviation of the inhibition values. The LOD in PBS was around 37.7 ng·L^{-1} as estimated by 10% of inhibition value.
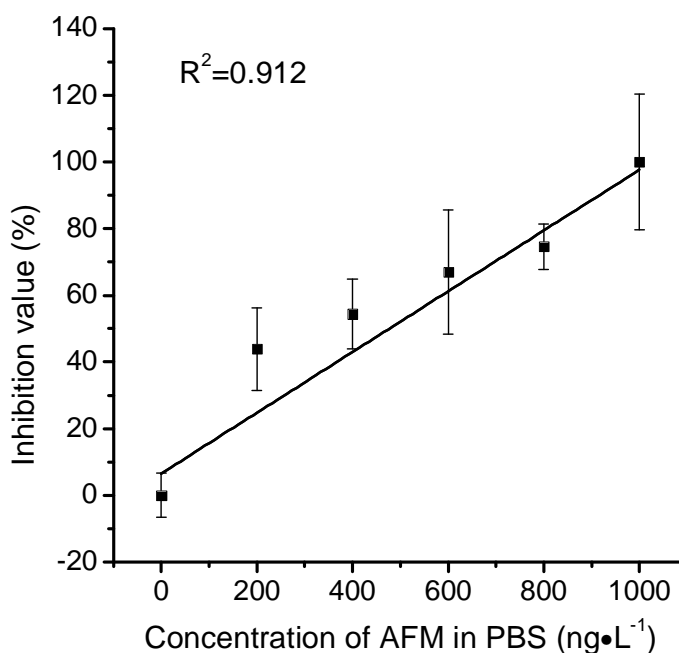
Figure 16 Linear relationship between the inhibition value and the concentration of AFM in PBS (0 - 1000 ng·L^{-1}).

4.3.6 Measurement of AFM in milk by DLS

Although a layer of BSA was formed on the surface of Au nanoprobes, proteins in milk might still be able to interact with Au NPs, which may influence the reaction between antibodies and nanoprobes, resulting in great interference for analysis. Therefore, the protocol for analysis of AFM in milk was modified to avoid this direct interaction between milk proteins and the nanoprobes. The magnetic beads were used to capture free AFM in milk and were thoroughly washed before incubation with Au nanoprobes.

Figure 17 shows a linear relationship between the inhibition value and the concentration of spiked AFM in skim milk. The linear range is much narrower than that in PBS. There were two reasons for this much lower saturation point (400 ng·L^{-1}) in milk compared to that in PBS (1000 ng·L^{-1}). First, the proteins or other components in milk, such as bovine IgG and mycotoxins, may occupy some

of the antibody binding sites on the magnetic beads, rendering a higher concentration of nanoprobes in the bulk solution and a lower saturation point. Second, the protein G on magnetic beads might also adsorb some milk proteins, burying some antibody binding sites and enhancing steric hindrance for nanoprobes. Therefore, a linear relationship was only observed between the inhibition value and the concentration of AFM (R^2 = 0.979) when the concentration was between 0 and 400 ng·L^{-1} instead of 0 - 1000 ng·L^{-1}. The LOD of AFM in milk was around 27.5 ng·L^{-1} as estimated by 10% of inhibition value. The disadvantage of this method for detecting AFM in milk is that the AFM has to be extracted by antibody-magnetic beads before competing with Au nanoprobes. The detection time was also increased due to matrix effects of milk. Nonetheless, the method is simple, specific, and opens a new route for detection of other mycotoxins in animal feeds and food samples.
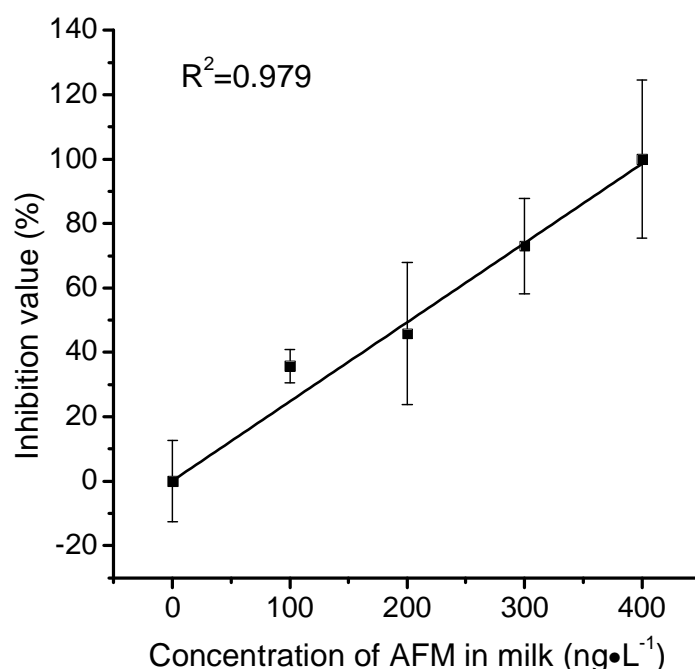
Figure 17 Linear relationship between the inhibition value and the concentration of AFM in skim milk (0 - 400 ng·L^{-1}).

4.4 Summary

The nanoprobes for AFM detection were successfully synthesized by AFM-BSA, BSA, 4-mercaptopyridine, and Au NPs. MBISA coupled with DLS was used to determine the concentration of AFM by competition between AFM and Au nanoprobes. Compared to conventional ELISA, MBISA does not require the color development step, thus simplifying the analysis of AFM. The incubation time was 15 min in this study. Moreover, TEM images prove that nanoprobes were successfully attached on the magnetic beads via reaction between antibodies and nanoprobes. The concentration of AFM in solution was positively proportional to the concentration of nanoprobes as determined by DLS. A linear relationship was observed between the inhibition values and the concentration of AFM for both PBS and spiked milk samples. The LOD was 37.7 ng·L^{-1} for AFM in PBS and 27.5 ng·L^{-1} in skim milk. This method could also be easily extended to rapid detection of other mycotoxins and biological species.

CHAPTER 5

Preparation of Vertically Aligned Au NR Arrays via Evaporation-Induced Self-Assembly

5.1 Introduction

The self-assembly of nanoscale materials is emerging as a popular and efficient method to fabricate ordered colloidal patterns (Dai and others 2011; Ko and others 2008; Prasad and others 2008; Grzelczak and others 2010; Jana 2004). Evaporation-induced self-assembly has been recognized as one of the most efficient and facile route to organize the nanoparticles and form various colloidal superstructures (Zhang and others 2010; Wang and Möhwald 2004; Lin and others 2005; Nie and others 2009; Gong and others 2012). Recently, the supercrystal of vertically aligned Au NRs has been assembled and attracted much attention due to its nearly perfect three-dimensional organization of Au NRs with uniform and intense electric field enhancement (Alvarez-Puebla and others 2011; Vigderman and others 2012). The supercrystals were used as substrates for surface enhanced Raman spectroscopy with high reproducibility and enhancement factor for rapid detection of prions in complex biological media. A monolayer of vertically aligned NRs has also been used to detect food contaminants in femtomolar concentrations (Peng and others 2013). There are a variety of potential applications using standing arrays of Au NRs, including plasmonic cavity resonator, light polarizer, and substrate for biosensing (Kabashin and others 2009; Lyvers and others 2008; Kullock and others 2008; Tserkezis and others 2009).

Several methods have been proposed to fabricate the standing Au NR arrays in macroscopic shape and local smectic order. For example, Au NRs were vertically aligned on a smooth surface with topographically patterned polydimethylsiloxane (PDMS) pillars (Nepal and others 2012). The PDMS pillars were used to regulate water evaporation and control the assembling of (1-mercaptoundec-11-yl)hexa(ethylene glycol) modified Au NRs in given locations. Standing Au NR arrays have also been fabricated by evaporating PEG-functionalized Au NR solutions on a micropatterned silicon slide that was placed vertically in an Eppendorf tube (Thai and others 2012). The disadvantage of this strategy is that it needs to graft Au NRs with specific ligands and pre-pattern the substrate to direct the NR assembling. In addition, highly monodispersed Au NRs were fabricated using a Gemini surfactant to direct the NR growth. The superlattices of standing Au NRs were formed on the silicon surface after the drying of NR droplets (Guerrero-Martínez and others 2009). However, it is complex and expensive to fabricate specific Gemini surfactant for highly monodispersed Au NRs.

Gold NRs, functionalized by thiol-terminated poly(N-vinylcarbazole) and thiol-terminated poly-styrene, were able to assemble in a side-by-side manner in a tetrahydrofuran (THF) solution (Petukhova and others 2012). After evaporating the THF solution, standing array of Au NRs was acquired at the bottom of the container. The interfacial assembly of Au NRs was also triggered by functionalizing Au NRs with small hydrophobic thiol molecules (Wei and Ge 2013a). The dodecanthiol-modified Au NRs could assemble into a monolayer of standing arrays at the water-air interface. In addition, Au NRs were also modified by a layer of OH-terminated hexa(ethylene glycol) alkanethiol in order to tune the

repulsive interaction during the evaporation-induced assembling (Xie and others 2011). The modified Au NRs could form symmetric circular or semicircular superlattices composed of multilayers of standing Au NRs. The only drawback of these methods is that Au NRs must be functionalized with thiol capping agents before assembling.

Vertically aligned monolayer of Au NRs were formed after drying the droplets of NR solution containing CTAB and NaCl at 21°C overnight (Peng and others 2013). However, the crystallization of NaCl could deteriorate the morphology of the self-assembled film. Another technique, controlled two-stage droplet evaporation method, has been proposed to fabricate standing Au NR monolayer on silicon surface (Xie and others 2013). In the first stage, a pinned edge was formed by rapid evaporation of the concentrated Au NR droplet. In the second stage, a monolayer of Au NRs was formed through slow evaporation of the droplet in the area defined by the pinned edge. This method is straightforward and easy to operate. However, it requires a high concentration of Au NRs (~30 nM) and most NRs were wasted in forming the pinned edge. Therefore, it is important to develop a simple and high-yield method to prepare standing Au NR arrays. In this study, we propose a novel and simple method to fabricate standing Au NR monolayer by controlling the evaporation rate of NR droplet in two steps to suppress the formation of coffee-ring structure and provide enough time for the monolayer assembling. The procedure does not need to functionalize Au NRs by thiolated ligands, synthesize strictly monodispersed Au NRs, or use highly concentrated Au NR solutions.

5.2 Material & Methods

5.2.1 Materials and chemicals

Hydrogen tetrachloroaurate solution (HAuCl$_4$, 30 *wt.*% in dilute HCl), silver nitrate, ascorbic acid, and cetyltrimethylammonium bromide (CTAB) were purchased from Sigma-Aldrich (St Louis, MO) and used without any purification. Silicon slides were purchased from Ted Pella (Redding, CA). All ultrapure water (18.2 MΩ/cm) was prepared from a Millipore water purification system (Milli-Q water system).

5.2.2 Synthesis of Au NRs

Gold NRs with aspect ratio of 2.0 were synthesized based on El-Sayed's method with slight modifications (Nikoobakht and El-Sayed 2003). The glassware was treated by aqua regia for 30 min to remove all metal residues before using. Briefly, the seed solution was prepared by mixing 1.9 mL of CTAB (0.2 M) with 0.10 mL of HAuCl$_4$ (5 mM) in a glass vial. Then 0.12 mL of freshly prepared ice-cold NaBH$_4$ (10 mM) was added into a glass vial, and the solution was mixed thoroughly by vigorous shaking. The seed solution could be used after 30-min incubation at room temperature. The growth solution was prepared by mixing 50 mL of CTAB solution (0.2 M) with 50 mL of 0.5 mM HAuCl$_4$ in a 150 mL flask. After that, 400 μL of 20 mM AgNO$_3$ and 550 μL of fresh-made ascorbic acid (0.1 M) were added into the mixture, and the mixture turned into colorless after stirring for 20-30 s. Subsequently, an aliquot of seed solution (200 μL) was injected into the growth solution with gentle stirring. The mixture was then incubated in 28.0°C water bath overnight without disturbing. The Au NRs with

desired longitudinal surface plasmon were obtained after aging the mixture for certain amount of time (~30 days) at room temperature.

5.2.3 Characterization of Au NRs by UV-vis and TEM

For UV-vis characterization, the Au NR solution was centrifuged twice and redispersed in pure water. The purified Au NR solution was transferred into a 2.8 mL cuvette and scanned by a Varian UV-vis spectrophotometer (Cary Bio 50, Agilent, CA). For characterization by transmission electron microscopy (TEM), Au NRs were purified by centrifugation and redispersion in pure water. After that, 2.0 μL of Au NRs was casted on the copper/carbon grids and dried at room temperature. The TEM images were taken by a JEOL electron microscopy (JEOL 1400) operated at an accelerating voltage of 120 kV.

5.2.4 Evaporation-induced assembling of standing Au NR arrays

The Au NR solution (10 mL, aspect ratio of 2.0) was centrifuged twice and redispersed in 2.0 mL of CTAB solution (2.5 mM). The concentration of Au NR was ~1.7 nM as determined by *Beer-Lambert Law* with extinction coefficient of 2.5×10^9 $M^{-1}cm^{-1}$.(Orendorff and Murphy 2006) After 60 s of sonication, five drops of NR solution (10 μL) were casted on the silicon substrate (1 cm × 5 cm) which was previously cleaned by water and ethanol. The silicon substrate was transferred onto a glass slide in a polystyrene petri dish with width of 94 mm and height of 15 mm (VWR International Co., PA, USA). Then, 200 μL of water was added into the petri dish to adjust the humidity (Figure 18). The petri dish was sealed by parafilm (PM-992, American National Can Co., WI, USA) and placed into an incubator. After 24 h, the droplets on the silicon shrank into smaller droplets

without forming coffee-rings. Subsequently, water was removed from the petri dish to allow further evaporation of the droplets. The petri dish were quickly sealed again by the parafilm and put back into an incubator. After another 36-48 h, the droplets would be completely dried and form a film containing standing NR arrays on the silicon surface. The NR film was characterized by an optical microscope and a FEI Quanta 600 FEG scanning electron microscope (FEI, Oregon, USA). The vertically aligned Au NRs with aspect ratio of 3.4 were assembled and characterized by the same procedure. In addition, the Au NRs with (aspect ratio of 3.4) were also incubated with 150 μL of water in petri dish. The water was not removed during the whole incubation period in order to generate a longer incubation time than the two-step method. The droplets of Au NR solution were completely dried after ~144 h of incubation.

Five drops of nanorod solution (10 μL/drop)

Silicon slide

Glass slide

Total: 200 μL free H_2O
100 μL H_2O at two corners

Height: 15 mm

Diameter: 94 mm
Polystyrene Petri dish
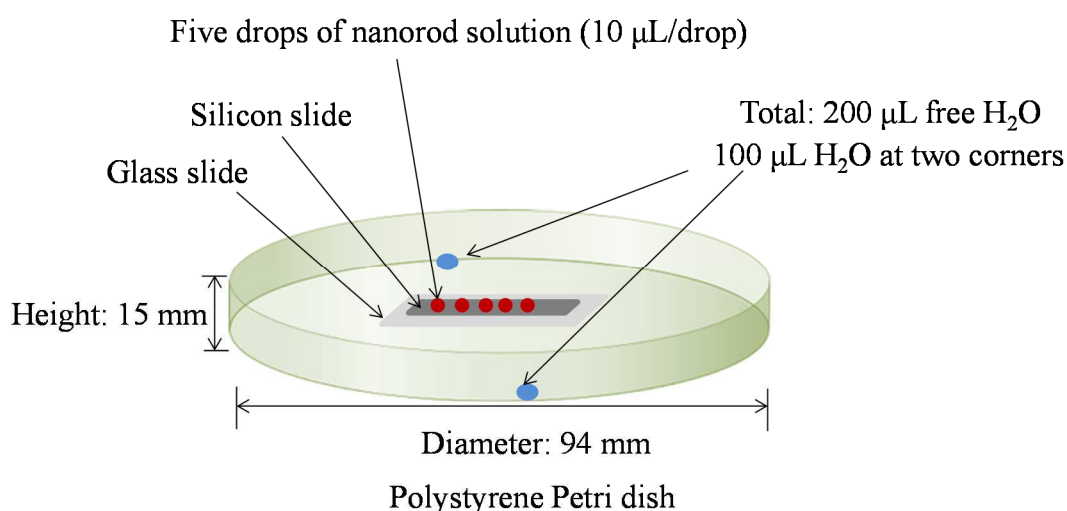
Figure 18 The sketch of the experimental setup in the present study.

The Au NRs with aspect ratio of 2.0 were also assembled for less than 12 h. First, the Au NRs were purified and redispersed as stated above. Then, one drop of the Au NR solution (10 μL) was casted on the silicon surface and placed on a glass slide in the petri dish. The petri dish was completely sealed by parafilm

and put in an incubator. The NR droplets were completely dried during 8-12 h. The lateral Au NR arrays were formed and characterized by optical microscope and SEM.

5.3 Results & Discussions

5.3.1 Preparation of standing Au NR arrays

As shown in Figure 19a, the droplets of CTAB-protected Au NR solution were incubated in a high humidity environment for 24 h. The high humidity is produced by adding 200 μL of water into the petri dish. The high humidity environment led to slow evaporation of the NR droplets and enabled the solvent to evaporate at the same speed from the contact line to the center of the droplet. The slow evaporation of solvent could suppress convections and prevent the NRs from flowing from the center to the contact line, thus avoiding the formation of a coffee-ring structure (Hu and Larson 2006). The solution shrank into a smaller droplet due to the homogenous evaporation speed on the entire surface of the droplet and the lack of pinned edge. In this stage, the concentration of CTAB was still very low, and all the Au NRs were well dispersed in the CTAB solution.
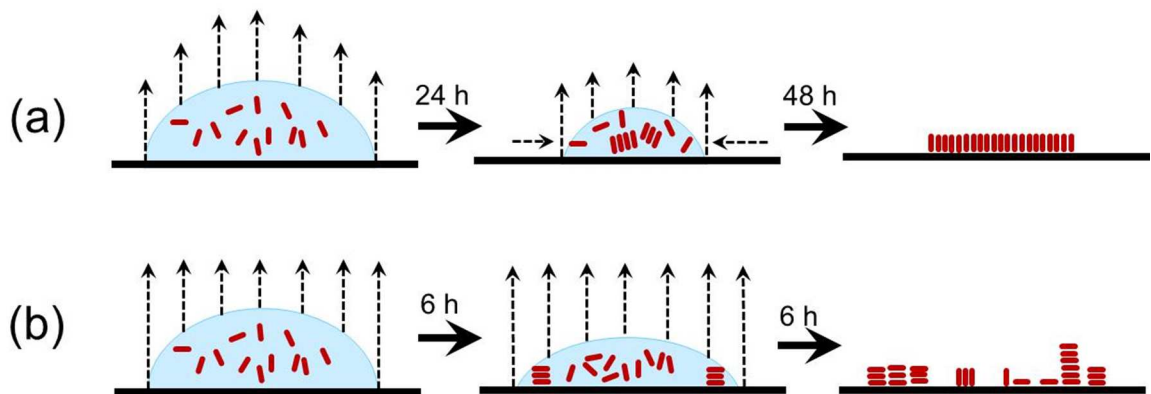
Figure 19 Fabrication of highly ordered Au NR arrays: (a) standing Au NR arrays prepared by evaporation-induced self-assembling for 72 h on silicon surface; (b) lateral Au NR arrays formed by evaporation-induced self-assembling for 12 h on silicon surface.

After the first stage, the remaining water was removed from the petri dish. The contracted droplets were allowed to evaporate for another 36 to 48 h for the complete drying of the droplets. At the second stage, Au NRs started to assemble in a side-by-side manner and formed small arrays when the CTAB reached a critical concentration (Xie and others 2013). The long period of the second stage provided enough time for all the NRs to find the best location to incorporate into arrays through side-by-side interactions and deposit as standing arrays on the silicon surface. On the contrary, lateral arrays of Au NRs were formed on the silicon when the total evaporation time was no more than 12 h (Figure 19b). No heavy shrinkage happened for the droplets due to fast evaporation of the solvent. In this circumstance, Au NRs started to precipitate even when the concentration of CTAB was still very low. The low concentration of CTAB is favorable for Au NRs to assemble in an end-to-end manner. Therefore, most of Au NRs were deposited as lateral arrays near the coffee ring area.

5.3.2 Evaporation-induced assembling of standing Au NR arrays

Figure 20a shows that the LSPR peak of Au NRs was ~610 nm. The length, width, and aspect ratio of Au NRs were 73.9 ± 7.3 nm, 36.6 ± 6.9 nm, and 2.0, respectively (Figure 20b). We employed an aging method to synthesize gold nanorods with LSPR of 610 nm. Firstly, gold nanorods with LSPR of 760 nm were synthesized based on the El-Sayed's method. Due to the presence of excessive amount of $HAuCl_4$ and ascorbic acid in the growth solution, the remaining gold ions could be reduced and deposited on the gold nanorods. Blue shifts of the LSPR were observed during the overgrowth of gold nanorods, indicating the decrease of aspect ratio of gold nanorods. The LSPR of gold nanorods could be

easily tuned by the overgrowth. Thus, NR-610 was obtained through aging the nanorod solution for 30 days.

This aging process was used to tune the aspect ratio of Au NRs to 2.0. During the aging process, no additional chemicals were added to modify the Au NRs in the solution. After the aging process, the Au NRs were purified by double centrifugation to remove silver nitrate, ascorbic acid, and CTAB. Then the Au NRs were redispersed in 2.5 mM of CTAB solution. The assembling behavior of Au NRs was determined by the ligands on the NR surface, aspect ratio, and the assembling procedure. The purpose of aging is to produce Au NRs with aspect ratio of 2.0. Without adding ligands to the Au NR surface during the aging, the aging time has no effect on the assembling behavior of Au NRs. Although Au NRs are not strictly monodispersed with uniform size distribution, the standing Au NR arrays are still able to form on the silicon using the proposed two-step method.
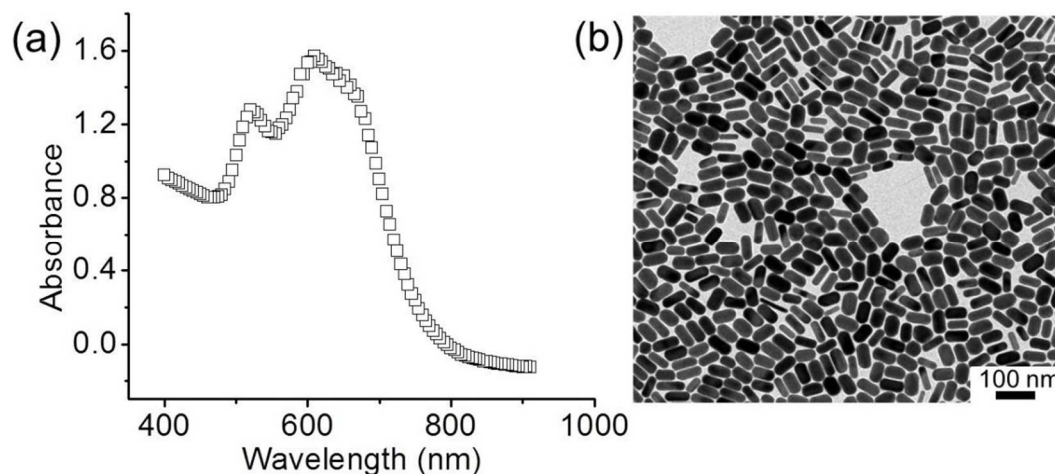
Figure 20 Characterization of Au NRs used for assembling: (a) UV-vis spectrum of purified Au NR in aqueous solution; (b) TEM image of purified Au NRs.

As shown in Figure 21a, the silicon was covered by numerous small round-shape islands. The islands at the edge show shiny golden color, indicating

that the islands are made of a layer of Au NRs. The islands at the center show rainbow colors, which was caused by the crystals of CTAB on the top of islands. Examination by SEM shows that the islands at the edge are much brighter than other islands, proving that CTAB were crystallized on the top of those dark islands (Figure 21b). In other words, the standing Au NR arrays were formed and deposited on the silicon before the crystallization of CTAB. The SEM image also shows that the average size of the islands is ~12.0 μm and almost all Au NRs are incorporated into the standing arrays. Figure 21c shows that all the NRs in the island are vertically aligned on the silicon surface. There are a few cracks inside the standing Au NR arrays, which was caused by adhesion force of the substrate and capillary force in the formation of liquid vapor meniscus during the last moment of drying. Figure 21d shows the SEM image at the pinned edge of the NR film. It could be observed that only a small amount of NRs were aligned horizontally at the edge. More importantly, the width of the pinned edge was less than 1.0 μm, indicating that only a very small amount of NRs were used to form the pinned edge.

In a previous report, a very high concentration of Au NRs were needed to fabricate the standing Au NRs, and most of the Au NRs were used to form the pinned edge.[24] However, the proposed method in this study does not require highly concentrated Au NRs and thus avoids the waste of the Au NR. A closer examination of NR arrays by SEM shows that Au NRs were assembled with hexagonal close-packed arrangement within the monolayer (Figure 21e). The SEM image of the crack also clearly shows the side view of the standing Au NRs. The Au NRs are perpendicularly standing on the silicon surface. These results indicate that standing arrays of Au NRs were acquired with high yield on the

silicon substrate by offering enough time for the side-by-side assembling at the second stage.
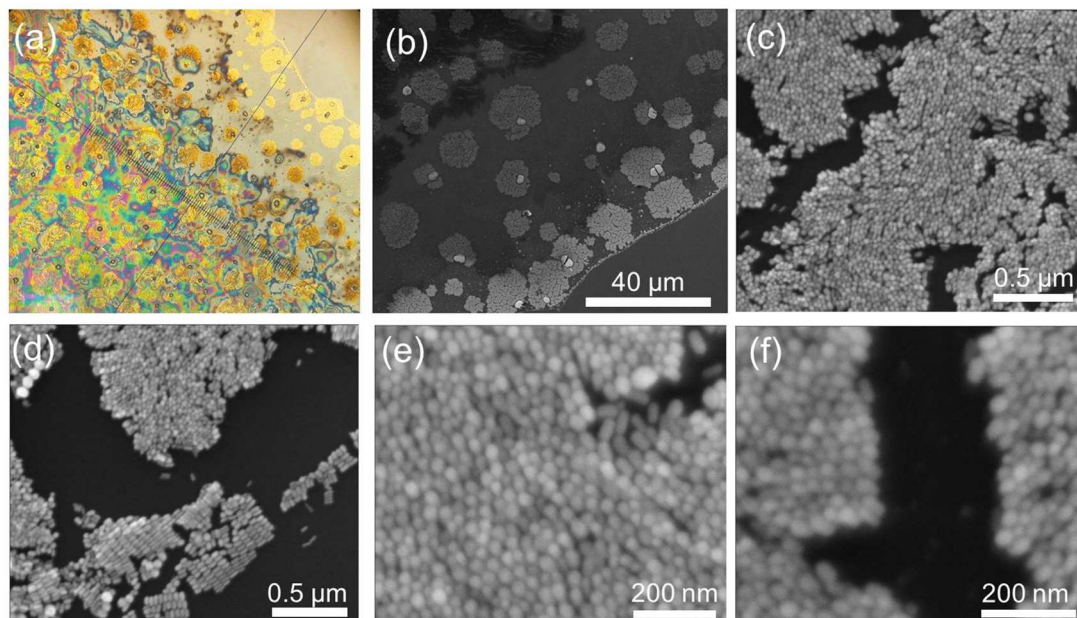
Figure 21 Characterization of the assembled Au NR arrays: (a) optical image of the standing Au NR arrays; (b) SEM image of the standing Au NR arrays; (c) SEM image of a single NR array; (d) SEM image of Au NR arrays near the pinned edge; (e) SEM image of a standing Au NR array with high magnification; (f) SEM image of a crack inside a standing Au NR array.

In addition, more NR islands have been selected from different locations and characterized by optical microscope and SEM (Figure 22). It can be observed that all of those NR islands have the exact same morphology with the vertically aligned Au NR island as shown in Figure 21. These results indicate that all of those NR islands were built by vertically aligned Au NRs. However, the Au NRs islands were not strictly monodispersed on the silicon surface. Those standing NR islands tend to connect with each other near the center of the droplet (Figure 23). This phenomenon might be caused by the extremely slow evaporation of the solvent, resulting in a lack of convection inside the droplet and preventing the movement of NRs from center to the edge area. Furthermore, a thick layer of CTAB was formed on the top of the standing Au NR arrays due to the contraction

of the droplet during assembling. This is a drawback of this method. To explore the application of such NR arrays, an appropriate method is needed to remove the thick layer of CTAB without damaging the morphology of the Au NRs.
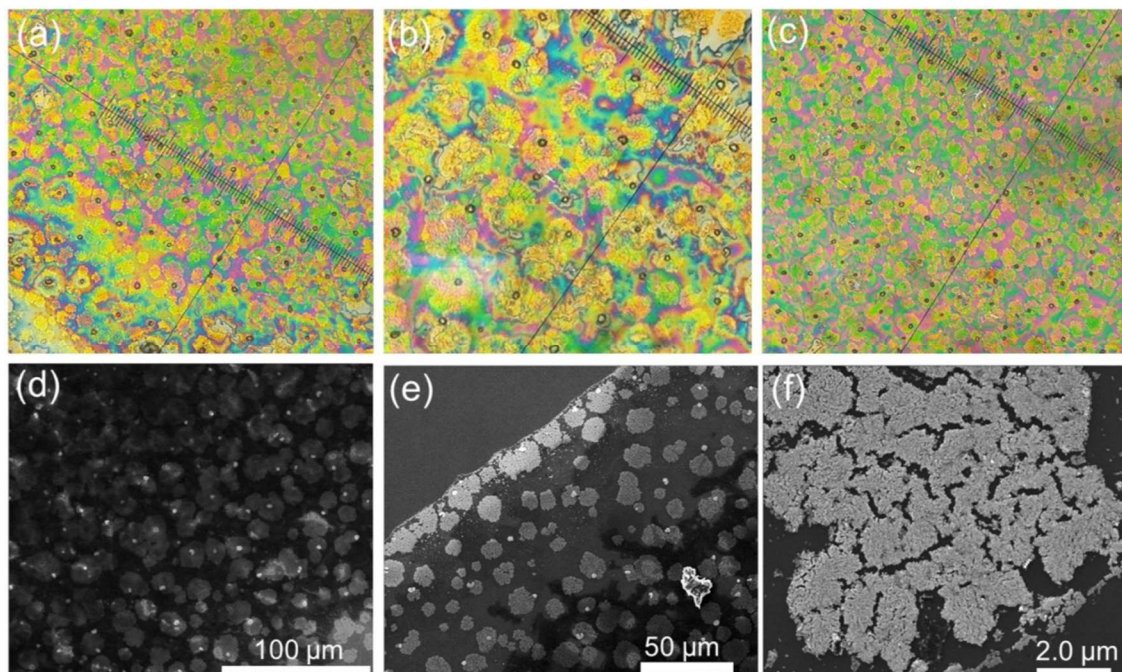
Figure 22 Characterization of Au NR arrays: (a), (b), and (c) optical images of Au NR islands at different areas; (d), (e), and (f) SEM images of Au NR islands with different magnifications.
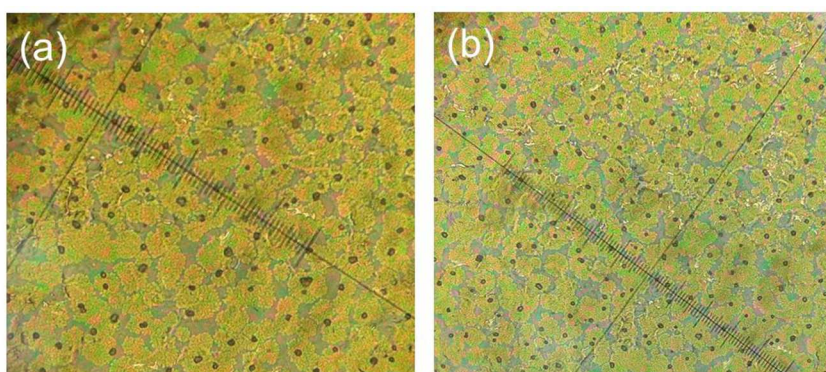
Figure 23 Optical images of Au NR islands near center of the droplet.

Figure 24 shows the optical images and SEM images of Au NR film when the NR solution was completely dried in less than 12 h. The optical image of the NR film is apparently different from that of standing NR film. A great number of

golden shiny particles were observed under the optical microscope (Figure 24b and 24c). SEM image shows that the particles are in a leaf shape with an average length of 5.0 μm and width of 0.8 μm. Because of short evaporation period, Au NR leaves were formed during the crystallization of CTAB. The leaves are either embedded inside the CTAB layer or located on the top of the CTAB layer (Figure 24d). There was no enough time left for the Au NRs to assemble into a large monolayer in a side-by-side manner and deposit on the silicon as standing arrays after CTAB reaches to the critical concentration. Instead, Au NRs formed into multilayer of lateral arrays at the same time when CTAB was crystallized (Figure 24e and 24f). This phenomenon suggests that it is necessary to keep a low evaporation speed to provide enough time for Au NRs to assemble into a standing monolayer. Otherwise, Au NRs would be aligned horizontally on the silicon surface.
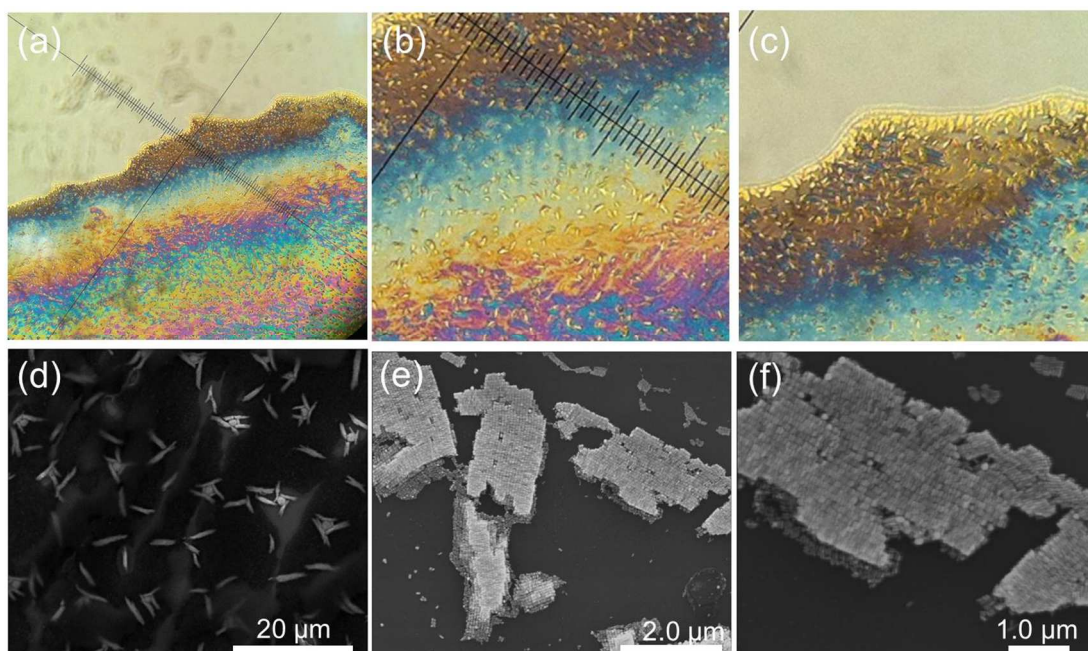
Figure 24 Characterization of lateral Au NR arrays: (a) optical image of Au NR leaves at the pinned edge; (b) optical image of Au NR leaves with higher magnification near the pinned edge; (c) optical image of Au NR leaves with higher magnification at the pinned edge; (d) SEM image of Au NR leaves near the pinned edge; (e) SEM image of Au NR leaves at the pinned edge; (f) SEM image of the Au NR leaf with higher magnification at the pinned edge.

As a comparison, another method was also used to fabricate standing Au NR arrays. PEG-modified Au NRs were previously used to assemble standing Au NRs on patterned surface (Thai and others 2012). However, it was found that mPEG-protected Au NRs were aligned horizontally on the un-patterned silicon due to the large repulsion between Au NRs (Figure 25). The result reveals that it is difficult to fabricate large scale of standing Au NR arrays for the NRs with large length variations using one-step fast evaporation method (<12 h) by simply modifying the Au NRs with ligands. The ligand must be carefully chosen to adjust the interactions between Au NRs in order to acquire the standing Au NR arrays. The functionalization of the Au NRs by thiolated ligands also makes the preparation of standing arrays much more complex compare to the present method. After the functionalization, Au NRs have to be purified by a few rounds of centrifugations, leading to the loss of Au NRs. However, there are still many advantages of using Au NRs modified by thiolated ligands to build the standing arrays. These NRs can be used to fabricate highly monodispersed standing arrays with multilayers on patterned silicon/gold surface. The multilayer of standing Au NRs can generate very strong electromagnetic fields and provide a high enhancement factor for SERS applications. As comparison, a monolayer of standing NR arrays was fabricated by our method. Second, the Au NRs modified by thiolated ligands could be assembled into superlattices by the interaction of the thiolated ligands without using 2.5 mM of CTAB solution. This can also avoid the formation of a thick layer of CTAB crystals on the top of the standing Au NRs as compared to our method.
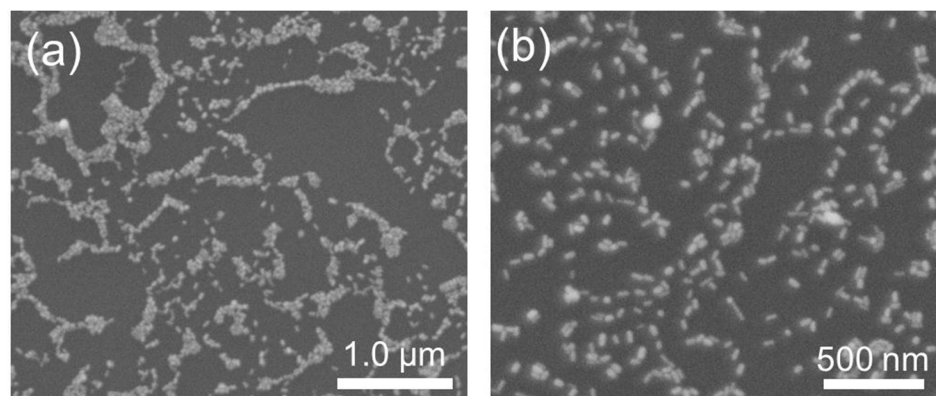
Figure 25 SEM characterization of Au NR film assembled using mPEG-modified Au NRs in aqueous solution: (a) and (b) are randomly selected locations across the Au NR film.

5.3.3 Assembling of Au NRs with aspect ratio of 3.4 by two-step method

Gold NRs, with a higher aspect ratio of 3.4, were also employed as building blocks to create standing Au NR arrays using the proposed two-step method. As shown in Figure 26, Au NRs were assembled into a monolayer in island shape. The diameter of the islands is the same as the island formed by short NRs with aspect ratio of 2.0. It is worth noting that there is a great number of leaf-shape particles present in the film. As mentioned above, the leaf-shape particles are composed of Au NRs that are aligned horizontally. It has been proven that lower aspect ratio is more advantageous for producing standing NR arrays (Xie and others 2013). Therefore, it is reasonable for the presence of the non-vertically aligned arrays in the film. Nonetheless, most of Au NRs are still aligned vertically on the silicon substrates (~60%). Examination of a single island shows that there were also a few cracks in the island (Figure 26b and 26c). Nearly all Au NRs in the island were vertically aligned on the silicon substrate (Figure 26d and 26e). In addition, it is clearly shown that Au NRs were hexagonally packed on the silicon surface with their tips facing up (Figure 26f). The results show that the proposed two-step methods could also be applied to assemble Au NRs with

longer aspect ratio. This method might also be extended to assemble other types of NRs into standing arrays.
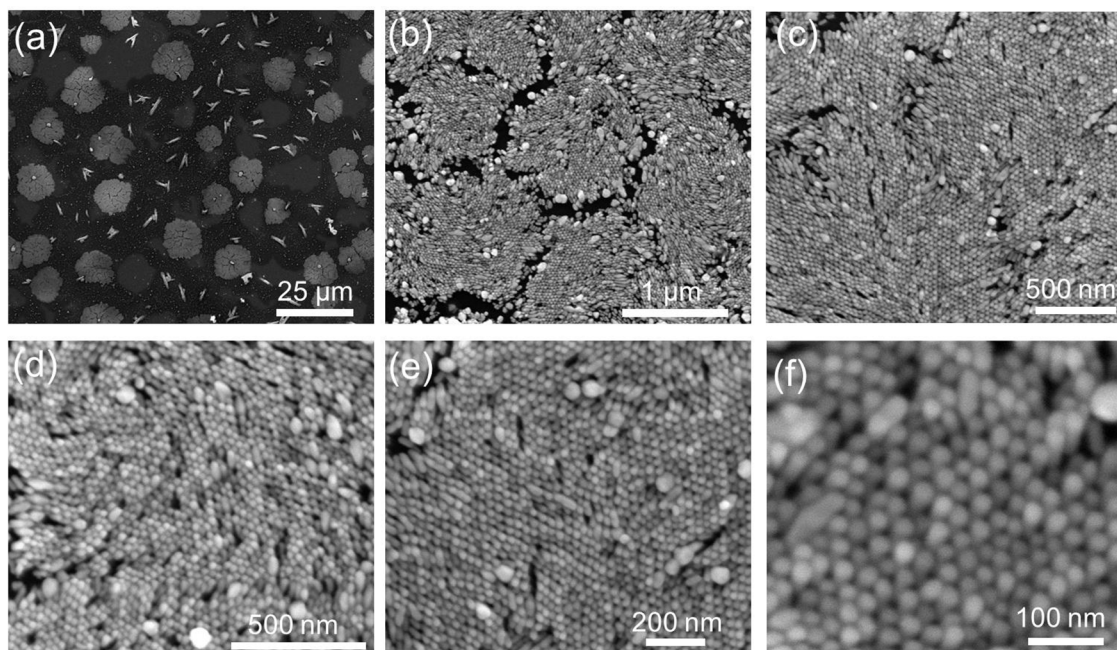
Figure 26 Characterization of the standing Au NR arrays prepared by NRs with LSPR of 720 nm: (a) SEM image of the Au NR arrays; (b) SEM image of a single array; (c) SEM image obtained at the center of an Au NR array; (d), (e) and (f) SEM image of standing Au NRs with higher magnifications.

In addition, we increased the incubation time to improve the assembling efficiency for the Au NRs with aspect ratio of 3.4. Without removing the water in the petri dish during the whole incubation period, the Au NR droplets were completely dried after ~144 h of incubation. As shown in Figure 27, vertically aligned Au NRs were formed on the silicon surface by extending the incubation time to ~144 h in one step. The standing Au NR islands tended to connect with each other. The non-standing Au NRs could still be observed on the silicon surface. The assembling efficiency is not significantly improved compared to the two-step incubation. The extending incubation method is easy to operate because the water is not removed during the incubation. However, longer incubation time is needed compared to the two-step method.
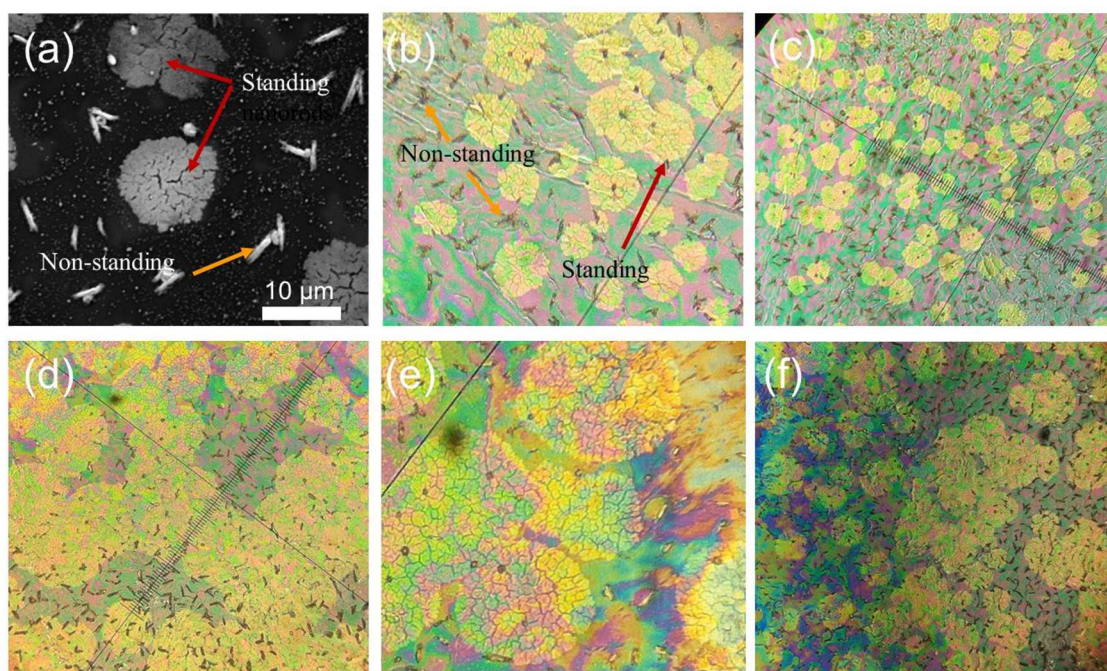
Figure 27 Characterization of vertically aligned Au NRs (aspect ratio of 3.4) assembled on the silicon surface: (a), (b), and (c) were assembled by the proposed two step method (first step: 24 h, second step: 36-48 h); (d), (e), and (f) were assembled by extending the incubation time to ~144 h in one step.

5.4 Summary

In this study, a two-step method was proposed to create standing Au NR arrays. In the first step, the NR droplets were incubated in a closed environment with high humidity for 24 h. In the second step, the contracted droplets were allowed to dry for another 36 - 48 h. The first step concentrates the CTAB in the NR droplets and produces a contracted area for the NR assembling. The second step continues to increase the concentration of CTAB and provides enough time for Au NRs to assemble in a side-by-side manner when CTAB reaches a critical concentration. The standing Au NR arrays were successfully acquired by the two-step method using Au NRs with aspect ratio of 2.0 as building blocks. Results show that nearly all the NRs were vertically aligned on the silicon substrate except that a very small amount of the NRs were confined at the pinned edge with a width of 1.0 μm, thus avoiding wasting NRs due to the formation of pinned

edge. Standing Au NR arrays were also created using Au NRs with aspect ratio of 3.4. Although the yield of standing arrays is much lower compared to the NR with aspect ratio of 2.0, this method is straightforward, cost-effective, and easy to operate. More importantly, there is no need to modify Au NRs by thiolated ligands, synthesize strictly monodispersed Au NRs, or use highly concentrated Au NR solution for the assembling. Further study will focus on improving the yield of standing arrays for Au NRs with higher aspect ratio.

CHAPTER 6

Application of Standing Au NR Arrays as Reproducible SERS Substrates to Measure Pesticides in Apple Juice and Vegetables

6.1 Introduction

The use of pesticides on vegetables can increase the yield and improve the quality of vegetables (Cooper and Dobson 2007). However, pesticide residues on produces could pose potential health risks for the consumers. Current analytical methods for measuring pesticides on vegetable samples include HPLC, GC, and other methods. However, these methods are time-consuming, labor-intensive, and often require sample pretreatment. With rapid developments and advances of nanotechnology and nanomaterials in recent years, there is a growing interest in the application of novel nanomaterials for detection of food contaminants such as pesticides. Particularly, SERS has received much attention in recent year.

SERS is a technique that enhances Raman scattering from molecules absorbed on roughened metal surface, especially on gold and silver nanostructures (Fleischmann and others 1974; Albrecht and Creighton 1977; Campion and Kambhampati 1998). The enhancement factor can be as high as 10^6 to 10^{10} (Le Ru and others 2006; Le Ru and others 2007; Fang and others 2008). Due to high sensitivity, unique spectroscopic fingerprints, and non-destructive data acquisition, SERS technique is becoming one of the most widely used spectroscopic tools for detection and identification of chemical and biological species (Alexander and Le 2007; Liu and others 2010; Liu and others 2012a).

SERS has also been used to detect food contaminants using various SERS-active substrates (Lin and others 2008; He and others 2011; Liu and others 2013).

A variety of methods have been used to fabricate sensitive and high quality SERS substrates, including nanolithography, microsphere lithography, and self-assembling (Wang and others 2006; Alvarez-Puebla and others 2007; Abu Hatab and others 2008; Fang and others 2013). The self-assembling approach is much more cost-effective and easier to operate than lithographic methods. Gold nanostructures, such as nanospheres, nanocubes, and NRs, are widely used to fabricate SERS substrates by evaporation-induced self-assembling method (Lee and others 2010; Wu and others 2011; Thai and others 2012; Wei and Ge 2013b). Among different nanostructures, Au NRs have received much attention due to their anisotropic structures, which can induce intense electromagnetic field (Alvarez-Puebla and others 2011; Thai and others 2012; Peng and others 2013; Wei and Ge 2013b). When a certain amount of cetyltrimethylammonium bromide (CTAB) is kept on the surface of Au NR, it is possible to form a monolayer of vertically aligned Au NR arrays on the silicon (Guerrero‐Martínez and others 2009; Xie and others 2013). This well-ordered NR arrays provide intense electromagnetic field and uniform hot spots for SERS (Alvarez-Puebla and others 2011). Therefore, the standing Au NR arrays have a great potential to be used as an ideal SERS substrate for various applications.

In a previous study, we demonstrated that Au NRs could be vertically aligned on silicon substrates by a two-step method or a one-step method without modifying the Au NR surface and using strictly monodispersed Au NRs (Zhang and Lin 2014). Due to the contraction of NR droplets, a thin crystal layer of CTAB was formed on the top of the standing NR arrays. To use Au NR as a SERS

substrate, it is necessary to remove this thick layer of CTAB, and at the same time, not to damage the morphology of the standing arrays, which is a challenging task.

The objective of this study was to develop SERS method coupled with standing Au NR arrays for detection of pesticides in apple juice and vegetables. We aimed to assemble Au NRs on gold-coated silicon slides. There were two-fold benefits using Au-coated silicon slides as a support for NR arrays. First, the coupling between the gold layer and the Au NRs can generate stronger electromagnetic field than the coupling between Au NRs and silicon. Second, due to the wettability of Au film, the Au NR droplets will not shrink after evaporation, thus forming a thin layer of CTAB layer on the top. This layer of CTAB could be easily removed by ethanol. A sample can be directly placed on the standing arrays for SERS detection after removing the CTAB layer. The analytes solution will uniformly distribute on the substrates to generate reproducible Raman signals.

6.2 Materials & Methods

6.2.1 Materials and chemicals

Hydrogen tetrachloroaurate solution (HAuCl$_4$, 30$wt.$% in dilute HCl), silver nitrate, ascorbic acid, and CTAB, carbaryl were purchased from Sigma-Aldrich (St Louis, MO) and used without any purification. Silicon slides were purchased from Ted Pella (Redding, CA). Organic apple juice and cabbage were purchased from a local grocery store.

6.2.2 Synthesis of Au NRs

Au NRs were synthesized in CTAB solution using a seed-mediated method (Ming and others 2009). Briefly, 1.9 mL of CTAB (0.2 M) and 0.10 mL of $HAuCl_4$ (5 mM) were added into a glass vial. The seeds were generated by injecting 0.12 mL of freshly prepared ice-cold $NaBH_4$ (10 mM) into the glass vial that was subjected to intense shaking. The seed solution was ready to use after 30 min of aging at room temperature. The growth solution was prepared by mixing 40 mL of CTAB solution (0.2 M) with 44 mL of 0.5 mM $HAuCl_4$ in a 150 mL flask. After that, 800 µL of 10 mM $AgNO_3$, 1.1 mL of fresh ascorbic acid (0.1 M), and 1.6 mL of HCl (1.0 M) were added into the mixture. The yellow color of growth solution disappeared after being shaken for about 30 s. Finally, 10 µL of seed solution was injected into the growth solution with gentle stirring. The solution was incubated in water bath (28.0^{o}C) overnight for the growth of Au NRs. The Au NRs were purified by centrifugation at 6000 rpm for 7 mins and redispersion in 20 mL of distilled water. This NR solution was stored at room temperature as a stock solution.

6.2.3 Preparation of the SERS substrates using Au NRs

An aliquot of the stock solution (1.0 mL) was centrifuged again and redispersed in 0.1 mL of CTAB solution (2.5 mM). The as-prepared solution was then subjected to 60 s of sonication for complete dispersion of the NRs. Five drops of NR solution (10 µL) were casted on the Au-coated silicon slides (1 cm × 5 cm). The Au-coated silicon slide was transferred onto a glass slide in a polystyrene petri dish (W: 94 mm, H: 15 mm, VWR, PA, USA). An aliquot of water (50 µL) was then added into the petri dish that was then sealed by parafilm (PM-992, American National Can Co., WI, USA) and placed in an incubator. After 5

days, the NR droplets were completely dried and the standing Au NR arrays were formed on the gold-coated silicon slides. The slides were then immerged into pure ethanol for 5 min to remove the CTAB layer on the top of the NR arrays. After air-dried at room temperature, the slides with standing Au NR arrays were ready to be used as SERS substrates.

6.2.4 Detection of carbaryl in apple juice

The apple juice samples were spiked with different concentrations of carbaryl (0 to 30 ppm) and centrifuged at 10000 rpm for 10 min. The supernatants (10 μL) were directly placed on the as-prepared SERS substrates and dried at room temperature. A micro-Raman spectrometer (Renishaw 1000) equipped a 785 nm laser and 50 × objectives was used to collect the SERS data. The laser beam (30 mW) was focused on the standing Au NR arrays. Raman signals were collected on ten randomly selected spots for each concentration.

As comparison, the carbaryl in apple juice were also extracted and measured by SERS. Briefly, after the centrifugation, the supernatant of spiked apple juice (200 μL) was mixed with same amount of dichloromethane. The mixture was shaken vigorously for 5 min. Then, 150 μL of the dichloromethane layer was transferred to another tube and dried in a fume hood. The carbaryl was re-dissolved in 50 μL of acetonitrile-water solution (50:50). The extracts (10 μL) were placed on the substrates and detected by SERS as described above.

6.2.5 Detection of carbaryl in cabbages

The cabbage sample was cut into small pieces and spiked with a series of concentrations of carbaryl. Carbaryl was extracted from the cabbage by organic

77

solvent. Briefly, the spiked cabbages (0.4 g) were mixed with 50% of acetonitrile-water solution (0.5 mL). The mixture was then vigorously shaken for 10 min and subjected to 10000 rpm of centrifugation for 10 min. A drop of supernatant (10 µL) was placed on the SERS substrates and dried at room temperature for analysis.

6.2.6 Data analysis

All the Raman spectra were processed by Delight software (v3.2.1, D-Squared Development Inc., LaGrande, OR, USA). Firstly, the Raman spectra were subjected to 5 cm^{-1} of smoothing and secondary polynomial subtraction to reduce the noise and baseline drift. Secondly, the multiple linear regression (MLR) model was built to predict the concentrations of carbaryl in tested samples, where 8 latent variables were used. The MLR model was validated and calibrated by leave-one-out cross validation. The detection limit of various samples was determined by the two-sample t-test at a 99% confidence level.

6.3 Results & Discussions

6.3.1 Preparation of standing Au NR arrays as SERS substrates

As shown in Figure 28, the droplets of CTAB-protected Au NR solution were placed on gold-coated silicon slide and incubated in a high humidity environment that provided a very slow evaporation speed for water in the NR solution, thus giving enough time for the Au NRs to assemble in a side-by-side manner. The side-by-side assembled Au NRs finally deposited on the Au film and formed vertically aligned Au NR arrays. After removing the CTAB layer by

ethanol, the pesticide solution was directly placed on the substrate surface and tested by Raman spectrometer.
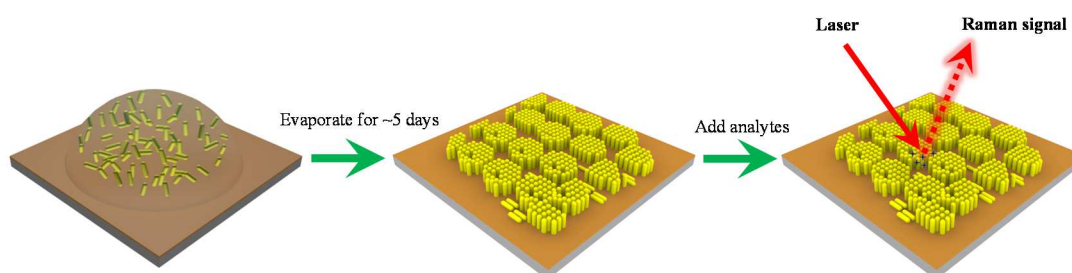
Figure 28 Preparation of standing Au NR arrays on a gold slide as SERS substrate.

The Au NRs used in this study have a length of 80 nm and width of 26 nm. The growth of Au NRs was triggered by adding only 10 μL of seeds solution into the growth solution. Figure 29 shows the optical and SEM images of standing NR arrays on a gold-coated silicon slide. It can be observed that the standing Au NR arrays show golden color and island shape under the optical microscope (Figure 29a). The NR islands are not completely separated with each other. The area between the NR islands show a lower reflected light density, suggesting sparsely scattered Au NRs in this area. The SEM image proved that the junctions between NR islands were filled with low density of Au NRs. The monolayer of standing Au NR arrays was very flat on the gold slides (Figure 29b). There were also a few supercrystals on the slides. The laser beam was directed on the monolayer of Au NRs during the Raman measurement. Therefore, the presence of the supercrystals did not influence the reproducibility of the substrates. It is clearly shown that the Au NRs were vertically aligned on the gold slides (Figure 29c and 29d). The Au NRs were closely packed on the slide with their tips facing up. The close packing is beneficial for the coupling between NRs and generating intense electromagnetic field. In addition, the NR tips are also known to produce high

density of electromagnetic field. Thus, the standing Au NR arrays could be used as a high performance SERS substrate to detect the analytes.
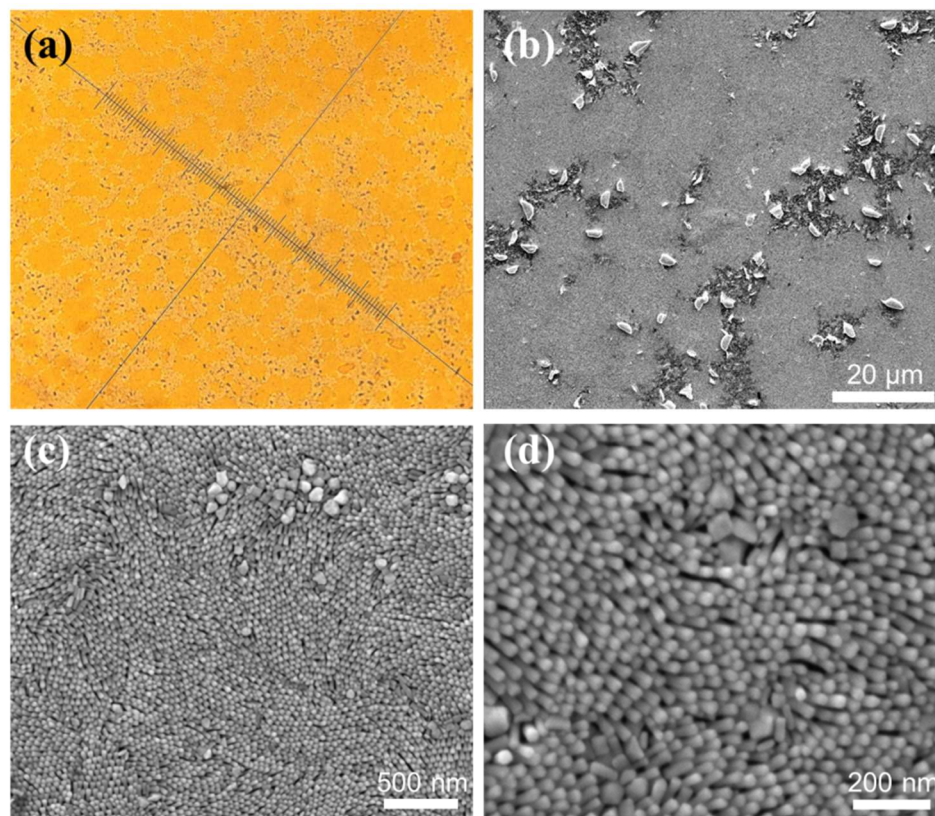
Figure 29 Characterization of standing Au NR arrays on gold slides: (a) optical microscope image; (b), (c), and (d) SEM images at different magnifications.

6.3.2 Detection of carbaryl in acetonitrile solution by SERS

Figure 30a shows the averaged Raman spectra (n = 10) of different concentrations of carbaryl in acetonitrile-water solution. The characteristic peaks of carbaryl, such as the peaks at, 1016, 1382, 1442, and 1578 cm^{-1} can be clearly observed in the Raman spectra. The peaks at 1382, 1442, and 1578 cm^{-1} are due to the symmetric ring vibration, unspecific ring vibration of mono-substituted naphthalene, and stretching of C=C in the naphthalene ring, respectively (Liu and others 2013). We can also observe a big peak at 1447 cm^{-1} even when the concentration of carbaryl is 0 ppm. This interfering band is from

residual CTAB on the nanorod surface that was not able to be removed by ethanol (Gökce and Bahçeli 2013). CTAB was attached on the surface of Au NRs and located between the NR junctions, yielding a Raman band at 1447 cm^{-1}. However, the residual CTAB does not cause interference for other characteristic peaks of carbaryl.

It is clearly shown that the intensity of a peak at 1382 cm^{-1} increased as the concentration of carbaryl increased from 0 to 30 ppm. Second derivative transformation could be used to separate the overlapping peaks, eliminate the baseline drifting, and enhance the spectra resolution. After the second derivative transformation, we can easily differentiate the carbaryl spectra with concentration of 0 and 0.1 ppm. The result shows that vertically aligned Au NRs on gold slides could be used as a sensitive SERS substrate to detect pesticides. When the sample was casted on the substrate, the solution formed a homogeneous layer on the substrate rather than concentrated in a coffee-ring area. This type of partitioning was caused by the interaction of solvent with the specific structure of the substrate. The sensitivity of the homogenous layer approach may be not as good as the coffee-ring type of partitioning. However, the Raman signals are more reproducible due to the homogenous partitioning. In addition, MLR model was employed to analyze the Raman spectra of carbaryl because MLR model yielded a higher coefficient of correlation and lower standard error than the partial linear squares regression. In addition, MLR model was employed to analyze the Raman spectra of carbaryl. It was found that the as-prepared SERS substrates could be used for the quantification of carbaryl solution. As shown in Figure 30b, the R-value and the slope is 0.97 and 0.95, respectively. These results show a good linear correlation between the actual

concentrations and the predicted concentrations of carbaryl. The good linear relationship could be ascribed to the uniform distribution of the SERS "hot-spots" through the standing arrays. If the hot-spots were not uniformly distributed on the substrates, the blind selection of testing spots would result in large variations for the Raman spectra and thus make it difficult to quantify the analytes.
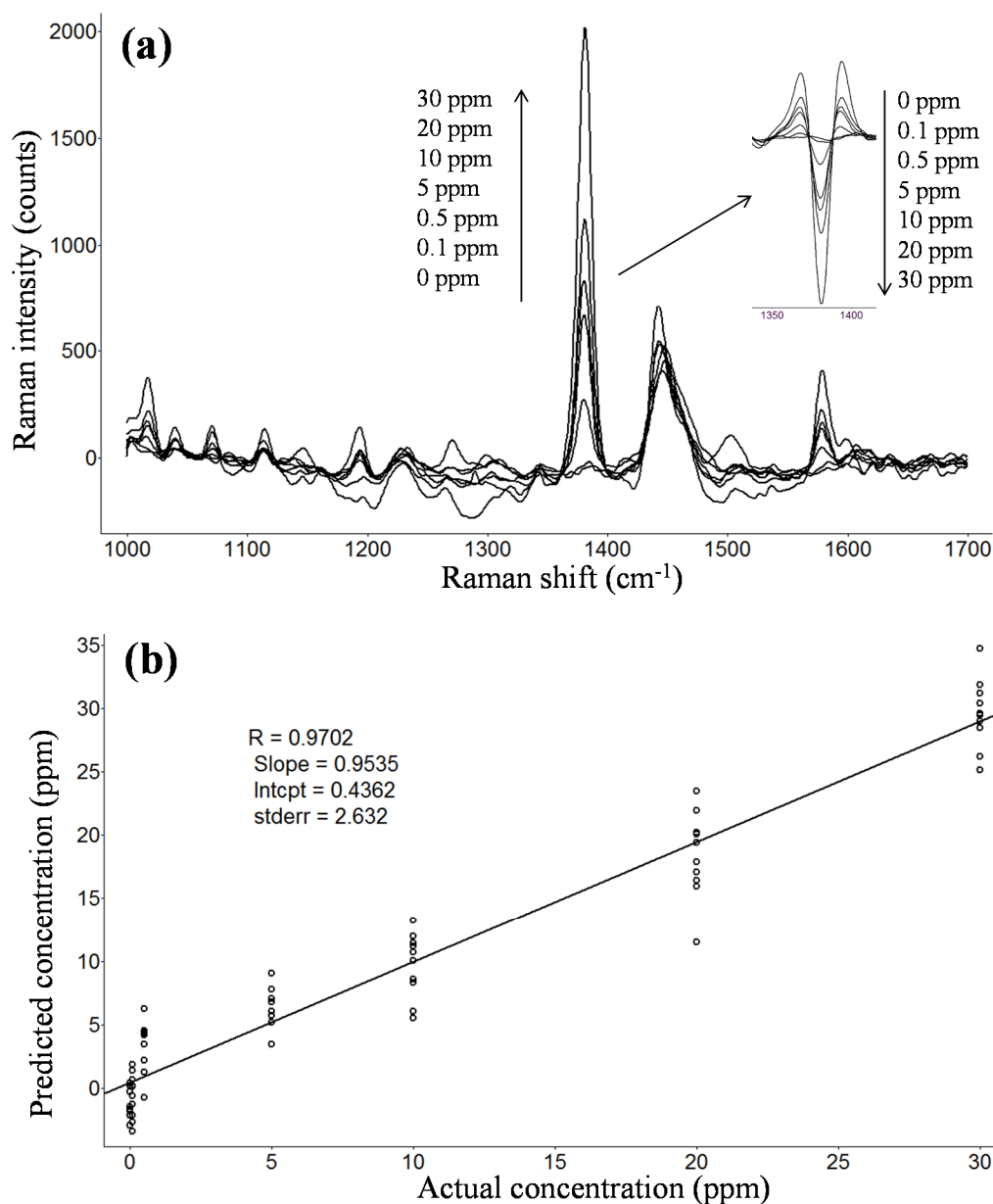
Figure 30 Detection of carbaryl using as-prepared substrates: (a) averaged Raman spectra of carbaryl with concentration from 0 to 30 ppm; inset: second derivatives of Raman spectra at 1382 cm^{-1}; (b) predicted concentration vs. actual concentration of carbaryl using MLR model (n=70).

6.3.3 Detection of carbaryl in apple juice by SERS

Carbaryl in apple juice needs to be extracted by organic solvents before the determination by HPLC. In contrast, the supernatant of spiked apple juice was directly used in the SERS detection. There was a large amount of sugar in apple juice. The sugar formed a transparent layer on the substrate after the droplet was dried. However, this transparent layer did not cause any trouble for the spectra collection. As shown in Figure 31a, the most important characteristic peaks of carbaryl could be observed in the Raman spectra. The intensity of Raman bands at 1382 cm^{-1} and 1578 cm^{-1} increased with the increased concentrations of carbaryl in apple juice (0 - 30 ppm). This figure also demonstrates that SERS can detect as low as 1.0 ppm of carbaryl in apple juice. Sugar and other carbohydrates in apple juice did not yield any significant interfering peaks. The MLR analysis of the Raman spectra in apple juice shows that there is a good linear correlation between the actual concentration of carbaryl and predicted concentration of carbaryl in apple juice (R = 0.97, Slope = 0.91). These results indicate that carbaryl in apple juice can be quantified by SERS coupled with the standing NR arrays on gold slides even without the extraction step.
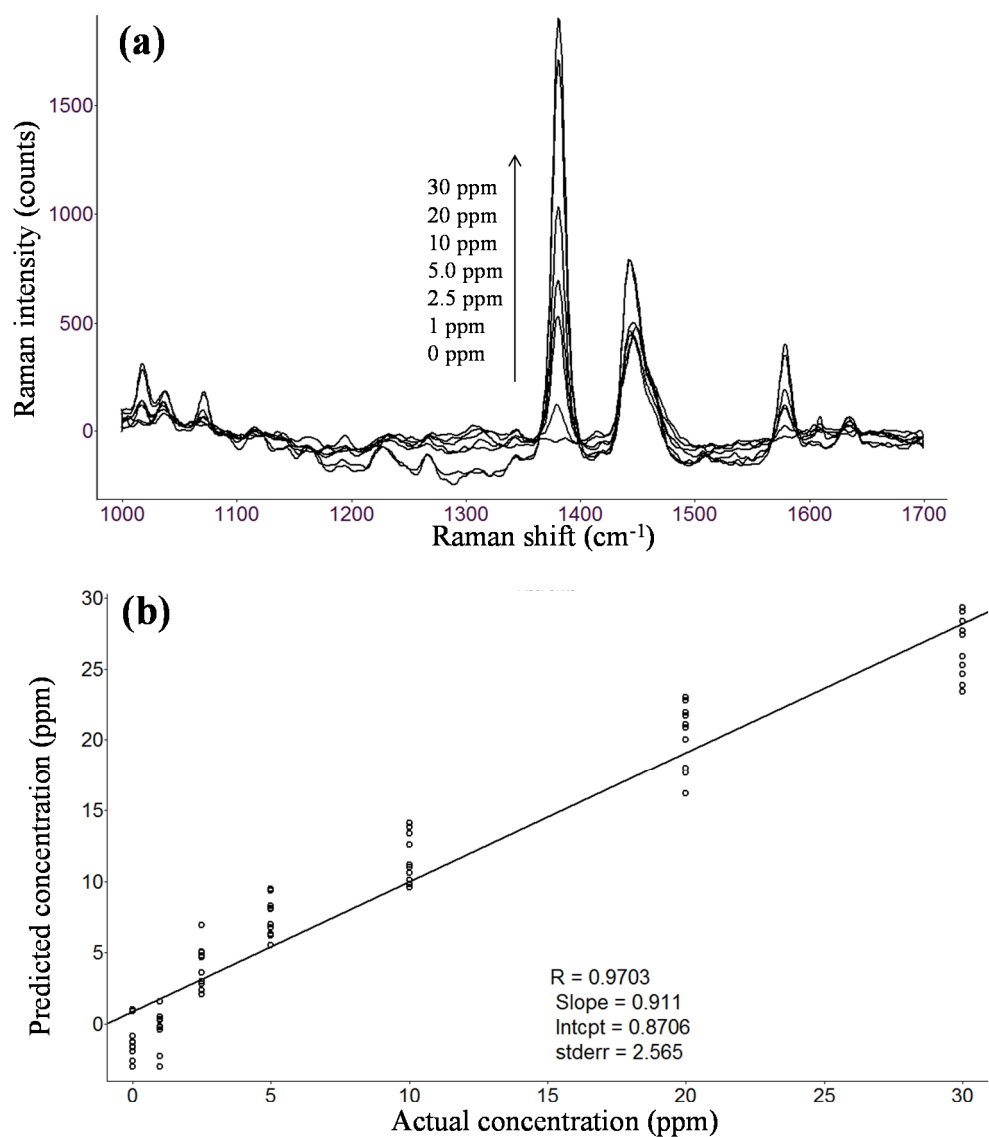
Figure 31 Detection of carbaryl in apple juice using as-prepared substrates and non-extraction method: (a) averaged Raman spectra of apple juice with carbaryl concentration from 0-30 ppm; (b) predicted concentration vs. actual concentration of carbaryl in apple juice using MLR model (n=70).
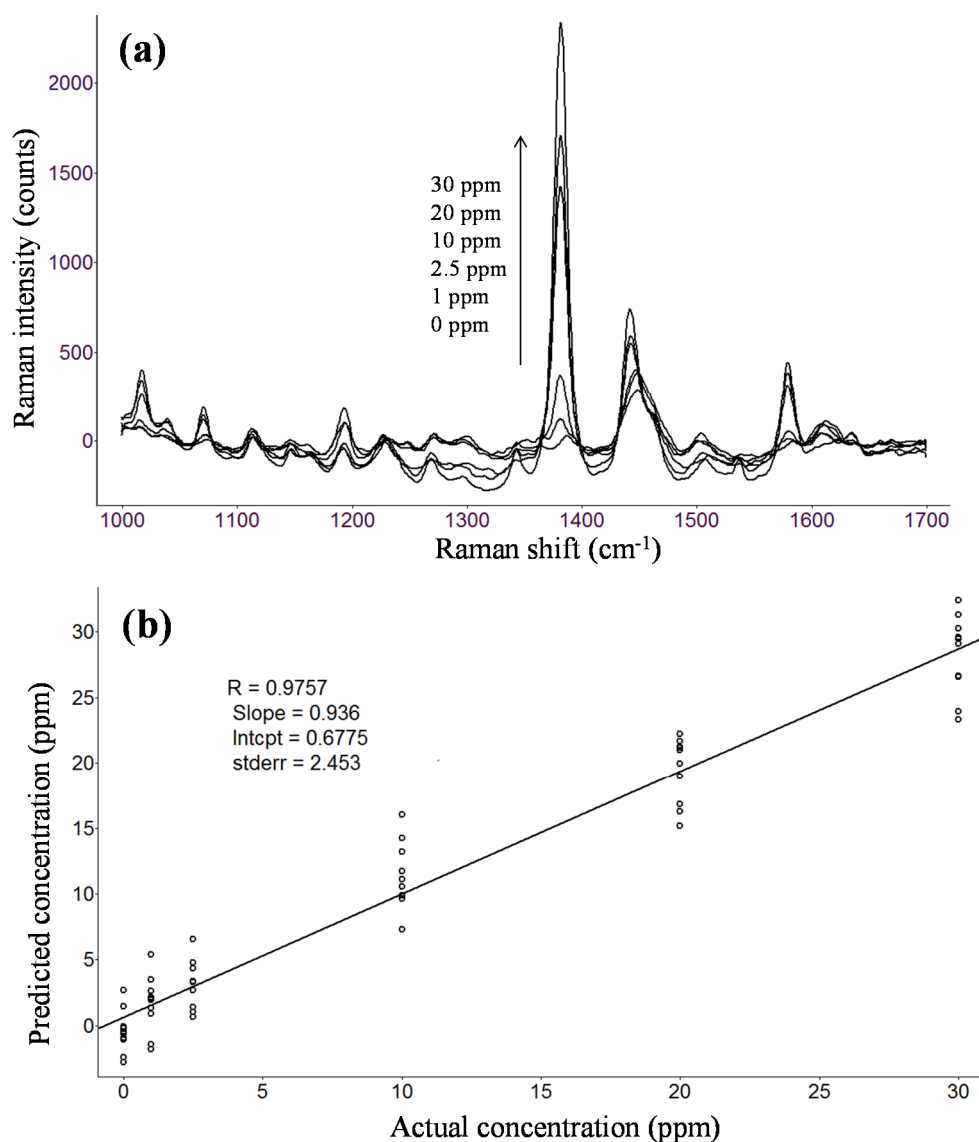
Figure 32 Detection of carbaryl in apple juice using as-prepared substrates and extraction method: (a) averaged Raman spectra of apple juice with carbaryl concentration from 0-30 ppm; (b) predicted concentration vs. actual concentration of carbaryl in apple juice using MLR model (n=60).

As a comparison, carbaryl was spiked in apple juice and then extracted by dichloromethane and re-dissolved in acetonitrile-water solution. The solutions were then analyzed by SERS using the same substrates. A few standing arrays were damaged after droplets were dried, but the majority of standing arrays remained intact. The laser spot was focused on the intact standing arrays. The carbaryl peaks are clearly shown in the Raman spectra (Figure 32a). Higher concentration of carbaryl always generates higher Raman intensity at 1382 cm^{-1}.

The MLR model can accurately predict the actual concentrations of carbaryl extracted from apple juice (R = 0.97, Slope = 0.94). Therefore, SERS coupled with standing NR arrays can be used to quantify carbaryl in apple juice directly or from the apple juice extract. However, in this case, it is not necessary to extract the pesticides from apple juice by organic solvents. This is an important advantage of SERS method compared to the HPLC or GC methods, which may require SPE extraction or derivatization (Valenzuela and others 1999; Koal and others 2003; Fillion and others 2000). The extraction and derivatization take a much longer time and could potentially bring addition errors. In addition, SERS method does not cause any damage to the instrument due to unwanted precipitates from apple juice or the juice extract. However, there is a limitation of SERS method. When extracting pesticides from food matrices, some food components will also be extracted to the solvent. These food components will compete for the "hot-spots" on the SERS substrates and cause interference in the analysis.

6.3.4 Detection of carbaryl in cabbage by SERS
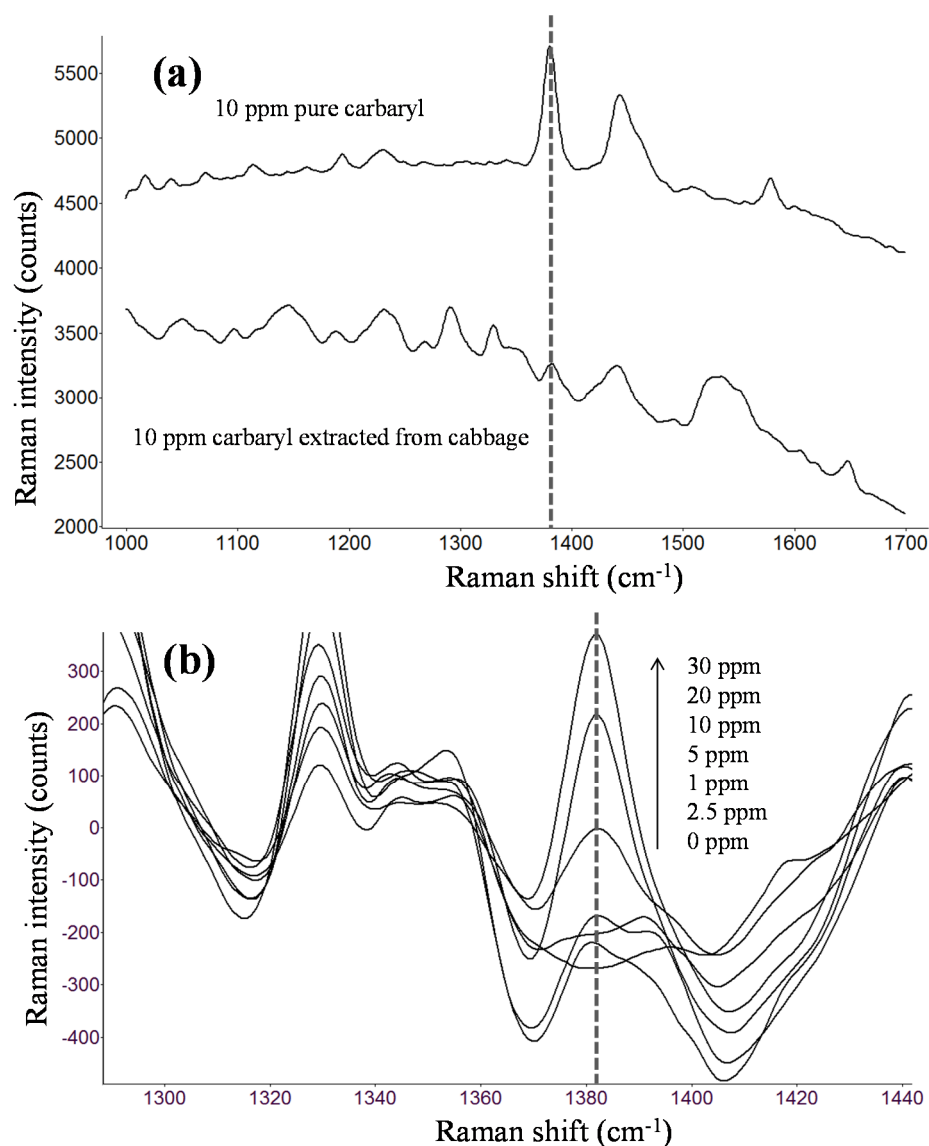
Figure 33 (a) Raman spectra of pure carbaryl (10 ppm) and carbaryl from cabbage (10 ppm); (b) averaged Raman spectra of carbaryl in cabbage with concentration from 0-30 ppm.

Unlike apple juice, it is necessary to extract carbaryl from cabbage by organic solvents for the SERS detection. Herein, acetonitrile-water (50:50) solution was used to extract carbaryl from cabbage. Figure 33a shows the Raman spectra of 10 ppm of pure carbaryl and 10 ppm of carbaryl extracted from cabbage. The pure carbaryl (10 ppm) solution yielded much higher Raman intensity at 1382 cm^{-1} than the same concentration of carbaryl extracted from the

cabbage, which may be explained by competitive effects of SERS. The interfering compounds were also extracted into the acetonitrile-water solution and placed on the substrates. They competed for the SERS "hot-spots" on the substrates and reduced the available "hot-spots" for carbaryl, thus suppressing the Raman intensity of carbaryl. A few interfering peaks, such as the peaks at 1289 and 1145 cm^{-1}, are shown in the Raman spectrum of the cabbage extract. Nonetheless, carbaryl can still be identified using the band at 1382 cm^{-1} even when a few interfering bands are present in the spectra. As shown in Figure 33b, the Raman intensity of carbaryl at 1382 cm^{-1} increased as the concentration increased from 0 to 30 ppm. The second derivative transformation of the Raman spectra also clearly shows the same trend (Figure 34a). The spectra at the concentrations of 0 and 1 ppm were fully separated after the second derivative transformation. The MLR analysis indicates that the predicted concentrations of carbaryl are linearly correlated with the actual concentrations of carbaryl in cabbage. The results suggest that SERS coupled with the standing NR arrays could accurately detect carbaryl in cabbage by extracting carbaryl using the acetonitrile-water solution.
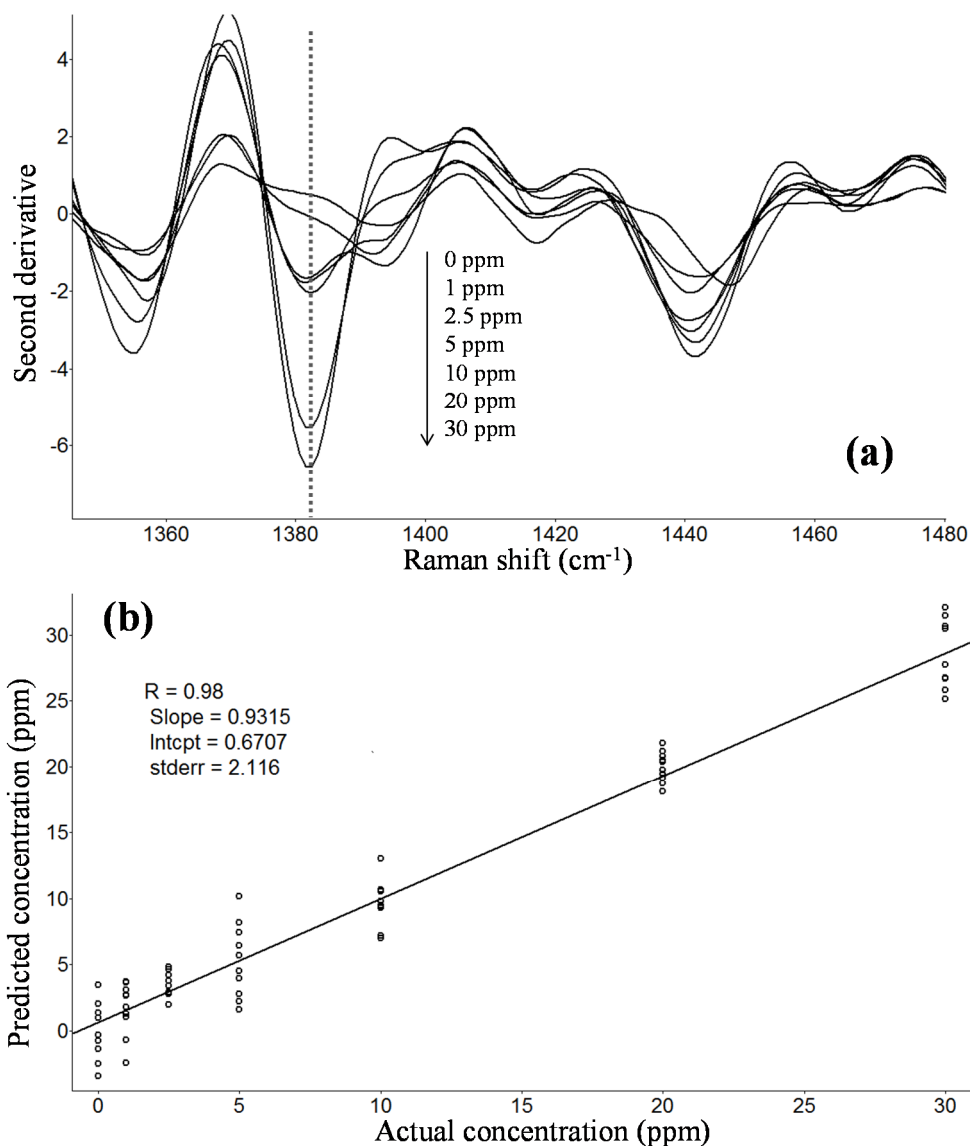
Figure 34 Detection of carbaryl in cabbage: (a) second derivatives of Raman spectra of carbaryl with concentration from 0-30 ppm; (b) predicted concentration vs. actual concentration of carbaryl in cabbage using MLR model (n=70).

## 6.3.5 Detection limits and recoveries of carbaryl in different samples

Table 2 summarizes the detection limits and the recoveries of carbaryl in different samples. The detection limit is 0.5 ppm for pure carbaryl solution. The detection limit is 2.5 ppm when carbaryl was directly measured in apple juice or after being extracted from apple juice. The detection limit of carbaryl in cabbage is 2.5 ppm by the proposed SERS method. According to the regulations of U.S.

EPA, the maximum residue limits (MRL) of carbaryl in apple pomace and cabbage is 15 and 21 ppm, respectively (EPA 2014). The proposed SERS methods meet the EPA's requirement of carbaryl in apple juice and cabbage. In addition, satisfactory recoveries have been acquired by the proposed SERS method for all the samples. For example, the recovery percentage of 10 ppm of carbaryl in apple juice and cabbage are 116.1% and 97.0%.

Table 2 Limit of detection (LOD) and recovery of carbaryl in different samples

Samples	LOD (ppm)	Recovery (10 ppm)	Recovery (20 ppm)
Pure carbaryl	0.5	9.73 ± 2.48	18.11 ± 3.77
Apple juice (extract)	2.5	11.47 ± 2.49	19.43 ± 2.52
Apple juice	2.5	11.61 ± 1.7	20.31 ± 2.32
Cabbage	2.5	9.70 ± 1.73	19.99 ± 1.17

6.4 Summary

In this study, cost-effective, sensitive, and reproducible SERS substrates were successfully fabricated by assembling standing Au NR arrays on the gold-coated silicon slides. The standing NR arrays provide strong electromagnetic field and numerous SERS "hot-spots", which are uniformly distributed on the array surface. The proposed SERS substrates were used to detect carbaryl in apple juice and cabbage. Results show that SERS can accurately quantify carbaryl in apple juice and cabbage using the as-prepared substrates. At the same time, satisfactory detection limits and recoveries were obtained by this method. More importantly, the substrates can be easily synthesized using the one-step assembling method. The substrates may be used to measure other types of contaminants in a variety

of food commodities by SERS. Future study will be focused on reducing the gap

distance between NRs and removing the interference from CTAB.

CHAPTER 7

Conclusions and Future Directions

In this study, contamination of engineered Ag NPs in pears were characterized and determined by TEM and SEM-EDS. The concentration of Ag NPs in food samples was measured by ICP-OES, which can detect as low as 22.7 ppb of Ag NPs in pears. This study provides a promising approach for detection, characterization, and quantification of contamination of Ag NPs in food crops or other agricultural products.

Secondly, Au NPs were successfully incorporated in the DLS technique for the detection of food contaminations. DLS coupled with superparamagnetic beads and Au nanoprobes could be used to measure the concentration of AFM by direct competition between AFM and nanoprobes. The method could detect AFM in spiked milk samples (0 - 400 ppb) with a LOD of 27.5 ppb. This method could be easily adapted for the detection of other types of food contaminants.

In addition, this study also proposed two simple and reproducible methods to fabricate standing Au NR arrays. The standing Au NR arrays were successfully acquired by a two-step method using Au NRs with aspect ratio of 2.0 and 3.4 as building blocks. The yields for standing NRs were 95% for Au NRs with aspect ratio of 2.0 and 60% for Au NRs with aspect ratio of 3.4. Au NRs can also be assembled into standing arrays using a one-step method with extended incubation time. Both methods do not need to modify Au NRs by thiolated ligands, synthesize strictly monodispersed Au NRs, or use highly concentrated Au NR solution for the assembling.

Furthermore, Au NRs were assembled into standing arrays on gold-coated silicon slides using the above mentioned one-step method. The standing NR arrays were closely packed on the gold film, generating strong electromagnetic field and uniformly distributed SERS "hot-spots" on the array surface. Strong and reproducible Raman signals were generated for the pesticides extracted from food samples using the standing NR arrays as substrates. The method could quantify the pesticides (R > 0.97) with a LOD of 2.5 ppm, meeting the maximum residue limits built by EPA. SERS coupled with the substrates is a sensitive and reproducible method and can be used for rapid detection of other chemical contaminations in foods.

However, there are still a few problems need to be addressed in the future. First, the method of using a combination of technologies for the detection of engineered NPs is time-consuming and expensive. Cost-effective technologies are needed for rapid characterization of engineered NPs. Second, more uniformly distributed Au NPs are needed to reduce the standard deviation for DLS applications. Aptamer may also be used to replace antibody to reduce the total cost. At the same time, the proposed DLS method is not feasible for the analysis of aflatoxins in solid foods. The toxins need to be extracted by organic solvent from solid foods. Future research direction should focus on the synthesis of novel NPs which have great compatibility with the organic solvent. Finally, the standing Au NR arrays are promising and reproducible SERS substrates for measurement of food contamination. The performance may be further improved by reducing the gap distance between Au NRs and increasing the size of Au NRs. Future research may focus on removing the CTAB between Au NRs by UV-ozone and oxygen plasma for smaller gap distance.

APPENDIX

1. Abbreviations

Au: Gold

Ag: Silver

NP: Nanoparticle

NR: Nanorod

LSPR: Localized surface plasmon resonance

SERS: Surface enhanced Raman spectroscopy

DLS: Dynamic light scattering

LOD: Limit of Detection

AFM: Aflatoxin M1

2. Unit conversions

ppm: part per million (mg/kg)

ppb: part per billion (µg/kg)

REFERENCES

Abu Hatab NA, Oran JM, Sepaniak MJ. 2008. Surface-enhanced Raman spectroscopy substrates created via electron beam lithography and nanotransfer printing. ACS Nano 2(2):377-385.

Albrecht MG, Creighton JA. 1977. Anomalously intense Raman spectra of pyridine at a silver electrode. J Am Chem Soc 99(15):5215-5217.

Alexander TA, Le DM. 2007. Characterization of a commercialized SERS-active substrate and its application to the identification of intact Bacillus endospores. Appl Opt 46(18):3878-3890.

Alvarez-Puebla R, Cui B, Bravo-Vasquez J-P, Veres T, Fenniri H. 2007. Nanoimprinted SERS-active substrates with tunable surface plasmon resonances. J Phys Chem C 111(18):6720-6723.

Alvarez-Puebla RA, Agarwal A, Manna P, Khanal BP, Aldeanueva-Potel P, Carbó-Argibay E, Pazos-Pérez N, Vigderman L, Zubarev ER, Kotov NA. 2011. Gold nanorods 3D-supercrystals as surface enhanced Raman scattering spectroscopy substrates for the rapid detection of scrambled prions. Proc Natl Acad Sci USA 108(20):8157-8161.

Azeredo H. 2009. Nanocomposites for food packaging applications. Food Res Int 42(9):1240-1253.

Banitaba MH, Davarani SS, Mehdinia A. 2011. Study of interactions between DNA and aflatoxin B1 using electrochemical and fluorescence methods. Anal Biochem 411(2):218-222.

Benn T, Cavanagh B, Hristovski K, Posner JD, Westerhoff P. 2010. The release of nanosilver from consumer products used in the home. Journal of environmental quality 39(6):1875-1882.

Bergeson LL. 2010. Nanosilver: US EPA's pesticide office considers how best to proceed. Environmental Quality Management 19(3):79-85.

Bjorck L, Kronvall G. 1984. Purification and some properties of streptococcal protein G, a novel IgG-binding reagent. J Immunol 133(2):969-974.

Bognanno M, La Fauci L, Ritieni A, Tafuri A, De Lorenzo A, Micari P, Di Renzo L, Ciappellano S, Sarullo V, Galvano F. 2006. Survey of the occurrence of Aflatoxin M1 in ovine milk by HPLC and its confirmation by MS. Mol Nutr Food Res 50(3):300-305.

Bouwmeester H, Dekkers S, Noordam MY, Hagens WI, Bulder AS, De Heer C, Ten Voorde SECG, Wijnhoven SWP, Marvin HJP, Sips AJAM. 2009. Review of health safety aspects of nanotechnologies in food production. Regul Toxicol Pharmacol 53(1):52-62.

Brewer SH, Glomm WR, Johnson MC, Magne K, Franzen S. 2005. Probing BSA binding to citrate-coated gold nanoparticles and surfaces. Langmuir 21(20):9303-9307.

Campion A, Kambhampati P. 1998. Surface-enhanced Raman scattering. Chem Soc Rev 27(4):241-250.

Carvalho FP. 2006. Agriculture, pesticides, food security and food safety. Environ Sci Policy 9(7):685-692.

Cecchini MP, Turek VA, Paget J, Kornyshev AA, Edel JB. 2012. Self-assembled nanoparticle arrays for multiphase trace analyte detection. Nature Materials.

Chan GH, Zhao J, Hicks EM, Schatz GC, Van Duyne RP. 2007. Plasmonic properties of copper nanoparticles fabricated by nanosphere lithography. Nano Lett 7(7):1947-1952.

Chen A, DePrince AE, Demortière A, Joshi‐Imre A, Shevchenko EV, Gray SK, Welp U, Vlasko‐Vlasov VK. 2011. Self‐Assembled Large Au Nanoparticle Arrays with Regular Hot Spots for SERS. Small 7(16):2365-2371.

Chen G, Wang Y, Tan LH, Yang M, Tan LS, Chen Y, Chen H. 2009. High-purity separation of gold nanoparticle dimers and trimers. J Am Chem Soc 131(12):4218-4219.

Chu FS. 1991. Mycotoxins: food contamination, mechanism, carcinogenic potential and preventive measures. Mutat Res-GenTox En 259(3-4):291-306.

Colthup NB, Daly LH, Wiberley SE. 1990. Introduction to infrared and Raman spectroscopy. Elsevier.

Cooney RP, Reid ES, Fleischmann M, Hendra PJ. 1977. Thiocyanate adsorption and corrosion at silver electrodes. A Raman spectroscopic study. J Chem Soc, Faraday Trans 1 73(0):1691-1698.

Cooper J, Dobson H. 2007. The benefits of pesticides to mankind and the environment. Crop Protect 26(9):1337-1348.

Dai Q, Liu X, Coutts J, Austin L, Huo Q. 2008. A one-step highly sensitive method for DNA detection using dynamic light scattering. J Am Chem Soc 130(26):8138-8139.

Dai Q, Rettner CT, Davis B, Cheng J, Nelson A. 2011. Topographically directed self-assembly of goldnanoparticles. J Mater Chem 21(42):16863-16865.

Daniel M-C, Astruc D. 2004. Gold nanoparticles: assembly, supramolecular chemistry, quantum-size-related properties, and applications toward biology, catalysis, and nanotechnology. Chemical reviews 104(1):293-346.

de KOk A, Hiemstra M. 1992. Optimization, automation, and validation of the solid-phase extraction cleanup and on-line liquid chromatographic determination of N-methylcarbamate pesticides in fruits and vegetables. Journal of AOAC International 75(6):1063-1072.

De la Rosa G, Peralta-Videa J, Gardea-Torresdey J. 2003. Utilization of ICP/OES for the determination of trace metal binding to different humic fractions. J Hazard Mater 97(1):207-218.

De Moura MR, Mattoso LH, Zucolotto V. 2012. Development of cellulose-based bactericidal nanocomposites containing silver nanoparticles and their use as active food packaging. J Food Eng 109(3):520-524.

Delie F. 1998. Evaluation of nano- and microparticle uptake by the gastrointestinal tract. Adv Drug Del Rev 34(2–3):221-233.

Drummond TG, Hill MG, Barton JK. 2003. Electrochemical DNA sensors. Nat Biotech 21(10):1192-1199.

Duncan TV. 2011. Applications of nanotechnology in food packaging and food safety: barrier materials, antimicrobials and sensors. Journal of colloid and interface science 363(1):1-24.

Dunlap RE, Beus CE. 1992. Understanding public concerns about pesticides: An empirical examination. Journal of Consumer Affairs 26(2):418-438.

Durr NJ, Larson T, Smith DK, Korgel BA, Sokolov K, Ben-Yakar A. 2007. Two-photon luminescence imaging of cancer cells using molecularly targeted gold nanorods. Nano Lett 7(4):941-945.

Eaton DL, Gallagher EP. 1994. Mechanisms of aflatoxin carcinogenesis. Annu Rev Pharmacol 34(1):135-172.

El-Sayed IH, Huang X, El-Sayed MA. 2005. Surface plasmon resonance scattering and absorption of anti-EGFR antibody conjugated gold nanoparticles in cancer diagnostics: applications in oral cancer. Nano Lett 5(5):829-834.

EPA. 2014. Tolerances and exemptions for pesticide chemical residues in food.

Etchegoin PG, Le Ru EC. 2011. Basic Electromagnetic Theory of SERS. Surface Enhanced Raman Spectroscopy:1-37.

Fang C, Bandaru NM, Ellis AV, Voelcker NH. 2013. Beta-cyclodextrin decorated nanostructured SERS substrates facilitate selective detection of endocrine disruptorchemicals. Biosens Bioelectron 42:632-639.

Fang Y, Seong N-H, Dlott DD. 2008. Measurement of the Distribution of Site Enhancements in Surface-Enhanced Raman Scattering. Science 321(5887):388-392.

FAO. 2012. Global pact against plant pests marks 60 years in action. Food and Agriculture Organization of the United Nations.

Feng X, Mao C, Yang G, Hou W, Zhu JJ. 2006. Polyaniline/Au composite hollow spheres: synthesis, characterization, and application to the detection of dopamine. Langmuir 22(9):4384-4389.

Fernández A, Soriano E, López-Carballo G, Picouet P, Lloret E, Gavara R, Hernández-Muñoz P. 2009. Preservation of aseptic conditions in absorbent pads by using silver nanotechnology. Food Res Int 42(8):1105-1112.

Ferraro JR. 2003. Introductory raman spectroscopy. Academic press.

Fillion J, Sauve F, Selwyn J. 2000. Multiresidue method for the determination of residues of 251 pesticides in fruits and vegetables by gas chromatography/mass spectrometry and liquid chromatography with fluorescence detection. J AOAC Int 83(3):698-713.

Fleischmann M, Hendra P, McQuillan A. 1974. Raman spectra of pyridine adsorbed at a silver electrode. Chem Phys Lett 26(2):163-166.

Franchini MC, Ponti J, Lemor R, Fournelle M, Broggi F, Locatelli E. 2010. Polymeric entrapped thiol-coated gold nanorods: cytotoxicity and suitability as molecular optoacoustic contrast agent. J Mater Chem 20(48):10908-10914.

Frens G. 1973. Controlled nucleation for the regulation of the particle size in monodisperse gold suspensions. Nature 241(105):20-22.

Galvano F, Galofaro V, Galvano G. 1996. Occurrence and stability of aflatoxin M1 in milk and milk products: a worldwide review. J Food Protect 59(10):1079-1090.

Gökce H, Bahçeli S. 2013. The molecular structures, vibrational spectroscopies (FT-IR and Raman) and quantum chemical calculations of n-alkyltrimethylammonium bromides. Opt Spectrosc 115(5):632-644.

Goldburg W. 1999. Dynamic light scattering. American Journal of Physics 67(12):1152-1160.

Gong J, Li G, Tang Z. 2012. Self-assembly of noble metal nanocrystals: Fabrication, optical property, and application. Nano Today.

Gossner CM-E, Schlundt J, Embarek PB, Hird S, Lo-Fo-Wong D, Beltran JJO, Teoh KN, Tritscher A. 2009. The melamine incident: implications for international food and feed safety. Environ Health Perspect:1803-1808.

Grzelczak M, Vermant J, Furst EM, Liz-Marzán LM. 2010. Directed self-assembly of nanoparticles. ACS Nano 4(7):3591-3605.

Guerrero‐Martínez A, Pérez‐Juste J, Carbó‐Argibay E, Tardajos G, Liz‐Marzán LM. 2009. Gemini‐Surfactant‐Directed Self‐Assembly of Monodisperse Gold Nanorods into Standing Superlattices. Angew Chem Int Ed 48(50):9484-9488.

He L, Rodda T, Haynes CL, Deschaines T, Strother T, Diez-Gonzalez F, Labuza TP. 2011. Detection of a foreign protein in milk using surface-enhanced Raman spectroscopy coupled with antibody-modified silver dendrites. Analytical chemistry 83(5):1510-1513.

Hu H, Larson RG. 2006. Marangoni effect reverses coffee-ring depositions. J Phys Chem B 110(14):7090-7094.

Hu M, Chen J, Li Z-Y, Au L, Hartland GV, Li X, Marquez M, Xia Y. 2006. Gold nanostructures: engineering their plasmonic properties for biomedical applications. Chem Soc Rev 35(11):1084-1094.

Huang X, El-Sayed IH, Qian W, El-Sayed MA. 2006. Cancer cell imaging and photothermal therapy in the near-infrared region by using gold nanorods. J Am Chem Soc 128(6):2115-2120.

Huang Y-F, Sefah K, Bamrungsap S, Chang H-T, Tan W. 2008. Selective photothermal therapy for mixed cancer cells using aptamer-conjugated nanorods. Langmuir 24(20):11860-11865.

Hussain I, Anwar J, Asi MR, Munawar MA, Kashif M. 2010. Aflatoxin M1 contamination in milk from five dairy species in Pakistan. Food Control 21(2):122-124.

Iha MH, Barbosa CB, Favaro RMD, Trucksess MW. 2011. Chromatographic Method for the Determination of Aflatoxin M1 in Cheese, Yogurt, and Dairy Beverages. J AOAC Int 94(5):1513-1518.

Ikem A, Nwankwoala A, Odueyungbo S, Nyavor K, Egiebor N. 2002. Levels of 26 elements in infant formula from USA, UK, and Nigeria by microwave digestion and ICP-OES. Food Chem 77(4):439-447.

Im H, Bantz KC, Lee SH, Johnson TW, Haynes CL, Oh SH. 2013. Self‐Assembled Plasmonic Nanoring Cavity Arrays for SERS and LSPR Biosensing. Adv Mater.

Im H, Bantz KC, Lindquist NC, Haynes CL, Oh S-H. 2010. Vertically Oriented Sub-10-nm Plasmonic Nanogap Arrays. Nano Lett 10(6):2231-2236.

Instruments M. 2004. Zetasizer nano series user manual. MAN0317.

Jana NR. 2004. Shape Effect in Nanoparticle Self‑Assembly. Angew Chem Int Ed 43(12):1536-1540.

Jans H, Liu X, Austin L, Maes G, Huo Q. 2009. Dynamic light scattering as a powerful tool for gold nanoparticle bioconjugation and biomolecular binding studies. Anal Chem 81(22):9425-9432.

Kabashin A, Evans P, Pastkovsky S, Hendren W, Wurtz G, Atkinson R, Pollard R, Podolskiy V, Zayats A. 2009. Plasmonic nanorod metamaterials for biosensing. Nat Mater 8(11):867-871.

Kammer F, Legros S, Hofmann T, Larsen EH, Loeschner K. 2011. Separation and characterization of nanoparticles in complex food and environmental samples by field-flow fractionation. TrAC Trends in Analytical Chemistry 30(3):425-436.

Khlebtsov BN, Khlebtsov NG. 2011. On the measurement of gold nanoparticle sizes by the dynamic light scattering method. Colloid J 73(1):118-127.

Kim E, Shon D, Ryu D, Park J, Hwang H, Kim Y. 2000. Occurrence of aflatoxin M1 in Korean dairy products determined by ELISA and HPLC. Food Addit Contam 17(1):59-64.

Kimling J, Maier M, Okenve B, Kotaidis V, Ballot H, Plech A. 2006. Turkevich method for gold nanoparticle synthesis revisited. J Phys Chem B 110(32):15700-15707.

Ko H, Singamaneni S, Tsukruk VV. 2008. Nanostructured surfaces and assemblies as SERS media. Small 4(10):1576-1599.

Koal T, Asperger A, Efer J, Engewald W. 2003. Simultaneous determination of a wide spectrum of pesticides in water by means of fast on-line SPE-HPLC-MS-MS—a novel approach. Chromatographia 57(1):S93-S101.

Kreyling WG, Semmler-Behnke M, Chaudhry Q. 2010. A complementary definition of nanomaterial. Nano Today 5(3):165-168.

Kullock R, Hendren WR, Hille A, Evans PR, Pollard RJ, Atkinson R, Eng LM. 2008. Polarization conversion through collective surface plasmons in metallic nanorod arrays. Opt Express 16(26):21671-21681.

Le Ru E, Blackie E, Meyer M, Etchegoin P. 2007. Surface enhanced Raman scattering enhancement factors: a comprehensive study. J Phys Chem C 111(37):13794-13803.

Le Ru E, Etchegoin P, Meyer M. 2006. Enhancement factor distribution around a single surface-enhanced Raman scattering hot spot and its relation to single molecule detection. J Chem Phys 125:204701.

Lee K-S, El-Sayed MA. 2006. Gold and silver nanoparticles in sensing and imaging: sensitivity of plasmon response to size, shape, and metal composition. J Phys Chem B 110(39):19220-19225.

Lee SY, Hung L, Lang GS, Cornett JE, Mayergoyz ID, Rabin O. 2010. Dispersion in the SERS Enhancement with Silver Nanocube Dimers. ACS Nano 4(10):5763-5772.

Lehotay SJ, Kok Ad, Hiemstra M, Bodegraven Pv. 2005. Validation of a fast and easy method for the determination of residues from 229 pesticides in fruits and vegetables using gas and liquid chromatography and mass spectrometric detection. Journal of AOAC International 88(2):595-614.

Liao J-Y, Li H. 2010. Lateral flow immunodipstick for visual detection of aflatoxin B1 in food using immuno-nanoparticles composed of a silver core and a gold shell. Microchimica Acta 171(3-4):289-295.

Lin M, He L, Awika J, Yang L, Ledoux D, Li H, Mustapha A. 2008. Detection of melamine in gluten, chicken feed, and processed foods using surface enhanced Raman spectroscopy and HPLC. J Food Sci 73(8):T129-T134.

Lin S, Li M, Dujardin E, Girard C, Mann S. 2005. One‐Dimensional Plasmon Coupling by Facile Self‐Assembly of Gold Nanoparticles into Branched Chain Networks. Adv Mater 17(21):2553-2559.

Liu B, Han G, Zhang Z, Liu R, Jiang C, Wang S, Han MY. 2012a. Shell thickness-dependent Raman enhancement for rapid identification and detection of pesticide residues at fruit peels. Anal Chem 84(1):255-261.

Liu B, Lin M, Li H. 2010. Potential of SERS for rapid detection of melamine and cyanuric acid extracted from milk. Sens Instrum Food Qual Saf 4(1):13-19.

Liu B, Zhou P, Liu X, Sun X, Li H, Lin M. 2012b. Detection of Pesticides in Fruits by Surface-Enhanced Raman Spectroscopy Coupled with Gold Nanostructures. Food and Bioprocess Technology:1-9.

Liu B, Zhou P, Liu X, Sun X, Li H, Lin M. 2013. Detection of pesticides in fruits by surface-enhanced raman spectroscopy coupled with gold nanostructures. Food Bioprocess Tech 6(3):710-718.

Liu C, Wang H, Cui Z, He X, Wang X, Zeng X, Ma H. 2007. Optimization of extraction and isolation for 11S and 7S globulins of soybean seed storage protein. Food Chemistry 102(4):1310-1316.

Liu S, Chen G, Prasad PN, Swihart MT. 2011. Synthesis of monodisperse Au, Ag, and Au–Ag alloy nanoparticles with tunable size and surface plasmon resonance frequency. Chemistry of materials 23(18):4098-4101.

Liu X, Dai Q, Austin L, Coutts J, Knowles G, Zou J, Chen H, Huo Q. 2008. A one-step homogeneous immunoassay for cancer biomarker detection using gold nanoparticle probes coupled with dynamic light scattering. J Am Chem Soc 130(9):2780-2782.

Llorens A, Lloret E, Picouet PA, Trbojevich R, Fernandez A. 2012. Metallic-based micro and nanocomposites in food contact materials and active food packaging. Trends in Food Science & Technology 24(1):19-29.

Lombardi JR, Birke RL, Lu T, Xu J. 1986. Charge‐transfer theory of surface enhanced Raman spectroscopy: Herzberg–Teller contributions. The Journal of chemical physics 84(8):4174-4180.

López FJG, Quereda C. 2011. Melamine toxicity: one more culprit in calcium kidney lithiasis. Kidney international 80(7):694-696.

Luo X, Morrin A, Killard AJ, Smyth MR. 2006. Application of nanoparticles in electrochemical sensors and biosensors. Electroanalysis 18(4):319-326.

Lyvers DP, Moon J-M, Kildishev AV, Shalaev VM, Wei A. 2008. Gold nanorod arrays as plasmonic cavity resonators. ACS Nano 2(12):2569-2576.

Magnuson BA, Jonaitis TS, Card JW. 2011. A Brief Review of the Occurrence, Use, and Safety of Food‐Related Nanomaterials. J Food Sci 76(6):R126-R133.

Martirosyan A, Schneider Y-J. 2014. Engineered Nanomaterials in Food: Implications for Food Safety and Consumer Health. Int J Env Res Public Health 11(6):5720-5750.

Ming T, Feng W, Tang Q, Wang F, Sun L, Wang J, Yan C. 2009. Growth of tetrahexahedral gold nanocrystals with high-index facets. J Am Chem Soc 131(45):16350-16351.

Mura S, Seddaiu G, Bacchini F, Roggero PP, Greppi GF. 2013. Advances of nanotechnology in agro-environmental studies. Italian Journal of Agronomy 8(3):e18.

Murdock RC, Braydich-Stolle L, Schrand AM, Schlager JJ, Hussain SM. 2008. Characterization of nanomaterial dispersion in solution prior to in vitro exposure using dynamic light scattering technique. Toxicological Sciences 101(2):239-253.

Murphy CJ, Sau TK, Gole AM, Orendorff CJ, Gao J, Gou L, Hunyadi SE, Li T. 2005. Anisotropic metal nanoparticles: synthesis, assembly, and optical applications. J Phys Chem B 109(29):13857-13870.

Murphy CJ, Thompson LB, Chernak DJ, Yang JA, Sivapalan ST, Boulos SP, Huang J, Alkilany AM, Sisco PN. 2011. Gold nanorod crystal growth: from seed-mediated synthesis to nanoscale sculpting. Current Opinion in Colloid & Interface Science 16(2):128-134.

Nepal D, Onses MS, Park K, Jespersen M, Thode CJ, Nealey PF, Vaia RA. 2012. Control over Position, Orientation, and Spacing of Arrays of Gold Nanorods Using Chemically Nanopatterned Surfaces and Tailored Particle–Particle–Surface Interactions. ACS Nano 6(6):5693-5701.

Nie Z, Petukhova A, Kumacheva E. 2009. Properties and emerging applications of self-assembled structures made from inorganic nanoparticles. Nat Nanotech 5(1):15-25.

Nikoobakht B, El-Sayed MA. 2003. Preparation and growth mechanism of gold nanorods (NRs) using seed-mediated growth method. Chem Mater 15(10):1957-1962.

Orendorff CJ, Murphy CJ. 2006. Quantitation of metal content in the silver-assisted growth of gold nanorods. J Phys Chem B 110(9):3990-3994.

Pal S, Tak YK, Song JM. 2007. Does the antibacterial activity of silver nanoparticles depend on the shape of the nanoparticle? A study of the gram-negative bacterium Escherichia coli. Appl Environ Microbiol 73(6):1712-1720.

Panáček A, Kvitek L, Prucek R, Kolar M, Vecerova R, Pizurova N, Sharma VK, Nevečná Tj, Zboril R. 2006. Silver colloid nanoparticles: synthesis, characterization, and their antibacterial activity. J Phys Chem B 110(33):16248-16253.

Pecora R. 1985. Dynamic light scattering: applications of photon correlation spectroscopy. Springer.

Pei SC, Zhang YY, Eremin SA, Lee WJ. 2009. Detection of aflatoxin M1 in milk products from China by ELISA using monoclonal antibodies. Food Control 20(12):1080-1085.

Peng B, Li G, Li D, Dodson S, Zhang Q, Zhang J, Lee YH, Demir HV, Yi Ling X, Xiong Q. 2013. Vertically Aligned Gold Nanorod Monolayer on Arbitrary Substrates: Self-Assembly and Femtomolar Detection of Food Contaminants. ACS Nano 7(7):5993-6000.

Petukhova A, Greener J, Liu K, Nykypanchuk D, Nicolaÿ R, Matyjaszewski K, Kumacheva E. 2012. Standing Arrays of Gold Nanorods End‐Tethered with Polymer Ligands. Small 8(5):731-737.

Pillai ZS, Kamat PV. 2004. What factors control the size and shape of silver nanoparticles in the citrate ion reduction method? J Phys Chem B 108(3):945-951.

Prandini A, Tansini G, Sigolo S, Filippi L, Laporta M, Piva G. 2009. On the occurrence of aflatoxin M1 in milk and dairy products. Food Chem Toxicol 47(5):984-991.

Prasad B, Sorensen C, Klabunde KJ. 2008. Gold nanoparticle superlattices. Chem Soc Rev 37(9):1871-1883.

Prodan E, Radloff C, Halas N, Nordlander P. 2003. A hybridization model for the plasmon response of complex nanostructures. Science 302(5644):419-422.

Qian X, Peng XH, Ansari DO, Yin-Goen Q, Chen GZ, Shin DM, Yang L, Young AN, Wang MD, Nie S. 2008. In vivo tumor targeting and spectroscopic detection with surface-enhanced Raman nanoparticle tags. Nat Biotechnol 26(1):83-90.

Radoi A, Targa M, Prieto-Simon B, Marty JL. 2008. Enzyme-linked immunosorbent assay (ELISA) based on superparamagnetic nanoparticles for aflatoxin M1 detection. Talanta 77(1):138-143.

Rao CNR, Müller A, Cheetham AK. 2006. The chemistry of nanomaterials: synthesis, properties and applications. John Wiley & Sons.

Ray PC, Khan SA, Singh AK, Senapati D, Fan Z. 2012. Nanomaterials for targeted detection and photothermal killing of bacteria. Chem Soc Rev 41(8):3193-3209.

Reddy K, Salleh B, Saad B, Abbas H, Abel C, Shier W. 2010. An overview of mycotoxin contamination in foods and its implications for human health. Toxin Rev 29(1):3-26.

Reidy B, Haase A, Luch A, Dawson KA, Lynch I. 2013. Mechanisms of silver nanoparticle release, transformation and toxicity: a critical review of current knowledge and recommendations for future studies and applications. Materials 6(6):2295-2350.

Ren W, Zhu C, Wang E. 2012. Enhanced sensitivity of a direct SERS technique for Hg2+ detection based on the investigation of the interaction between silver nanoparticles and mercury ions. Nanoscale 4(19):5902-5909.

Rodriguez Velasco ML, Calonge Delso MM, Ordonez Escudero D. 2003. ELISA and HPLC determination of the occurrence of aflatoxin M(1) in raw cow's milk. Food Addit Contam 20(3):276-280.

Rycenga M, Cobley CM, Zeng J, Li W, Moran CH, Zhang Q, Qin D, Xia Y. 2011. Controlling the synthesis and assembly of silver nanostructures for plasmonic applications. Chemical reviews 111(6):3669-3712.

Santini A, Ferracane R, Meca G, Ritieni A. 2010. Comparison and improvement of the existing methods for the determination of aflatoxins in human serum by LC-MS/MS. Anal Methods 2(7):884.

Shang L, Wang Y, Jiang J, Dong S. 2007. pH-dependent protein conformational changes in albumin: gold nanoparticle bioconjugates: a spectroscopic study. Langmuir 23(5):2714-2721.

Singh AK, Senapati D, Wang S, Griffin J, Neely A, Candice P, Naylor KM, Varisli B, Kalluri JR, Ray PC. 2009. Gold nanorod based selective identification of

Escherichia coli bacteria using two-photon Rayleigh scattering spectroscopy. ACS Nano 3(7):1906-1912.

Siontorou CG, Nikolelis DP, Miernik A, Krull UJ. 1998. Rapid methods for detection of Aflatoxin M1 based on electrochemical transduction by self-assembled metal-supported bilayer lipid membranes (s-BLMs) and on interferences with transduction of DNA hybridization. Electrochim Acta 43(23):3611-3617.

Sivapalan ST, DeVetter BM, Yang TK, van Dijk T, Schulmerich MV, Carney PS, Bhargava R, Murphy CJ. 2013. Off-resonance surface-enhanced Raman spectroscopy from gold nanorod suspensions as a function of aspect ratio: not what we thought. ACS Nano 7(3):2099-2105.

Smith E, Dent G. 2005. Modern Raman spectroscopy: a practical approach. John Wiley & Sons.

Sokolov K, Follen M, Aaron J, Pavlova I, Malpica A, Lotan R, Richards-Kortum R. 2003. Real-time vital optical imaging of precancer using anti-epidermal growth factor receptor antibodies conjugated to gold nanoparticles. Cancer Res 63(9):1999-2004.

Sondi I, Salopek-Sondi B. 2004. Silver nanoparticles as antimicrobial agent: a case study on *E. coli* as a model for Gram-negative bacteria. J Colloid Interface Sci 275(1):177-182.

Stoloff L, Trucksess M, Hardin N, Francis OJ, Hayes J, Polan C, Campbell T. 1975. Stability of aflatoxin M in milk. J Dairy Sci 58(12):1789-1793.

Strange RN, Scott PR. 2005. Plant disease: a threat to global food security. Annu Rev Phytopathol 43:83-116.

Su Q, Ma X, Dong J, Jiang C, Qian W. 2011. A reproducible SERS substrate based on electrostatically assisted APTES-functionalized surface-assembly of gold nanostars. ACS Applied Materials & Interfaces 3(6):1873-1879.

Sun Y, Xia Y. 2003. Gold and silver nanoparticles: a class of chromophores with colors tunable in the range from 400 to 750 nm. Analyst 128(6):686-691.

Thai T, Zheng Y, Ng SH, Mudie S, Altissimo M, Bach U. 2012. Self‐Assembly of Vertically Aligned Gold Nanorod Arrays on Patterned Substrates. Angew Chem Int Ed 51(35):8732-8735.

Theiss J, Pavaskar P, Echternach PM, Muller RE, Cronin SB. 2010. Plasmonic nanoparticle arrays with nanometer separation for high-performance SERS substrates. Nano Lett 10(8):2749-2754.

Tiede K, Boxall ABA, Tear SP, Lewis J, David H, Hassellöv M. 2008. Detection and characterization of engineered nanoparticles in food and the environment. Food Addit Contam 25(7):795-821.

Tiede K, Boxall ABA, Wang X, Gore D, Tiede D, Baxter M, David H, Tear SP, Lewis J. 2010. Application of hydrodynamic chromatography-ICP-MS to investigate the fate of silver nanoparticles in activated sludge. Journal of Analytical Atomic Spectrometry 25(7):1149-1154.

Tighe M, Lockwood P, Wilson S, Lisle L. 2004. Comparison of digestion methods for ICP-OES analysis of a wide range of analytes in heavy metal contaminated soil samples with specific reference to arsenic and antimony. Commun Soil Sci Plant Anal 35(9-10):1369-1385.

Tombelli S, Mascini M, Scherm B, Battacone G, Migheli Q. 2009. DNA biosensors for the detection of aflatoxin producing Aspergillus flavus and A. parasiticus. Monatsh Chem 140(8):901-907.

Tong L, Wei Q, Wei A, Cheng JX. 2009. Gold nanorods as contrast agents for biological imaging: optical properties, surface conjugation and photothermal effects†. Photochem Photobiol 85(1):21-32.

Tong L, Zhu T, Liu Z. 2011. Approaching the electromagnetic mechanism of surface-enhanced Raman scattering: from self-assembled arrays to individual gold nanoparticles. Chem Soc Rev 40(3):1296-1304.

Tran B. 2014. Trace Analysis of Mycotoxins in Food Matrices by Solid Phase Extraction-Liquid Chromatography Tandem Mass Spectrometry. 2014 Annual Meeting. Iafp.

Tserkezis C, Papanikolaou N, Almpanis E, Stefanou N. 2009. Tailoring plasmons with metallic nanorod arrays. Phys Rev B 80(12):125124.

Turnipseed S, Casey C, Nochetto C, Heller DN. 2008. Determination of melamine and cyanuric acid residues in infant formula using LC-MS/MS. US FDA laboratory information bulletin 24.

Valenzuela A, Lorenzini R, Redondo M, Font G. 1999. Matrix solid-phase dispersion microextraction and determination by high-performance liquid chromatography with UV detection of pesticide residues in citrus fruit. J Chromatogr A 839(1):101-107.

Vigderman L, Khanal BP, Zubarev ER. 2012. Functional Gold Nanorods: Synthesis, Self‐Assembly, and Sensing Applications. Adv Mater 24(36):4811-4841.

von Maltzahn G, Park J-H, Agrawal A, Bandaru NK, Das SK, Sailor MJ, Bhatia SN. 2009. Computationally guided photothermal tumor therapy using long-circulating gold nanorod antennas. Cancer Res 69(9):3892-3900.

Wall P. 2014. One Health and the food chain: maintaining safety in a globalised industry. Vet Rec 174(8):189-192.

Wang C, Irudayaraj J. 2008. Gold nanorod probes for the detection of multiple pathogens. Small 4(12):2204-2208.

Wang C, Irudayaraj J. 2010. Multifunctional magnetic–optical nanoparticle probes for simultaneous detection, separation, and thermal ablation of multiple pathogens. Small 6(2):283-289.

Wang D, Möhwald H. 2004. Template-directed colloidal self-assembly–the route to 'top-down'nanochemical engineering. J Mater Chem 14(4):459-468.

Wang H, Huff TB, Zweifel DA, He W, Low PS, Wei A, Cheng J-X. 2005. In vitro and in vivo two-photon luminescence imaging of single gold nanorods. Proceedings of the National Academy of Sciences of the United States of America 102(44):15752-15756.

Wang HH, Liu CY, Wu SB, Liu NW, Peng CY, Chan TH, Hsu CF, Wang JK, Wang YL. 2006. Highly Raman‐Enhancing Substrates Based on Silver Nanoparticle Arrays with Tunable Sub‐10 nm Gaps. Adv Mater 18(4):491-495.

Wang J-J, Liu B-H, Hsu Y-T, Yu F-Y. 2011. Sensitive competitive direct enzyme-linked immunosorbent assay and gold nanoparticle immunochromatographic strip for detecting aflatoxin M1 in milk. Food Control 22(6):964-969.

Wang L, Zhu Y, Xu L, Chen W, Kuang H, Liu L, Agarwal A, Xu C, Kotov NA. 2010. Side‐by‐Side and End‐to‐End Gold Nanorod Assemblies for Environmental Toxin Sensing. Angew Chem Int Ed 49(32):5472-5475.

Watabe Y, Kondo T, Imai H, Morita M, Tanaka N, Hosoya K. 2004. Reducing bisphenol A contamination from analytical procedures to determine ultralow levels in environmental samples using automated HPLC microanalysis. Anal Chem 76(1):105-109.

Wei W, Ge G. 2013a. Monolayer of Nanorod Vertical Arrays Self-Assembled at the Air/Water Interface. Part Part Syst Charact 30(10):837-841.

Wei W, Ge G. 2013b. Monolayer of Nanorod Vertical Arrays Self‐Assembled at the Air/Water Interface. PART PART SYST CHAR (30):837-841.

Wood GE, Trucksess MW. 1998. Regulatory control programs for mycotoxin-contaminated food. Mycotoxins in Agriculture and Food Safety:459-481.

Wu HL, Tsai HR, Hung YT, Lao KU, Liao CW, Chung PJ, Huang JS, Chen IC, Huang MH. 2011. A comparative study of gold nanocubes, octahedra, and rhombic dodecahedra as highly sensitive SERS substrates. Inorganic chemistry 50(17):8106-8111.

Xie H, Gill-Sharp KL, O'Neal DP. 2007. Quantitative estimation of gold nanoshell concentrations in whole blood using dynamic light scattering. Nanomedicine: Nanotechnology, Biology and Medicine 3(1):89-94.

Xie Y, Guo S, Guo C, He M, Chen D, Ji Y, Chen Z, Wu X, Liu Q, Xie S. 2013. Controllable Two-Stage Droplet Evaporation Method and Its Nanoparticles Self-Assembly Mechanism. Langmuir 29(21):6232-6241.

Xie Y, Guo S, Ji Y, Guo C, Liu X, Chen Z, Wu X, Liu Q. 2011. Self-assembly of gold nanorods into symmetric superlattices directed by OH-terminated hexa (ethylene glycol) alkanethiol. Langmuir 27(18):11394-11400.

Xiulan S, Xiaolian Z, Jian T, Xiaohong G, Jun Z, Chu FS. 2006. Development of an immunochromatographic assay for detection of aflatoxin B1 in foods. Food Control 17(4):256-262.

Zhang J, Li Y, Zhang X, Yang B. 2010. Colloidal Self‐Assembly Meets Nanofabrication: From Two‐Dimensional Colloidal Crystals to Nanostructure Arrays. Adv Mater 22(38):4249-4269.

Zhang Q, Carmody L. 2009. Food Safety In China-A Briefing for Responsible Investors. Responsible Research.

Zhang X, Zhao J, Whitney AV, Elam JW, Van Duyne RP. 2006. Ultrastable substrates for surface-enhanced Raman spectroscopy: Al2O3 overlayers fabricated by atomic layer deposition yield improved anthrax biomarker detection. J Am Chem Soc 128(31):10304-10309.

Zhang Z, Lin M. 2014. High-yield preparation of vertically aligned gold nanorod arrays via a controlled evaporation-induced self-assembly method. J Mater Chem C 2(23):4545-4551.

Zhao T, Fan J-B, Cui J, Liu J-H, Xu X-B, Zhu M-Q. 2011. Microwave-controlled ultrafast synthesis of uniform silver nanocubes and nanowires. Chem Phys Lett 501(4-6):414-418.

Zheng J, He L. 2014. Surface-Enhanced Raman Spectroscopy for the Chemical Analysis of Food. Compr Rev Food Sci 13(3):317-328.

Zheng MZ, Richard JL, Binder J. 2006. A review of rapid methods for the analysis of mycotoxins. Mycopathologia 161(5):261-273.

VITA

Zhong Zhang was born in Ganzhou, Jiangxi, China on September 15, 1986. He obtained his Bachelor of Engineering degree in Food Engineering from Jiangnan University, Wuxi, China, in 2008. He received his Master of Food Engineering degree in the same program at Jiangnan University in 2010. He worked for Nestlé Nutrition Suzhou Manufacturing Plant for three months in 2011. In the fall of 2011, he joined University of Missouri to pursue his Ph.D. degree in Food Science. He received his doctoral degree in 2014.